

UCLA

UCLA Electronic Theses and Dissertations

Title

ImmunoPET imaging of murine CD4+ T cells using an anti-mouse CD4 antibody fragment

Permalink

<https://escholarship.org/uc/item/3426s469>

Author

Freise, Amanda Christine

Publication Date

2016

Peer reviewed|Thesis/dissertation

UNIVERSITY OF CALIFORNIA

Los Angeles

ImmunoPET imaging of murine CD4+ T cells
using an anti-mouse CD4 antibody fragment

A dissertation submitted in partial satisfaction
of the requirements for the degree Doctor of Philosophy
in Molecular and Medical Pharmacology

by

Amanda Christine Freise

2016

© Copyright by

Amanda Christine Freise

2016

ABSTRACT OF THE DISSERTATION

ImmunoPET imaging of murine CD4⁺ T cells
using an anti-mouse CD4 antibody fragment

by

Amanda Christine Freise

Doctor of Philosophy in Molecular and Medical Pharmacology

University of California, Los Angeles, 2016

Professor Anna Wu Work, Chair

CD4⁺ T cells orchestrate the immune system and play a key role in the response to infection, the induction and maintenance of some autoimmune diseases, and immunotherapy of cancer. Comprehensive, noninvasive imaging of CD4⁺ T cells would be an improvement upon current methods of analysis such as blood draws and biopsies. Molecular imaging of CD4⁺ T cells can be accomplished with immuno-positron emission tomography (PET), which utilizes antibody-based probes to detect and quantify cell surface markers. This dissertation describes the characterization of the functional properties of GK1.5 cys-diabody (cDb), an anti-mouse CD4 antibody fragment, and its use in detecting CD4⁺ T cells with immunoPET in a mouse model of inflammatory bowel disease.

Ideally, imaging probes should have minimal biological effect on the target of interest, and be suitable for imaging at low doses. In this work, the effect of GK1.5 cDb on murine CD4⁺ T cell function and CD4 expression was explored at multiple doses. Furthermore, the effect of protein dose on image contrast was assessed by performing a dose-escalation immunoPET study and *ex vivo* biodistribution analysis. The lowest protein dose of 2 µg ⁸⁹Zr-labeled GK1.5 cDb resulted in improved contrast of lymphoid organs in PET scans compared to higher doses. Intravenous administration of GK1.5 cDb caused a dose-dependent, transient decrease in CD4 expression in blood and lymphoid organs, which recovered within 3 days post-injection. Proliferation was inhibited *in vivo* in inguinal lymph nodes but not the spleen by injection of 40 µg GK1.5 cDb. Overall, using low dose GK1.5 cDb minimized biological effects on CD4⁺ T cells.

A potential application of anti-CD4 immunoPET is investigation of the localization of CD4⁺ T cells at sites of inflammation, and use imaging to guide treatment decisions. Here, immunoPET imaging with ⁸⁹Zr-malDFO-GK1.5 cDb was used to image the distribution of CD4⁺ T cells in the intestinal region of mice treated with dextran sulfate sodium to induce colitis. Increased uptake of GK1.5 cDb in the distal colon and mesenteric lymph nodes (MLN) of colitic mice was apparent from *in vivo* scans. *Ex vivo* scans and biodistribution analysis confirmed higher uptake in DSS-treated colons, ceca, and MLN. Anti-CD4 immunoPET was also used to image colitic mice after immunosuppressive treatment with cyclosporin A (CsA), although no significant changes were seen in the biodistribution of the probe between treated and non-treated mice.

This work shows that low dose GK1.5 cDb yields high-contrast immunoPET images with minimal effects on T cell biology, and was a useful tool for investigating CD4⁺ T cells in the context of preclinical inflammatory bowel disease.

The dissertation of Amanda Christine Freise is approved.

Jonathan Braun

Arion-Xenofon Hadjioannou

Samson A. Chow

Manuel L. Penichet

Ting-Ting Wu

Anna Wu Work, Committee Chair

University of California, Los Angeles

2016

Dedicated to my father Larry and my mother Diana

For your eternal and unwavering support

Table of Contents

1	Introduction	1
1.1	Molecular imaging	1
1.1.1	PET imaging	3
1.2	Antibody-based imaging.....	8
1.2.1	Antibody structure and function	8
1.2.2	ImmunoPET.....	10
1.2.3	ImmunoPET with intact antibodies	13
1.2.4	ImmunoPET with engineered antibody fragments	15
1.2.5	Labeling strategies	19
1.2.6	Applications of immunoPET.....	23
1.3	CD4+ T cells	27
1.3.1	Approaches to imaging immune cells	30
1.3.2	Antibody imaging of immune cells	32
1.4	Inflammatory bowel disease.....	35
1.4.1	Inflammatory bowel disease in humans.....	35
1.4.2	Clinical imaging of IBD.....	37
1.4.3	Dextran sulfate sodium mouse model of inflammatory bowel disease	38
2	GK1.5 cys-diabody.....	41

2.1	History and applications of intact GK1.5 antibody	41
2.2	Expression and production of GK1.5 cDb	43
2.3	Purification of GK1.5 cDb.....	44
2.4	Conjugation and labeling of GK1.5 cDb	45
3	ImmunoPET imaging of murine CD4 ⁺ T cells using anti-CD4 cys-diabody: Effects of protein dose on T cell function and imaging	47
3.1	Introduction	47
3.2	Materials and Methods.....	50
3.2.1	Animals.....	50
3.2.2	Conjugation and labeling of GK1.5 cDb.....	51
3.2.3	Production of soluble murine CD4	51
3.2.4	Soluble antigen binding assays	52
3.2.5	ImmunoPET imaging and biodistribution	53
3.2.6	Flow cytometry	53
3.2.7	Proliferation assays	54
3.2.8	Cytokine assays	55
3.2.9	Statistical analysis	56
3.3	Results	57
3.3.1	GK1.5 cDb retains specificity and affinity for murine CD4	57

3.3.2	ImmunoPET with low-dose ⁸⁹ Zr-malDFO-GK1.5 cDb yields high-contrast images of lymphoid organs	59
3.3.3	GK1.5 cDb causes transient decrease in CD4 expression in vivo	63
3.3.4	GK1.5 cDb alters CD4 ⁺ T cell proliferation and cytokine release in a dose-dependent manner in vitro	66
3.3.5	GK1.5 cDb decreases CD4 expression and inhibits CD4 ⁺ T cell proliferation in a dose-dependent manner in vivo	68
3.4	Discussion.....	70
3.5	Conclusions.....	74
4	ImmunoPET imaging of CD4 ⁺ T cells in mesenteric lymph nodes and colons of colitic mice.....	75
4.1	Introduction	75
4.2	Materials and Methods.....	77
4.2.1	Animals.....	77
4.2.2	Induction and assessment of colitis	77
4.2.3	Histopathological evaluation of inflammation and CD4 ⁺ T cell infiltration..	79
4.2.4	Flow cytometry	80
4.2.5	PET/CT Imaging.....	80
4.2.6	Image reconstruction and analysis	81
4.2.7	Statistical analysis	82

4.3	Results	83
4.3.1	DSS-induced colitis results in gross anatomical changes.....	83
4.3.2	Changes in CD4+ T cells in DSS-treated mice.....	86
4.3.3	ImmunoPET imaging of CD4 in colitic mice.....	88
4.4	Discussion.....	95
5	ImmunoPET imaging of CD4+ T cells in colitic mice after cyclosporin A immunosuppressive treatment	100
5.1	Introduction	100
5.2	Materials and Methods.....	103
5.2.1	Preparation of CsA	103
5.2.2	CsA treatment.....	103
5.3	Results	104
5.3.1	CsA treatment ameliorates some signs of colitis	104
5.3.2	CsA treatment alters percentage of CD4+ T cells in the spleen	106
5.3.3	Anti-CD4 immunoPET imaging of CsA-treated mice	106
5.4	Discussion.....	110
6	Conclusions	114

List of Figures

Figure 1.1 PET imaging.....	4
Figure 1.2 Positron-emitting radionuclides	5
Figure 1.3 [¹⁸ F]FDG imaging of highly glycolytic tissues	6
Figure 1.4 Immunoglobulin G structure	9
Figure 1.5 Desired characteristics of imaging vs. therapeutic antibodies.....	13
Figure 1.6 Antibody fragments	17
Figure 1.7 Applications of antibody imaging in oncology.....	25
Figure 1.8 Monitoring changes in biomarker expression in response to treatment	26
Figure 1.9 CD4+ T cell subsets	28
Figure 1.10 Imaging immune cells	34
Figure 2.1 SDS-PAGE gel of fractions	44
Figure 3.1 Schematic of antibody and cys-diabody structure.....	57
Figure 3.2 Affinity of GK1.5 cDb.....	58
Figure 3.3 Conformation of GK1.5 cDb	58
Figure 3.4 Effect of GK1.5 cDb protein dose on anti-CD4 immunoPET imaging.....	60
Figure 3.5 <i>Ex vivo</i> biodistribution from ⁸⁹ Zr-malDFO-GK1.5 cDb dose escalation	61
Figure 3.6 Target:muscle ratios from ⁸⁹ Zr-malDFO-GK1.5 cDb dose escalation study .	63
Figure 3.7 <i>In vivo</i> changes in CD4 expression, measured by RM4-4.....	64
Figure 3.8 <i>In vivo</i> effects of GK1.5 cDb on CD3+ T cells	65
Figure 3.9 <i>In vivo</i> changes in CD4 expression, measured by GK1.5.	66
Figure 3.10 <i>In vitro</i> effects of GK1.5 cDb on T cell proliferation.	67
Figure 3.11 <i>In vitro</i> effects of GK1.5 cDb on T cell IFN γ production.....	68

Figure 3.12 <i>In vivo</i> effects of GK1.5 cDb on CD4 expression	69
Figure 3.13 <i>In vivo</i> effects of GK1.5 cDb on CD4+ T cell proliferation	69
Figure 3.14 GK1.5 cDb administration affects proliferation <i>in vivo</i>	70
Figure 4.1 DSS treatment plan.....	78
Figure 4.2 DSS-induced weight loss	83
Figure 4.3 Disease activity index scores of colitic mice.....	84
Figure 4.4 DSS induces gross anatomical changes in the colon.....	84
Figure 4.5 DSS increases average MLN weight.....	85
Figure 4.6 DSS-induced changes in MLN size and cellularity	85
Figure 4.7 DSS-induced histopathological damage	86
Figure 4.8 Anti-CD4 IHC staining of colon tissue	87
Figure 4.9 Flow cytometric analysis of CD4+ T cells in spleen and MLN	88
Figure 4.10 Anti-CD4 immunoPET of colitic mice	90
Figure 4.11 <i>Ex vivo</i> scans of colons, ceca, and MLN	91
Figure 4.12 <i>Ex vivo</i> biodistribution analysis.....	92
Figure 5.1 DSS and CsA treatment plan	103
Figure 5.2 Effects of CsA on body weight and disease activity index.....	104
Figure 5.3 Effects of CsA on colon gross anatomy	105
Figure 5.4 Effects of CsA on average MLN size.....	105
Figure 5.5 Flow cytometric analysis of CD4+ T cells in spleen and MLN	106
Figure 5.6 Anti-CD4 immunoPET of CsA-treated colitic mice	108
Figure 5.7 <i>Ex vivo</i> scans of colons, ceca, and MLN.....	109
Figure 5.8 <i>Ex vivo</i> biodistribution analysis.....	110

Acknowledgements

This work would not have been possible without the incredible members of the Wu Lab: Anna Wu, Richard Tavaré, Kirstin Zettlitz, Felix Bergara, and Wen-Ting Tsai. To my mentor, Dr. Anna Wu, thank you for taking me into your lab, allowing me the opportunity to study immunology, and for always pushing me to improve. I am so grateful I had the chance to work in your lab and push immunoPET forward. I am very appreciative of Drs. Richard Tavaré and Kirstin Zettlitz, both of whom have been excellent scientific mentors and who were never too busy to answer any question or to discuss any result. It was from both of you that I learned how solid science is done. Special thanks to Richard, as his proof-of-concept GK1.5 cDb enabled me to pick up the project quickly (and graduate on time!). Kirstin, you are my Sam Bee – I wish I had more female role models like you who are powerful, inspiring, and independent. Felix, you put me at ease in the lab from day one and provided many laughs every day afterward, not to mention an immense amount of research support – thank you. Wen-Ting, I may have been ahead of you by a couple years but the truth is that I often looked to you for inspiration and motivation as a scientist and as a graduate student. I am so glad our friendship went beyond the doors of CNSI and into the great wide world, where we have had such awesome adventures. It has truly been a delight to work in a lab with terrific people who were not just co-workers, but “frolleagues” and I will always remember fondly the myriad misadventures we had in and out of the lab.

To each of my wonderful committee members – Drs. Sam Chow, Ting-Ting Wu, Arion Chatzioannou, Jonathan Braun, and Manuel Penichet - thank you so much for your

insight and guidance during my PhD. I knew I was lucky when I looked forward to our meetings! I owe extra gratitude to Sam, Ting-Ting, and Arion, who gave me career guidance and supported my extra-PhD endeavors. Enormous thanks go to Emily Fitch, for being a terrific, knowledgeable student affairs officer and a wonderful friend. It's been a pleasure to do my PhD in the department of Molecular and Medical Pharmacology, where I've always felt that new ideas were welcome and encouraged – thank you to Mike Phelps and the many faculty who stimulated discussion and interest. I am also proud and grateful to have worked with so many other wonderful graduate students in the realm of science communication.

Much of my research was supported by core facilities on UCLA campus, by too many excellent staff to name individually. Thank you to everyone at the Tissue Procurement Core Laboratory, the Factor Flow Core, the Crump Preclinical Imaging Core, the David Geffen School of Medicine Statistics Core, and the Immune Assessment Core. A special thank you to Dr. Waldemar Ladno at the Crump, from whom I learned so much about imaging, mice, and extraordinary patience. Thank you to Kha Huynh and Alec Estrada for their wonderful technical support in lab, and for being the best undergraduate lab members we could ask for! And thanks are due to Scott Knowles, Keyu Li, and other past members of the Anna Wu Lab, whose dissertations served as excellent examples.

Finally, the biggest thanks of all goes to my wonderful immediate and extended family. Mom, Dad, Alyssa, Laurie, and Erin – I would have gone crazy a million times over if I didn't have you. I hope I've made you as proud as I am of all of you. I love you. To every scientist and engineer in my family, and everyone who loved and supported them, thank you for encouraging me to explore and succeed academically. Dad, you used to

have a sweatshirt with a quote: “The truly educated never graduate.” I may have graduated, but thanks to you I will never stop wanting to learn.

I am grateful for the funding that supported me during my studies, including the UCLA Eugene Cota-Robles Fellowship, the UCLA Dissertation Year Fellowship, and grants from the National Institutes of Health.

Portions of Chapter 1 and Chapter 6 appeared as a review article in *Molecular Immunology*: Freise AC, Wu AM (2015) *In vivo* imaging with antibodies and engineered fragments. *Mol Immunol* 67:142–52. doi: 10.1016/j.molimm.2015.04.001.

Chapter 3 is a reproduction of an article published in *Molecular Imaging and Biology*: Freise, A.C., Zettlitz, K.A., Salazar, F.B., Lu, X., Tavaré, R., Wu, A.M. In press. ImmunoPET imaging of murine CD4+ T cells using anti-CD4 cys-diabody: Effects of protein dose on T cell function and imaging. *Mol Imaging Biol*. Dr. Richard Tavaré, Dr. Kirstin Zettlitz, and Mr. Felix Bergara contributed to the experimental design, data collection, and analysis in this work, and Dr. Xiang Lu contributed to the statistical analysis.

Chapter 4 is in the process of being submitted for publication.

Vita

Education

Expected Ph.D., Molecular and Medical Pharmacology, UCLA
Dec 2016
2011 B.S., Genetics, UCI

Honors and Awards

2015 Best Talk in Session: Pharmacology Departmental Retreat, UCLA
2014 Best Talk: Pharmacology Departmental Talks, UCLA
2014 Best Student Poster: Pharmacology Departmental Retreat, UCLA
2013 Certificate of Distinction in Teaching in the Life Sciences, UCLA
2011 Excellence in Undergraduate Research, UCI
2011 Honors in Biological Sciences, UCI
2009 Honorary Summer Undergraduate Research Program Fellowship, UCI

Research Support

2016 UCLA Dissertation Year Fellowship
2012 Eureka Scholarship
2011 Eugene Cota-Robles Fellow
2010 Summer Undergraduate Research Program Stipend
2010 Undergraduate Research Opportunities Program Grant
2009 Friends of the CNLM Summer Undergraduate Award

Professional Certifications

2016 Entering Mentoring Training, by: National Institutes of Health
2016 Certified Interpretive Guide, by: National Association for Interpretation

Leadership Experience

2016 Editor-in-Chief and Founder, *Signal to Noise Magazine*
2015-16 President and Founder, SciComm Hub @ UCLA
2016 Mentor, HHMI Pathways Peer Mentoring Program, UCLA
2009-10 Resident Advisor, Undergraduate Research Interest Hall, UCI

Peer-Reviewed Publications

Freise AC, Tavaré R, Zettlitz K, Salazar FB, Wu AM. In press. ImmunoPET imaging of murine CD4⁺ T cells using anti-CD4 GK1.5 cys-diabody: Effects of protein dose on T cell function and imaging. *Mol Imag Bio*.

Freise AC, Wu AM. 2015. *In vivo* imaging with antibodies and engineered fragments. *Mol Immun* 67(2 Pt A): 142-52.

McGowan LD, Alaama RA, Freise AC, Huang JC, Charvet CJ, Striedter GF. 2012. Expansion, folding, and abnormal lamination of the chick optic tectum after intraventricular injections of FGF2. *Proc Nat Acad Sci* 109: doi:10.1073/pnas.1201875109.

Non-Peer Reviewed Publications

Freise AC. 2016. It's time for scientists to stop explaining so much. *Scientific American Guest Blog* URL: <http://blogs.scientificamerican.com/guest-blog/it-s-time-for-scientists-to-stop-explaining-so-much/>

Freise AC. 2014. Epidemiology and Laboratory Techniques. In: Pfluegl G, editor. *Life Sciences LS23L: Introduction to Laboratory & Scientific Methodology, third edition*. Plymouth (MI): Hayden McNeil.

Presentations

Freise AC, Tavaré R, Salazar FB, Zettlitz K, Braun J, Wu AM. ImmunoPET imaging CD4+ T cells in a mouse model of colitis using an ⁸⁹Zr-labeled anti-CD4 cys-diabody [abstract]. In: World Molecular Imaging Congress, September 7-10, 2016 in New York, NY, USA.

Freise AC, Tavaré R, Zettlitz K, Salazar FB, Wu AM. Immuno-PET of murine T helper lymphocytes with an anti-CD4 cys-diabody [abstract]. In: Midwinter Conference of Immunologists, January 23-26, 2016 in Asilomar, CA, USA.

Tavaré R, Freise AC, Salazar FB, Wu AM. ImmunoPET imaging of murine T helper lymphocytes with an anti-CD4 cys-diabody [abstract]. In: World Molecular Imaging Congress, September 2-8, 2015 in Honolulu, HI, USA.

Tavaré R, Freise AC, Salazar FB, Olafsen T, Wu AM. 2014. ImmunoPET imaging of CD4 expression using an anti-CD4 cys-diabody. Presented at Imaging in 2020, September 22, 2014 in Jackson Hole, Wyoming, USA.

Freise AC, Huang JC, Charvet CJ, Striedter GF. Effects of exogenous fibroblast growth factor-2 on brain development in birds [abstract]. In: Neuroscience, November 13-17, 2010, San Diego, CA, USA.

1 Introduction

1.1 Molecular imaging

Imaging modalities such as x-ray computed tomography (CT), magnetic resonance imaging (MRI), and ultrasound are current backbones in diagnostic medicine, but these methods are largely restricted to providing anatomical and physiological information. In parallel with the development of highly targeted therapeutics, there is an increasing need to analyze specific targets and biomarkers *in vivo*, including distinct molecules, events, and processes. Molecular imaging allows detection of these targets, usually via use of radioactive and/or optical probes, and offers numerous advantages, including the ability to detect biomarkers with nanomolar sensitivity, visualization and quantitation (for some modalities) of biomarkers throughout the entire organism, and the potential for serial imaging (James and Gambhir, 2012).

The questions that molecular imaging has the potential to answer are many and varied, due in part to the diversity of targets and the ability to design bespoke probes to interrogate them. Specific metabolic processes can be investigated using tracers that are analogues for key metabolites. Expression of specific biomarkers can be assessed, which has broad applications not only for oncology but also for other diseases and disorders. These types of data can be used to plan treatment and determine whether therapeutics are successful, sometimes before an anatomical change (e.g. tumor shrinkage) is apparent.

Choosing a target, and an appropriate probe for said target, is crucial for molecular imaging. Ideally a target should be expressed/active uniquely or at high levels on the cells of interest, and at low levels elsewhere. If the target is expressed at high levels in normal tissues, creating a target or antigen “sink,” higher amounts of probe may be needed to image outside these tissues. The target must be accessible; whether a target is extracellular or intracellular will determine which types of probes will be suitable. Knowledge of the internalization properties of the target is also important, as this influences the choice of both probe and label. Targets which are shed by cells at high rates can pose problems for imaging as the probe may end up at high concentrations in the circulation, making localization of the cells of interest difficult. Finally, the target must be informative: imaging must give a specific answer for the question at hand.

After a target of interest is identified, a corresponding probe and label must be chosen. Small molecules, peptides, proteins, cells, and antibodies, among others, can all be labeled and administered *in vivo*. Ideally a probe should be biologically inert, enabling imaging without causing functional changes in the system. Immunogenicity of the probe should be avoided as much as possible, not only to avoid the initiation of an immune response in the organism, but also to allow for serial imaging. Depending on the location of the target, various probes are better suited than others for imaging; for instance, for targets expressed in the brain, probes which can cross the blood-brain barrier are usually needed. Targets expressed in the liver, a major organ of clearance, may be simpler to image with a probe that clears directly through the kidney.

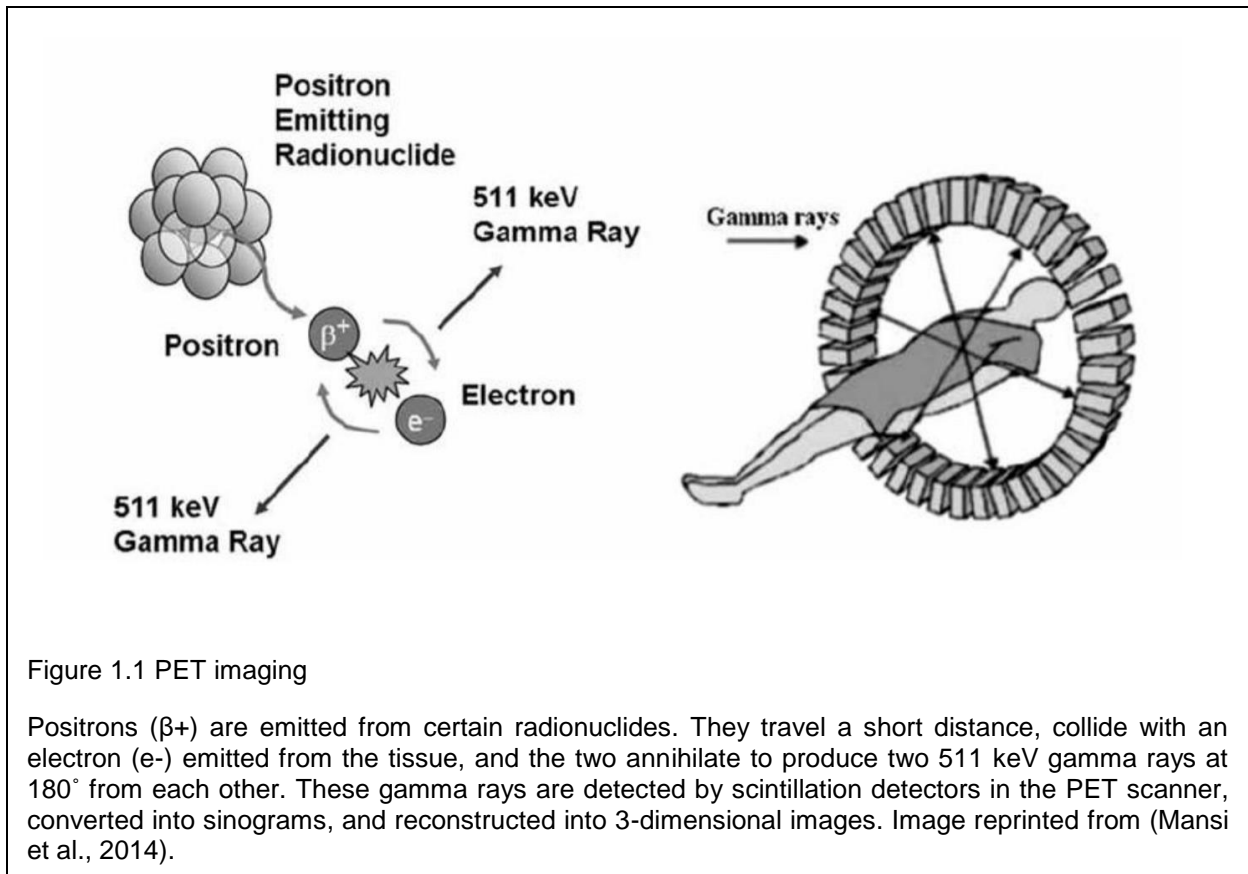
Molecular imaging offers numerous advantages compared to other methods of analysis. It can permit visualization and quantitation of targets throughout the entire body,

thereby providing information representative of the entire living organism. This is particularly critical when studying disease processes that are disseminated or systemic, such as cancer metastasis or immune responses. Imaging targets *in vivo* also means that the target is examined in its natural state, in contrast to traditional methods which require removing and processing of tissue. In animal studies, molecular imaging allows repeat assessment of the same subject over time, reducing variability. In the clinical setting, non-invasive imaging stands to have an increasing impact, circumventing the sampling limitations inherent to tissue biopsy.

There are multiple imaging modalities which can be utilized for molecular imaging, including nuclear, optical, magnetic resonance, and ultrasound. This dissertation will focus on nuclear imaging, specifically positron emission tomography, and the use of antibodies as probes.

1.1.1 PET imaging

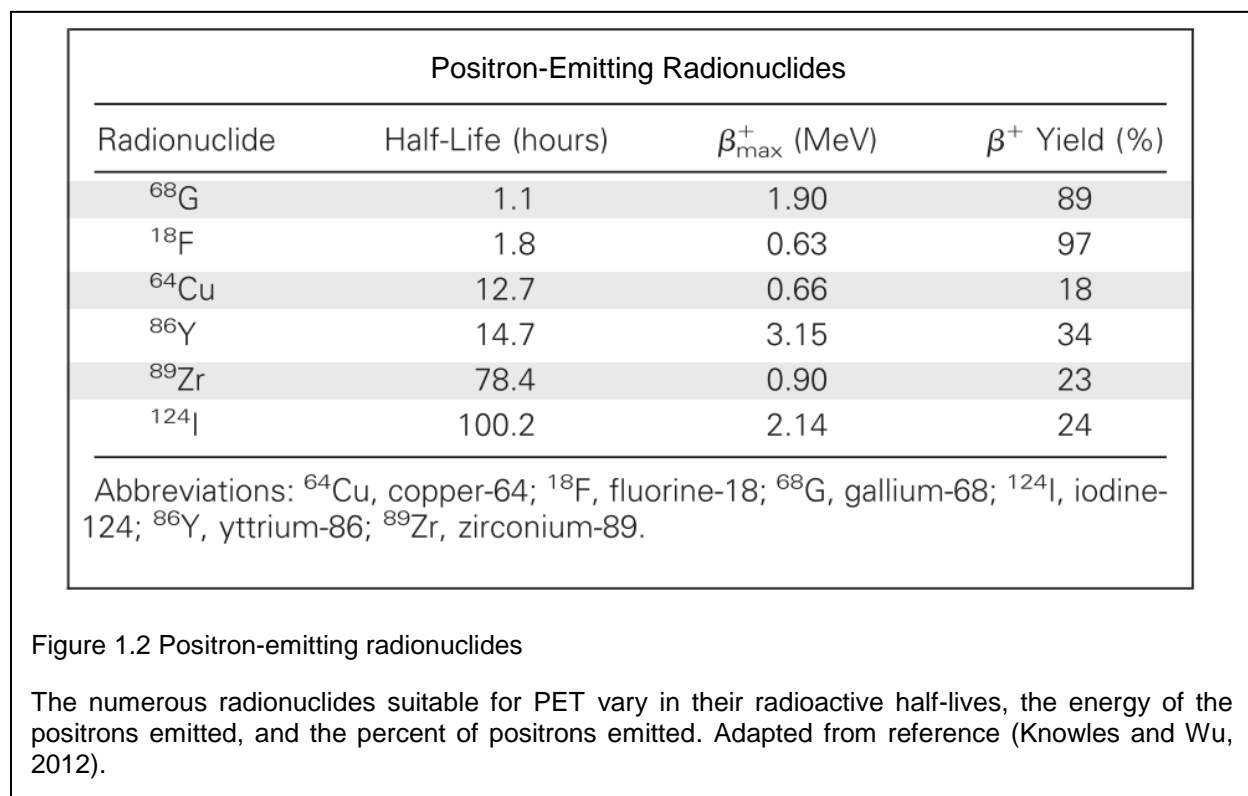
One of the most common modalities for molecular imaging is positron emission tomography (PET). PET enables noninvasive, sensitive detection and quantitation of biomarkers and biological processes. A positron-emitting radionuclide is used to label a probe which is typically injected intravenously into an organism (Figure 1.1). When a positron collides with a nearby electron, they annihilate and two 511 keV gamma rays are produced 180° apart. Pairs of gamma rays, when detected at approximately the same time by a ring of scintillation detectors surrounding the organism, are registered as coincidence events. Multiple coincidences are converted into sinograms, which are ultimately reconstructed into 3-dimensional images. The high energy of the gamma rays



enables limitless depth of tissue penetration (James and Gambhir, 2012). CT or MRI scans are often used to provide an anatomical reference for the signal seen on PET.

An increasing number of radionuclides are commercially available, the choice of which depends upon the biomarker to be detected, the probe to be used, and the physical characteristics of the radionuclide (Figure 1.2) (Knowles and Wu, 2012). For internalizing targets, a residualizing radiolabeling approach, where radioactive metabolites remain trapped inside the cell following internalization and metabolism, may be desirable to maximize activity accumulation in target cells; however, activity will also be retained in normal organs of clearance, increasing background. Radiolabeling can be carried out a specific sites on a molecule, or randomly using certain motifs (such as a particular amino acid on a protein-based probe). Site-specific conjugation typically results in more

predictable labeling and is advantageous because it is known where on the probe labeling will occur, thereby enabling avoidance of important regions of the tracer.



PET/CT can be used in oncology to detect cancer, typically with the use of [^{18}F]-2-fluoro-2-deoxyglucose ([^{18}F]FDG), a glucose analog for metabolic imaging (Figure 1.3) (James and Gambhir, 2012). To synthesize [^{18}F]FDG, the C-2 hydroxyl group on glucose is replaced with fluorine-18. [^{18}F]FDG can still be transported into the cell and phosphorylated by hexokinase (which is upregulated by highly glycolytic cancers), but the lack of the hydroxyl group prevents further metabolism, therefore trapping [^{18}F]FDG-6-phosphate inside the cell. PET imaging then detects regions of [^{18}F]FDG accumulation (Figure 1.3). [^{18}F]FDG has become ubiquitous and is the standard to which other probes

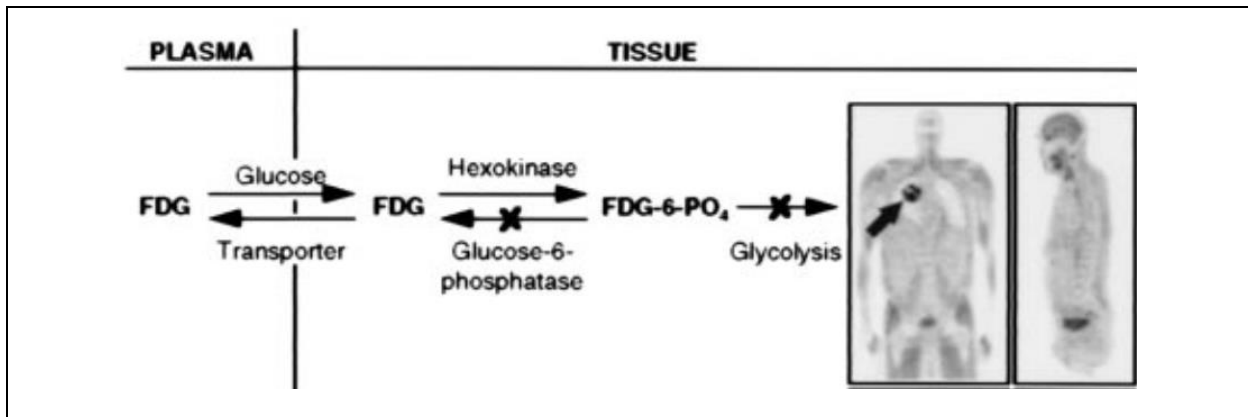


Figure 1.3 $[^{18}\text{F}]\text{FDG}$ imaging of highly glycolytic tissues

$[^{18}\text{F}]\text{FDG}$ is transported into the cell and converted by hexokinase into $[^{18}\text{F}]\text{FDG}$ -6-phosphate, and becomes trapped inside the cell. Highly glycolytic tissues often have upregulated hexokinase activity, which enables use of $[^{18}\text{F}]\text{FDG}$ to image metabolism. The arrow on the PET image points to a tumor, visualized by $[^{18}\text{F}]\text{FDG}$. Adapted from (Phelps, 2000).

must compare, but it is not without flaws; not all cancers are highly glycolytic, and false positives can occur in areas which have other types of rapidly proliferating cells, such as regions of inflammation and infection. Probes for other metabolic pathways include amino acids, choline, and nucleoside analogs (Phelps, 2000; Schuster et al., 2016; Zhu et al., 2011). Non-metabolic probes for cancer detection and monitoring may rely on surface biomarkers expressed by cancers. For example, breast cancer patients can be stratified into treatment groups depending on tumor surface expression of human epidermal growth factor receptor 2 (HER2); however, expression can vary within the primary tumor, and between the primary tumor and metastases (Ulaner et al., 2016). Imaging with ^{89}Zr -labeled trastuzumab, an antibody probe specific for HER2, enabled noninvasive screening of metastases of several breast cancer patients and the discovery of HER2-positive metastases resulted in updated treatment plans (Ulaner et al., 2016). Ligands for receptors expressed highly on or within cancer cells can also be radiolabeled and used as PET probes, such as the radiolabeled steroid ^{18}F -16 β -fluoro-5 α -dihydrotestosterone

(^{18}F FDHT). ^{18}F FDHT binds to the androgen receptor which is often upregulated by prostate cancer (Pandit-Taskar et al., 2016)

PET imaging also has numerous applications outside of oncology, and a wealth of probes have been clinically approved or are under investigation. The ability to noninvasively image is particularly useful for investigating the brain and nervous system. Since the brain relies heavily on glucose metabolism, ^{18}F FDG has been used to assess changes in brain activity associated with, but not limited to, aging (Greve et al., 2016), dementia (Brown et al., 2014; Silverman, 2004), and Alzheimer's disease (Johnson et al., 2012). ^{18}F FDG also detects neuroinflammation and was demonstrated to image inflammatory infiltrates in the spinal cords of mice with experimental autoimmune encephalomyelitis, a model of multiple sclerosis (Buck et al., 2012). Other probes can be used to image biomarkers of certain diseases; for example, probes for tau and β -amyloid can detect pathological protein depositions present in Alzheimer's disease and other dementia-associated disease (Catafau and Bullich, 2015; Schöll et al., 2016; Waldron et al., 2016). PET imaging also has utility for cardiovascular disease. Tracers such as ^{15}O H₂O, ^{13}N NH₃, and ^{82}Rb RbCl can be used to measure perfusion in the heart (Y. Li et al., 2014). Determination of myocardium health can be done with ^{18}F FDG; nonviable areas have a reduction in ^{18}F FDG uptake (Y. Li et al., 2014). Wound healing following myocardial infarction was assessed with a radiolabeled peptide containing an asparagine-glycine-arginine (NGR) motif which targets CD13, a surface marker expressed on fibroblasts and immune cells (Tillmanns et al., 2015). A major focus of this work is the use of PET imaging to detect inflammation and infection, which will be discussed in depth in Section 1.3.1.

1.2 Antibody-based imaging

Antibodies are proteins produced by the immune system which bind to previously encountered antigens and can signal to immune cells to interact with the target of the antibody, typically to induce destruction. The hallmark of an antibody protein is its ability to recognize a target antigen with exquisite specificity, which not only enables its immunological function but also makes them invaluable tools in biotechnology and medicine. Over the past decades, antibodies have evolved to become a mainstay of biotherapeutics, bolstered by progress in target discovery and validation, advances in antibody isolation, design, and engineering, and successes in clinical translation and commercialization (Scott et al., 2012). In parallel, the continued development of antibody-based therapeutics requires a detailed understanding of the normal function of potential targets, and how modifications contribute to, or are correlated with, disease. Antibodies have already provided invaluable tools for biomedical investigations. The precise discrimination offered by antibodies has formed the basis of workhorse assays used in research labs worldwide. Antibodies are essential components in ELISAs, flow cytometry, immunocyto- and immunohistochemistry (ICC and IHC), immunofluorescence, Western blotting, immunoprecipitation, protein microarray analysis, and many other techniques.

1.2.1 Antibody structure and function

Antibodies are immunoglobulin (Ig) proteins. Multiple classes of Ig exist including IgA, IgE, IgM, IgD, and IgG, each of which has different structures and properties. The focus of this dissertation will be IgG antibodies and fragments thereof. IgG antibodies are

Y-shaped homodimers of two heavy chains (50 kDa each) and two light chains (25 kDa each). The heavy chain is comprised of the variable heavy (V_H) domain and three constant domains (C_H1-3); the light chain is comprised of the variable light (V_L) domain and one constant domain (C_L) (Figure 1.4). The domains can be divided into two major regions: the fragment, antigen binding (Fab) region (including the V_H , V_L , and C_L , and C_H1 domains) and the fragment, crystallizable (Fc) region (comprised of C_H2 and C_H3 dimers). The V_H and V_L domains each contain three hypervariable loops, all six of which interact to form the complementarity-determining regions (CDRs), or antigen-binding sites, which recognize a unique antigen (Maynard and Georgiou, 2000). Intact antibodies are bivalent, meaning they have two sets of CDRs and can bind to two identical antigens at one time. The Fc region mediates a number of biological functions, including serum recycling,

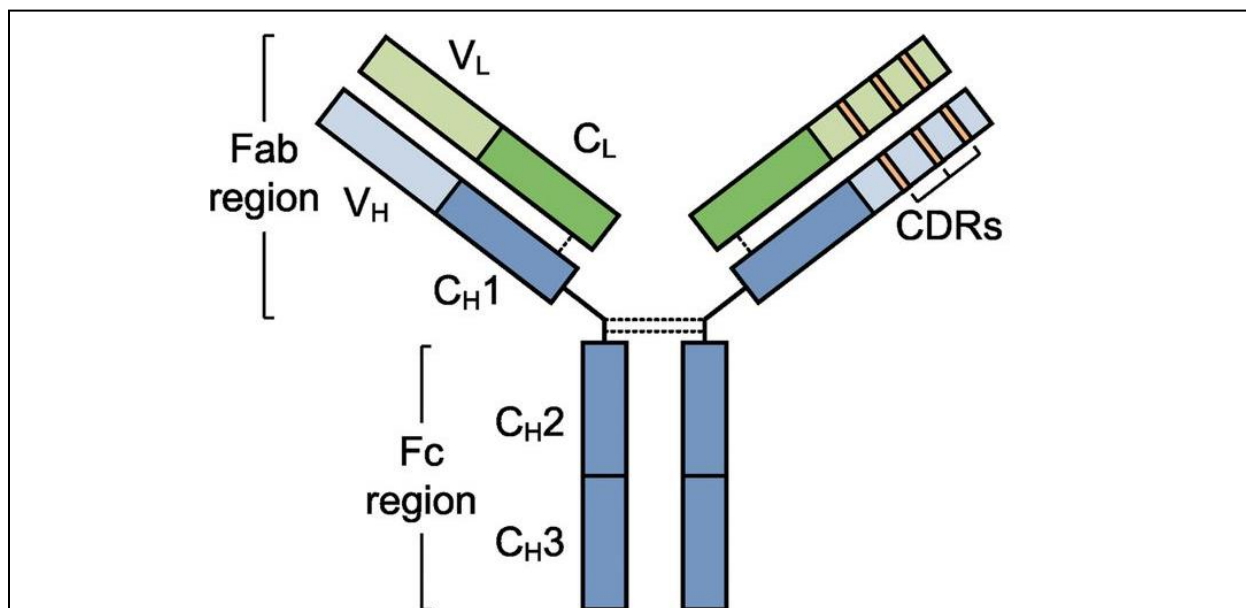


Figure 1.4 Immunoglobulin G structure

A schematic depicting the structure of a typical IgG molecule. IgGs are homodimers of two heavy (blue) and two light (green) chains. The heavy chains are held together by disulfide bonds (dashed lines), and each heavy and light chain are held together by a disulfide bond. Reprinted from (Ruigrok et al., 2011)

antibody-dependent cell-mediated cytotoxicity, and complement-dependent cytotoxicity (Redman et al., 2015).

IgG proteins are naturally maintained in plasma for long periods of time due to their ability to recycle through the neonatal Fc receptor (FcRn), a transport protein which facilitates transcytosis of IgG across the placenta to the fetus but is also expressed normally in the gut, liver, and on endothelial cells in adults. IgG are primarily active in tissues and participate in humoral immunity in several ways: complement-mediated cytotoxicity (CDC), antibody-mediated cell-dependent cytotoxicity, and neutralization (in which they bind viruses, toxins, etc. and prevent them from interacting with host cells) (Janeway Jr et al., 2001).

Antibodies can be cleaved enzymatically to produce Fab and Fc regions. Papain, a protease, cleaves on the Fab side of the disulfide bonds which link the two heavy chains together, producing two monovalent Fab fragments and one Fc fragment. Pepsin, another protease, cleaves on the Fc side of the disulfide bonds and produces one bivalent $F(ab')_2$ fragment and one Fc fragment (Janeway Jr et al., 2001). Cleaving antibodies is a straightforward way of developing a (limited) set of fragments which can be used as molecular imaging probes; one can easily alter the valency and molecular weight while removing the Fc region. However, engineering of antibodies at the genetic level allows for even more customization, which will be discussed in Section 1.2.4.

1.2.2 ImmunoPET

ImmunoPET combines the sensitivity of PET with the specificity and affinity of antibody-based probes to allow identification and quantitation of specific biomarkers

within the body. Antibodies have utility as imaging probes for several reasons. The ability of antibodies to engage specific targets with nanomolar or picomolar affinity provides a foundation for developing highly sensitive imaging agents. The relatively large size of antibodies means that a variety of cargoes, for imaging or therapeutic applications, can be appended without perturbing their innate specificity and targeting properties (in contrast to the challenges faced in modifying small molecules or peptides for imaging purposes). The resounding successes of antibody therapeutics validate their ability to find and engage their targets *in vivo*. Furthermore, corresponding expertise and infrastructure are now in place for the routine large-scale production and purification of antibodies for clinical use. Finally, advances in protein engineering allow customization of biophysical and biological properties of antibodies to enhance their efficacy.

Importantly, current interest in antibody imaging is driven by the need for specific molecular information to guide the development and use of targeted therapeutics. Non-invasive imaging using antibodies provides a powerful and general approach for assessing cell surface phenotype *in vivo*. Detection and quantification of tissue- or tumor-specific markers *in vivo* can be used to identify and localize tumors, providing information on the nature and extent of disease. There are also numerous ways in which molecular imaging can contribute to development and applications of targeted therapeutics. An obvious example would be the assessment of target expression and availability *in vivo*, which would not only be informative for patient selection, but could also provide an early indication of potential normal organ toxicities. Whole-body evaluation of target expression would be of value due to the heterogeneity observed in metastatic cancers, including intralesion and lesion-to-lesion variations. Imaging can be

employed for direct assessment of pharmacokinetics, biodistribution, and targeted delivery of therapeutic antibodies labeled with radionuclides or dyes. Molecular imaging can also provide highly specific readouts of response to therapy, either directly or indirectly. Direct elimination of targeted cells or downregulation of biomarkers can be assessed. Alternatively, antibody-based imaging of a cell surface biomarker can provide a downstream readout of intracellular events, providing insights into pathways and mechanism. In summary, the potential applications of imaging cell-surface phenotype, based on the specificity afforded by antibodies, are many.

Decades of research and development of antibodies for therapeutic applications has led to a wealth of information and experience in areas that are also highly relevant to the generation of imaging agents (Scott et al., 2012). For example, the potential immunogenicity of murine antibodies in patients has led to robust methods for routine humanization of antibodies or directly accessing fully human antibodies via technologies such as phage display. Availability of antibodies that cross-react with human and murine or primate target proteins can facilitate toxicological studies. The steady expansion of the use of antibody-drug conjugates and radioimmunoconjugates for therapy has increased attention to conjugation methods and spurred interest in site-specific conjugation (Agarwal and Bertozzi, 2015; Smaglo et al., 2014).

Manufacturability and stability must be addressed up front for clinical applications. Furthermore, imaging applications impose additional requirements on the agents employed (Figure 1.5). Optimal pharmacokinetics and distribution differ; whereas therapeutic antibodies need to achieve significant concentrations in target tissue over time (high area-under-the-curve), imaging agents instead need to achieve high contrast

Therapy		Imaging	
Lack of immunogenicity: use of humanized or human antibodies			
Site-specific conjugation			
Target requirements: high expression in disease state; low normal tissue background			
Target internalization: Yes for antibody-drug conjugates, etc. No for pretargeted/bispecific applications		Target internalization: Residualizing vs non-residualizing labeling approaches available for either case	
Innate biological activity -or- Conjugation/fusion to therapeutic moiety		Biologically inert	
Serum persistence - High area-under-the-curve		Accelerated clearance - High contrast	
Normal hepatobiliary clearance		Clearance directed via hepatobiliary or renal route	

Figure 1.5 Desired characteristics of imaging vs. therapeutic antibodies

Properties such as effector function, half-life, and conjugation sites are modified to suit either therapy or imaging applications.

at early times. As a result, the long plasma persistence of most intact antibodies can be disadvantageous for imaging purposes. However, this has not prevented their use as probes in animals or people. There are multiple approaches to modification of antibodies for *in vivo* imaging including protein engineering and modification, conjugation strategies, and the types of tracers and tags that can be introduced for detection by various imaging modalities.

1.2.3 ImmunoPET with intact antibodies

Intact antibodies function well as therapeutics due to their long serum half-life (1-3 weeks), increasing exposure of the affected tissues to the antibody; furthermore, biological activity from the Fc domain is often essential for therapeutic function (Wu, 2014). In contrast, the long half-life of intact antibodies hampers their use as imaging

agents: several days are required for blood and background clearance in order to achieve a good signal:noise ratio. For radiolabeled antibodies, this means that the organism will be exposed to radioactivity for an extended period of time. Furthermore, biological activity is undesirable in an imaging agent, in the interest of studying the system without perturbing it and reducing the risk of unwanted side effects.

Since 1990, only a few intact antibodies have been approved for use as clinical radioimaging agents. The first approved probes were for single photon emission computed tomography (SPECT) imaging, and include [^{111}In]satumomab pendetide (OncoScintTM) which targets Tag-72, a surface antigen commonly expressed on colorectal and ovarian cancers, [$^{99\text{m}}\text{Tc}$]arcitumomab (CEAScanTM) a Fab fragment which targets carcinoembryonic antigen, also expressed on colorectal cancers, and [^{111}In]capromab pendetide (ProstaScintTM) which binds PSMA, a target upregulated on prostate cancers. The success of these agents has been limited for several reasons, including immunogenicity resulting from use of murine antibodies and the disadvantages inherent to SPECT imaging such as challenges in quantitation and limited spatial resolution (James and Gambhir, 2012; Knowles and Wu, 2012). In the case of ProstaScint the epitope targeted was intracellular, meaning that only cells with damaged cell membranes could be imaged, limiting the sensitivity of the probe (Bouchelouche et al., 2010).

However, there are also advantages to using intact antibodies as imaging agents. Reformating antibodies into fragments sometimes results in an undesirable or unacceptable loss of affinity, so some antibodies are not suitable for reformating. In addition, imaging with a therapeutic antibody allows for treatment planning with the same

agent, a strategy applied to radioimmunotherapy with the anti-CD20 intact antibody Bexxar™ (tositumomab), a therapeutic antibody for non-Hodgkin's lymphoma refractory to rituximab treatment. To plan treatment, cold tositumomab is first injected to block the CD20 antigen sink in the spleen, followed by administration of ¹³¹I-tositumomab at a dosimetric radiation dose and gamma camera/SPECT imaging to determine patient-specific pharmacokinetics and the administered activity required to achieve the desired total-body dose (typically 75 cGy) (Dewaraja et al., 2014; Wahl, 2005). The second administration is then carried out using the calculated therapeutic dose.

Although intact antibodies have the potential to make their way back into the clinic with success, especially when linking imaging to treatment planning, many of the obstacles they present can be addressed by engineering them into fragments.

1.2.4 ImmunoPET with engineered antibody fragments

Intact antibodies can be cleaved or reformatted into smaller antibody fragments with a variety of molecular weights, valencies, clearance routes, and conjugation strategies (Figure 1.6). Retention of the Fv (fragment variable) domain preserves antigen binding, but fragments typically lack the Fc region, eliminating complement- and effector cell-mediated immune interactions. Removal of the Fc region also prevents recycling through the FcRn pathway, facilitating visualization of targeted tissues via rapid blood clearance and improved contrast. Smaller fragments also enable the use of radionuclides that decay more rapidly (e.g. ¹⁸F); the combination of short physical and biological half-lives of a radiotracer can result in reduced radiation exposure. Furthermore, use of lower-

molecular weight antibody fragments and proteins (below ~60 kDa) accelerates elimination via renal clearance. Several recent reviews have described in detail the biochemical and biophysical properties of antibody fragments (Freise and Wu, 2015; James and Gambhir, 2012; Wu, 2014).

Using single-chain variable fragments (scFv; 25 kDa) and portions of the constant region (C_H) as building blocks, additional fragments can be constructed such as diabodies (Db; dimers of scFv, 50 kDa), minibodies (Mb; dimers of scFv-C_H3, 80 kDa), and scFv-Fc (dimers of scFv fused to Fc, 105 kDa) (Figure 1.6) (James and Gambhir, 2012; Olafsen and Wu, 2010). Comparisons of the pharmacokinetics and targeting of intact and antibody fragments (enzymatically-derived and recombinant) have been conducted; recent examples include targeted imaging of prostate-specific membrane antigen (PSMA) using ¹¹¹In-radiolabeled F(ab')₂ and Fab (Fragment antigen binding) fragments, and ⁸⁹Zr-labeled minibodies and diabodies with SPECT or PET (Lütje et al., 2014; Pandit-Taskar et al., 2016; Viola-Villegas et al., 2014). Continued interest in smaller antibody fragments and protein scaffolds is evidenced by several imaging studies with nanobodies (Bannas et al., 2014; Keyaerts et al., 2016; Massa et al., 2014) and affibodies (Honarvar et al., 2017; Sørensen et al., 2016; Strand et al., 2014). Nanobodies (~15kDa) are single-domain variable heavy chain (V_{HH}) fragments, which are derived from heavy chain-only antibodies found in camelids (Schoonooghe et al., 2012), while affibodies (~7kDa) are based on *Staphylococcus aureus* protein A (Zielinski et al., 2012). The small sizes of these fragments enable them to bind to epitopes that antibody Fv-based fragments

cannot access (Schoonooghe et al., 2012) and makes them suitable for applications in which extremely rapid clearance is desired.

The route of clearance can be influenced by the size, charge, and hydrophobicity/hydrophilicity of the fragment as well as any fused or conjugated moieties. Fragments with molecular weights below the renal threshold (~60 kDa) clear through the kidneys; larger fragments are eliminated through the liver. Thus, format selection depends upon the final imaging application (e.g. use of a renally-cleared probe if liver metastases









	Format	Composition	Valency	Approx. MW (kDa)	Typical Serum $t_{1/2}$	Clearance Route
	Intact IgG	$(V_H + V_L)_2$	Bivalent	150-160	1-3 weeks	Hepatic
	F(ab') ₂	$(V_H C_{H1} + V_L + C_L)_2$	Bivalent	110	8-10 h	Hepatic
	Minibody	$(scFv + C_{H3})_2$	Bivalent	75	5-10 h	Hepatic
	Fab	$V_H C_{H1} + V_L + C_L$	Monovalent	50-55	12-20 h	Renal
	Diabody	$(scFv)_2$	Bivalent	50	3-5 h	Renal
	scFv	$V_H + V_L$	Monovalent	28	2-4 h	Renal
	Nanobody	$V_H H$ (Camelid)	Monovalent	12-15	30-60 m	Renal
	Affibody	Z domain of protein A (<i>S. aureus</i>)	Monovalent	7	30-60 m	Renal

Figure 1.6 Antibody fragments

Summary of salient properties of intact antibodies, enzymatic fragments, recombinant fragments and smaller scaffolds.

are to be visualized). A novel approach for controlling clearance and image contrast is offered by blocking the FcRn salvage receptor with Fc-engineered antibodies, or Abdegs (Ward et al., 2015). These IgG mutants have higher affinity for the FcRn recycling receptor than wildtype IgG, thus preventing other IgG – such as imaging probes - from binding FcRn. The net result is accelerated clearance and degradation of the imaging IgG. Swiercz et al. showed that an injection of Abdegs 8 hours after administration of ¹²⁴I-pertuzumab decreased background and improved tumor-to-blood ratios (Swiercz et al., 2014). The authors also note that the faster clearance time of the labeled probe decreased the levels of radioactivity exposure, an important consideration in clinical practice (Swiercz et al., 2014; Ward et al., 2015).

Antibodies can also be modified at specific amino acid residues to enable site-specific conjugation (Agarwal and Bertozzi, 2015). In contrast to conjugation at random surface residues, which produces a heterogeneous product and may introduce the label into the antigen-binding site (ABS), site-specific labeling creates a homogenous product in which the label can be intentionally located away from the ABS. A common approach is the addition of a cysteine residue at the carboxyl-terminus, which creates a site for specific labeling via a thio-ether bond (Massa et al., 2014; Olafsen et al., 2004; Tavaré et al., 2014a, 2014b). Alternatively, bio-orthogonally reactive unnatural amino acids, which are not naturally encoded in the genetic code but can still be incorporated artificially into proteins, can be inserted to provide specific sites for conjugation (Axup et al., 2012; Kim et al., 2013, 2012; Wu et al., 2016). Conserved glycosylation sites in antibodies can be utilized for site-specific conjugation as well (Rochefort et al., 2014)

1.2.5 Labeling strategies

Chemical conjugation is a critical step in attaching a detectable tracer to an antibody or fragment. Ideally, labeling should proceed quickly and with high efficiency, at established tracer:antibody ratios, and the immunoconjugate should be stable under *in vivo* conditions. Conjugation can be either direct (e.g., radionuclide or dye is attached directly to the antibody at certain amino acids) or indirect (e.g. radiometal labeling via attachment of a chelating moiety, such as 1,4,7,10-tetraazacyclododecane-N, N', N'', N'''-tetraacetic acid (DOTA) or desferrioxamine (DFO)). Both direct and indirect labeling may lead to incorporation of the tracer at random sites on the protein, potentially impacting immunoreactivity if the ABS is modified. This can be addressed by engineering a specific site for tracer conjugation away from the ABS, as discussed above. The choice of conjugation strategy – site-specific or random - can alter the biodistribution and pharmacokinetics of the labeled antibody. In an immunoPET study, Tavaré et al. demonstrated that labeling an anti-ALCAM cys-diabody site-specifically with ^{64}Cu using maleimide-DOTA resulted in increased tumor uptake and improved tumor-to-blood ratios compared to random labeling using N-hydroxysuccinimide-DOTA (Tavaré et al., 2014b).

The use of click chemistry potentially simplifies conjugation of tracer molecules to imaging antibodies. Click chemistry reactions are modular and rapid, give high product yields and nontoxic byproducts, remain stable in physiological conditions and utilize benign solvents (Kolb et al., 2001; Meyer et al., 2016). The rapid reaction rates of several click chemistries (Rossin and Robillard, 2014) are especially advantageous for radiolabeling with short-lived isotopes such as ^{18}F or ^{68}Ga , and can be used for

longer-lived radionuclides as well. In a recent study, site-specific labeling and click chemistry were combined to label the anti-CD20 antibody rituximab: an unnatural amino acid was site-specifically incorporated into two sites on rituximab, followed by click conjugation with DOTA under mild conditions, producing an antibody with precisely two chelates (Wu et al., 2016). Radiolabeling the immunoconjugate with ^{64}Cu enabled immunoPET of Ramos CD20+ tumor-bearing mice, although the use of an intact antibody required 60 h to elapse to achieve a high tumor:background ratio (Wu et al., 2016). *Trans*-cyclooctene (TCO) and tetrazine are often used together to accomplish click labeling. Rashidian et al. installed TCO-functionalized peptides onto anti-MHC II single domain antibodies, and then used click chemistry to label the probe with tetrazine-labeled [^{18}F]FDG (Rashidian et al., 2015). This approach capitalized on the widespread availability of [^{18}F]FDG in radiopharmacies, compared to other ^{18}F -labeled probes, which are not as ubiquitous.

Background signal can be reduced by pretargeting, in which the antibody is modified so that it can capture a ligand-bound radioisotope or tag, injected only after the antibody has had time to pre-localize to its target *in vivo* (Patra et al., 2016). This approach can dramatically improve contrast and also reduces non-specific toxicity, a consideration when radioactive detection is employed (Zeglis et al., 2013). Pretargeting can be accomplished by engineering a bispecific antibody, which recognizes both the target of interest and the radioligand (Marquez and Lapi, 2016); alternatively, pretargeting can utilize click chemistry. Zeglis et al. demonstrated pre-targeted *in vivo* labeling using A33 antibody modified with TCO to enable an inverse-electron demand Diels-Adler reaction. Twelve hours after injection into mice with EGFR-expressing

tumors, ^{64}Cu -NOTA-tetrazine was administered for PET imaging and biodistribution studies. In comparison to A33 directly labeled with ^{64}Cu or ^{89}Zr , comparable uptakes and target:background ratios were obtained, but at much shorter times and reduced dose deposition (Zeglis et al., 2013). Evans et al. extended the concept by demonstrating pretargeted click labeling of cetuximab-TCO followed by ^{68}Ga -DOTA-tetrazine administration. Pretargeting for 23 hours increased the tumor:liver ratio to 2.64, compared with a ratio of < 0.5 for free ^{68}Ga -DOTA-tetrazine or 3 hour pretargeting (Evans et al., 2014). More recently, in a study of immunoPET for pancreatic cancer, anti-CA19.9 intact antibody 5B1 was modified with TCO and injected into mice with pancreatic tumor xenografts; tetrazine-NOTA- ^{64}Cu radioligand was injected after 72 hr to click onto the antibody-TCO conjugate, and immunoPET was performed 20 h later (Houghton et al., 2016).

Many factors must be considered in the selection of the most appropriate radiolabel, as can be seen from studies that compare different radionuclides attached to the same probe. For instance, a recent study compared the use of ^{124}I and ^{89}Zr as labels for the A11 anti-PSCA (prostate stem cell antigen) minibody in a murine prostate cancer xenograft model. Although ^{89}Zr -A11 demonstrated significantly higher PSCA-positive tumor uptake, activity also accumulated non-specifically in other organs, leading to increased background and lower contrast. ^{124}I -A11 activity cleared quickly from nontumor tissue and, despite its comparatively lower accumulation in the tumor, had significantly higher tumor:blood contrast. Therefore, although PSCA internalizes slowly, ^{124}I was determined to be the better choice of radionuclide for imaging in this model (Knowles et al., 2014).

Ideally one wants to match the physical half-life of the radionuclide with the biological half-life of the antibody or fragment. Fluorine-18 is of great interest for same-day imaging due to its high positron yield and favorable short half-life (109.8 min), which matches the fast clearance of smaller fragments such as scFvs, nanobodies and affibodies, but rapid labeling methods are essential. Methods using vinyl sulfone linker chemistry (Wu et al., 2014) or aluminum fluoride (Lütje et al., 2014; McBride et al., 2012) have decreased the time required for labeling from several hours to as little as 30 minutes, making ^{18}F a viable option. For larger fragments such as intact antibodies and minibodies, ^{124}I ($t_{1/2} = 4.18$ d) is better suited; however, conventional iodination yields a non-residualizing label and therefore is more appropriate for non-internalizing targets. ^{64}Cu ($t_{1/2} = 12.7$ hr) and ^{89}Zr ($t_{1/2} = 78.4$ hr) are well-matched for intermediate-sized fragments such as scFvs, diabodies, and minibodies, as well as intact antibodies. Use of ^{89}Zr has dramatically expanded recently due to its half-life and ease of production; in addition, its positron emissions are lower energy than those of ^{124}I , improving intrinsic resolution (van de Watering et al., 2014). ^{89}Zr is usually attached indirectly to an antibody via chelation with DFO. However, ^{89}Zr released from DFO accumulates in bone and can presents toxicity issues or obscure imaging of lesions in the bone. Efforts have been made to improve upon the chelating molecule (Deri et al., 2014; Guérard et al., 2014, 2013; Price et al., 2014). Scandium-44 ($t_{1/2} = 3.9$ h) continues to be explored in conjunction with intermediate-sized fragments such as Fabs (Chakravarty et al., 2014) and even affibodies (Honarvar et al., 2017), and gallium-68 ($t_{1/2} = 68$ min) is gaining popularity as a label for smaller fragments such as nanobodies and affibodies (Honarvar et al., 2014; Keyaerts et al., 2016; Xavier et al., 2013). $^{99\text{m}}\text{Tc}$ ($t_{1/2} = 6.0$ hr) continues to be the most commonly

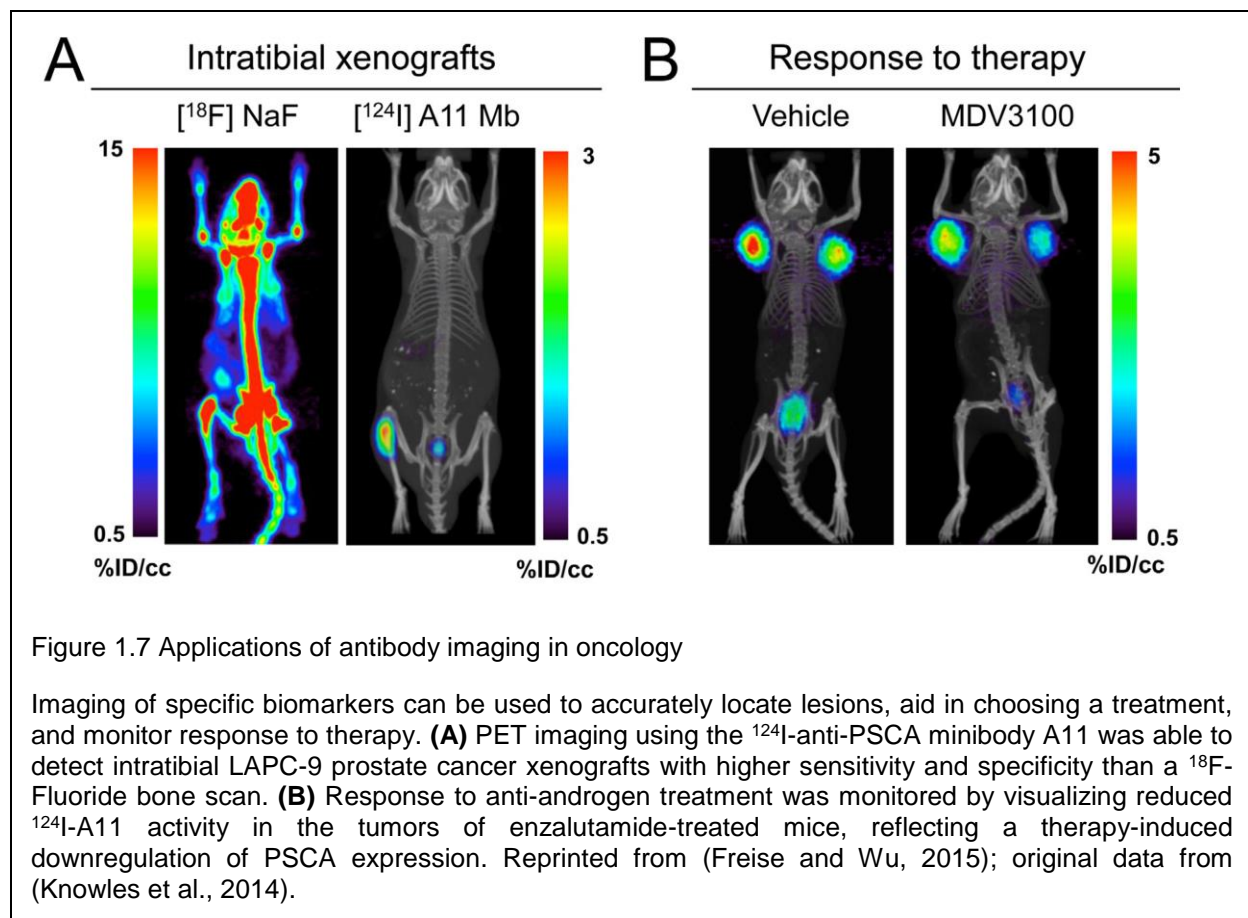
used SPECT radionuclide for a variety of uses in the clinic including conventional bone scans. Its broad availability has enabled numerous groups to label antibodies with ^{99m}Tc for the detection of varied biomarkers; recent examples include anti-VCAM-1 for inflamed atherosclerotic lesions in mice (Broisat et al., 2014), anti-EGFR for imaging small tumors (Krüwel et al., 2016), anti-RAGE F(ab')₂ for atherosclerotic plaques in pigs (Johnson et al., 2014), anti-CD11b for myeloid-derived suppressor cells in colon cancer (Cheng et al., 2015) or for imaging inflamed atherosclerotic plaques (Liu et al., 2016) and anti-gelsolin nanobodies for imaging amyloid deposits in familial amyloidosis (Verhelle et al., 2016)

1.2.6 Applications of immunoPET

The precision with which antibodies can identify their targets has stimulated broad development of applications, particularly in oncology. Current mainstream diagnostic imaging approaches, while practical and effective, still leave room for improvement. For example, PET using [^{18}F]FDG has proved invaluable for the detection of elevated glycolysis which is a hallmark of malignant transformation, but suffers from false negatives (from tumors with more indolent growth, or reliance on other metabolic pathways) or false positives (e.g. from infection or inflammation). ^{99m}Tc -MDP bone scintigraphy is a workhorse method for detecting metastases based on bone remodeling. However, it is non-specific: other biological processes (fractures, arthritis, inflammation) also generate positive signals, and soft tissue lesions are not addressable. Knowles et al. recently compared PET imaging using ^{18}F -NaF bone scans to a tumor-specific ^{124}I -PSCA minibody for detecting intratibial prostate cancer in a mouse model (Knowles et al., 2014),

illustrating the significant advantages of targeting a tumor-specific marker in this setting (Figure 1.7).

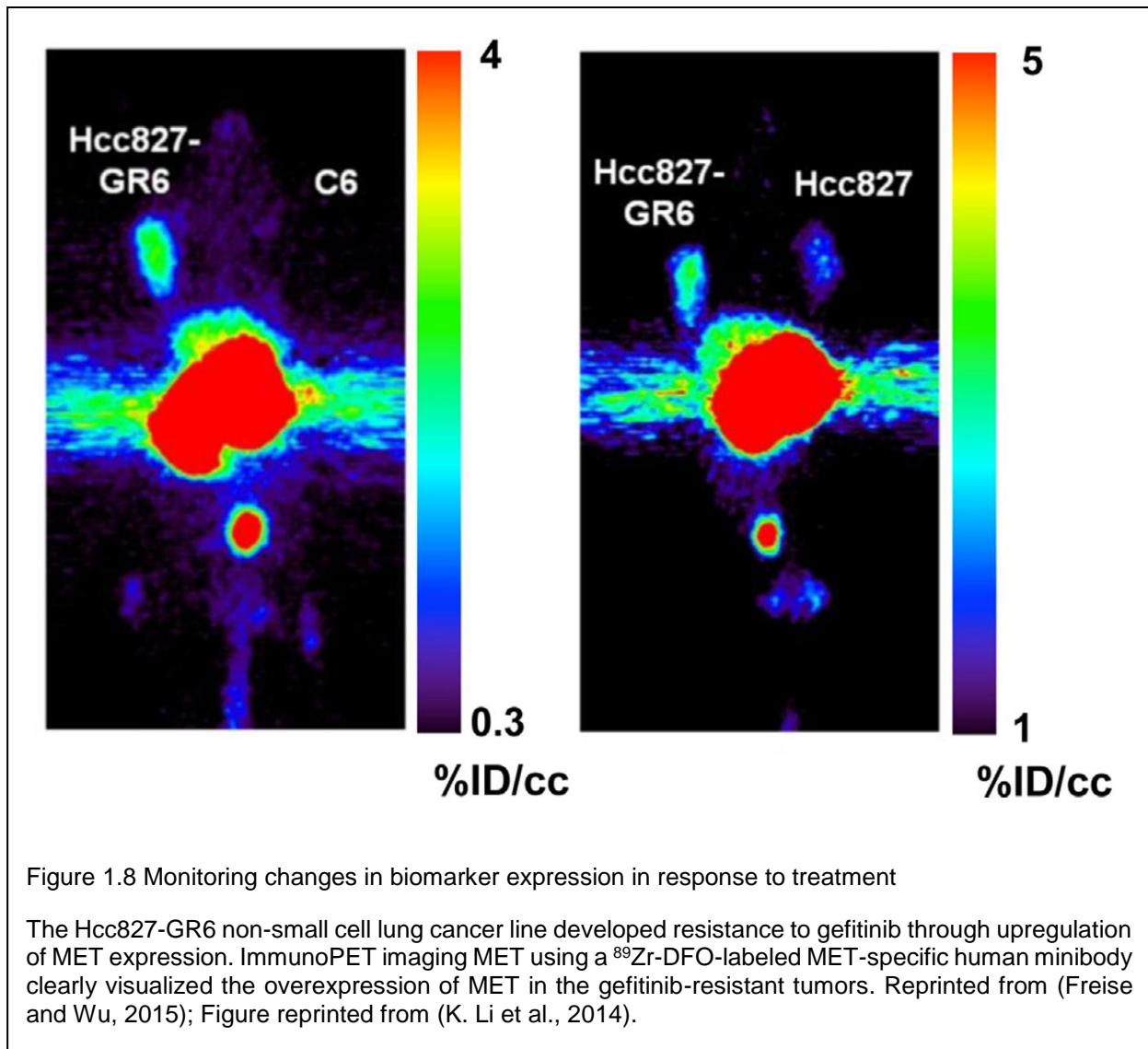
Beyond biomarker-specific visualization of disease there is great interest in developing antibodies as theranostic agents which act as both diagnostic and therapeutic molecules (Fleuren et al., 2014). Theranostic uses of antibodies may be particularly pertinent in oncology, where distinct alterations can be exploited for molecularly-targeted therapy. *In vivo* imaging using antibodies provides a versatile approach for identification and characterization of tumors for diagnosis, staging and disease management. Non-invasive detection and quantitation of biomarkers is increasingly needed for profiling disease in specific patients, and may be essential for addressing heterogeneity *in vivo*. Furthermore, therapeutic antibodies themselves can be directly labeled in order to assess drug delivery and target saturation. In preclinical models, including breast cancer models expressing different levels of HER2 (Zielinski et al., 2012) and lung, pancreatic, and prostate cancer xenograft models expressing differential Axl levels (Liu et al., 2014; Nimmagadda et al., 2014), antibody-directed PET has demonstrated that graded expression can be visualized. Antibody-based imaging provides a direct method for imaging response to therapy, and imaging cell-surface markers can provide insight into biological mechanisms of response. Recent examples include imaging EGFR downregulation to provide a measure of trastuzumab efficacy in HER2/EGFR-expressing tumors (Ma et al., 2014). A similar strategy was used to detect response to the mTOR inhibitor rapalog in renal cancer xenografts by imaging expression of VEGF, a downstream marker of mTOR activation (Chang et al., 2013). Knowles et al. employed the ¹²⁴I-PSCA-specific minibody to evaluate response to enzalutamide treatment in a



prostate cancer model, demonstrating downregulation of the androgen signaling axis *in vivo* (Figure 1.7). Ogasawara et al. demonstrated that antibodies specific for phosphatidylserine, which is transiently expressed on the cell surface during apoptosis, can be used to assess cell death in response to treatment; the long serum half-life of intact anti-phosphatidylserine antibodies proved advantageous for detection of the wave of apoptosis that occurred after delivery of pro-apoptotic therapy (Ogasawara et al., 2013). Antibody-directed imaging might also provide a method for assessing the development of resistance to therapy. Li et al. recently used engineered minibodies and diabodies derived from a phage display anti-MET antibody to image elevated MET in

non-small cell lung cancer xenografts from cell lines resistant to EGFR-targeted therapy via overexpression of MET (Figure 1.8) (K. Li et al., 2014).

Quantitative imaging has always played a central role in radioimmunotherapy, for assessing whether effective doses can be delivered to target tissues, while minimizing toxicity in normal tissues. PET imaging using ^{124}I -radretumab was used to estimate the dose delivered to the blood, bone marrow, and tumor in patients with brain metastases in advance of using ^{131}I -radretumab for radioimmunotherapy (Poli et al., 2013). Antibody



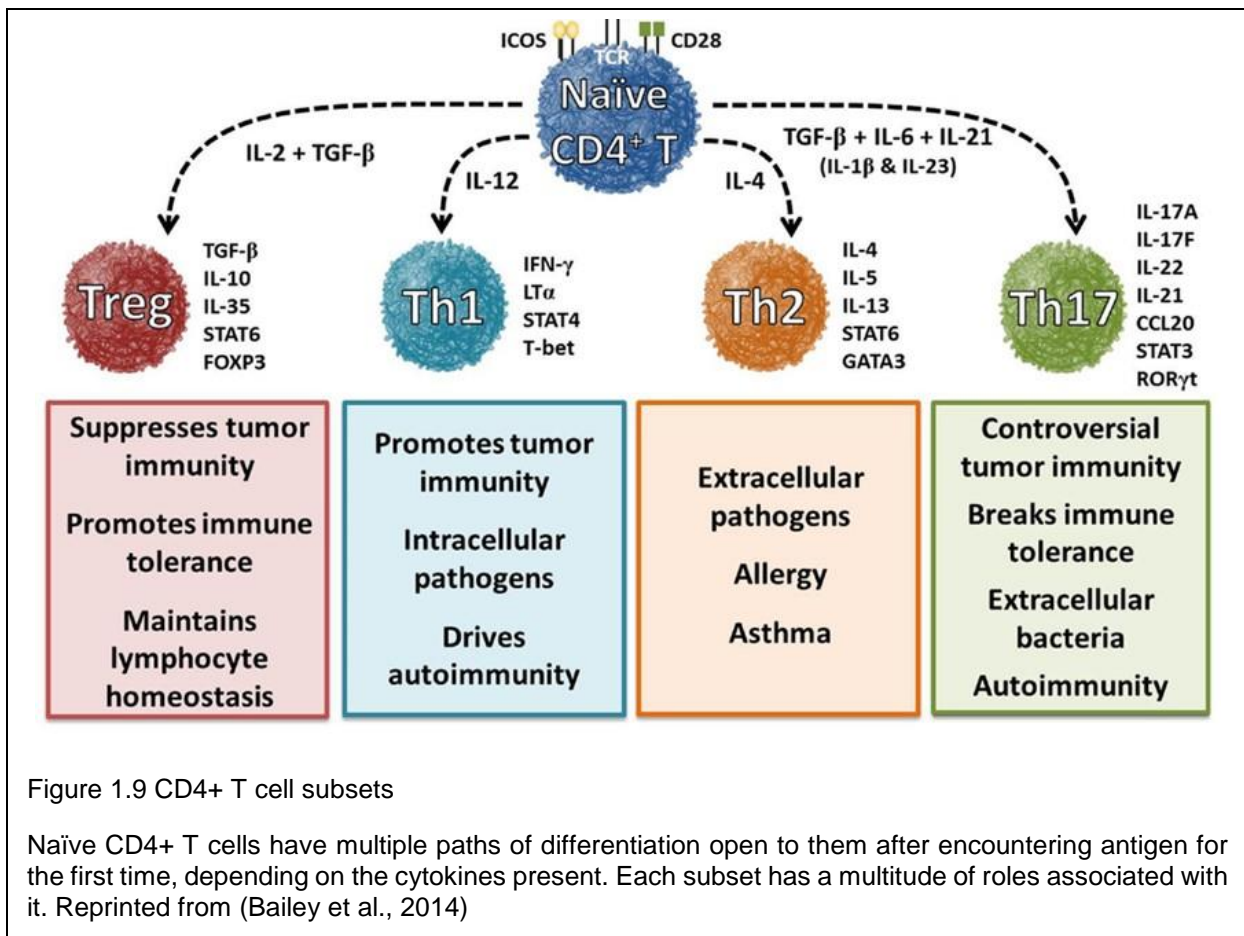
uptake varied even between lesions from the same patient. A recent pretargeting implementation utilized an antibody bispecific for TROP-2 (expressed at low levels in some glandular cells, and upregulated in several epithelial cancers) and the peptide hapten histamine-succinyl-glycine (HSG) to target prostate cancer xenografts in mice. Preliminary biodistribution studies using radiolabeled ^{111}In -di-HSG were conducted in order to establish optimal dose and timing. ImmunoPET with ^{68}Ga -di-HSG to visualize the tumors was followed by radioimmunotherapy using ^{177}Lu -di-HSG. Compared to direct radioimmunotherapy with anti-TROP-2 mAb (^{177}Lu -hRS7), the pretargeting strategy increased median survival, with no significant renal or hematological toxicity compared to intact antibody (van Rij et al., 2013).

Antibodies have also proven useful for imaging immune cell subsets, which has broad applications for imaging related to cancer, infection, autoimmune disease, and other types of inflammation. An overview of this application is discussed in Section 1.3.2.

1.3 CD4+ T cells

T lymphocytes, or T cells, are part of the adaptive immune system which is responsible for developing immunological memory to pathogens. T cells are commonly segregated into two main classes: CD8+ T cells, which have cytotoxic capabilities, and CD4+ T cells, which orchestrate the immune response. CD4+ T cells interact with and help B cells to produce antibodies, recruit and activate other immune cells to sites of inflammation, and regulate pro- and anti-inflammatory actions of immune cells to either stimulate or suppress immunity. Subsets of CD4+ T cells are defined in part by their cytokine profile and expression of key genes, by the cells they commonly interact with,

and the type of immune response they commonly produce (Figure 1.9). Major subsets of CD4⁺ T cells include Th1 (which recruit and activate neutrophils and macrophages, defend against intracellular pathogens, and often mediate autoimmunity), Th2 (which recruit and activate eosinophils, basophils, mast cells, and alternatively-activated macrophages, defend against extracellular parasites, and mediate allergy and asthma), Th17 (which recruit neutrophils, defend against extracellular bacteria, fungi, and also mediate autoimmunity), Tfh (follicular helper T cells, which induce production of antibodies by B cells), and Tregs (regulatory T cells, which mediate immune tolerance and regulate the immune response) (Janeway Jr et al., 2001; Zhu and Paul, 2008). Ongoing research in the field of T cell biology and differentiation suggests that there may



be even more major subsets of CD4+ T cells, and that within the known major subsets there are additional roles to be discovered (e.g. the relatively recent discovery of the role of Th17 in some autoimmune diseases).

Both CD4+ and CD8+ T cells are activated by recognition of antigen when it is presented by the major histocompatibility complex (MHC), expressed on the surface of antigen-presenting cells. All T cells express the T cell receptor (TCR) complex on their surface, which interacts with MHC to recognize antigen. CD4+ T cells only interact with MHC class II (MHC II), which presents antigen scavenged from the extracellular space. CD4 is a type 1 transmembrane glycoprotein comprised of four extracellular domains (ECD), a short transmembrane region, and a small intracellular domain which has binding sites for the tyrosine kinase Lck (Zola et al., 2007). Domains 3 and 4, closest to the cell membrane, interact with the TCR; domain 1 interacts with the β_2 -domain of MHCII. By interacting with both TCR and MHC II, CD4 is thought to stabilize this complex. The presence of CD4 increases sensitivity of the T cell to activation; 100-fold more antigen is required for activation when CD4 is absent. Only about 100 TCR:MHCII complexes are required for optimal activation when CD4 is present (Janeway Jr et al., 2001).

CD4 is also involved in the signaling cascade which occurs upon recognition of antigen. Central to the initiation of the pathway is the tyrosine kinase Lck, which phosphorylates cytosolic regions of the TCR, resulting in recruitment of other signal-potentiating proteins. Lck is closely associated with the cytosolic region of CD4; therefore, when CD4 binds to both CD3 and MHC II, Lck is within range of the TCR and can initiate the cascade (Janeway Jr et al., 2001)

The central role CD4+ T cells play in controlling the immune response contributes to their involvement in a variety of diseases and disorders. Depletion of CD4+ T cells is a hallmark of human immunodeficiency virus (HIV) infection, resulting in acquired immunodeficiency syndrome (AIDS) and leading to dangerous opportunistic infections (Okoye and Picker, 2013). There is also evidence of CD4+ T cell involvement in numerous autoimmune diseases (Palmer and Weaver, 2010). Multiple sclerosis, a progressive autoimmune disorder that results in demyelination and neurodegeneration, is thought to be mediated by aberrant autoreactive CD4+ T cells (Fletcher et al., 2010; Goverman, 2009). Rheumatoid arthritis is characterized by infiltration of Th1-type CD4+ T cells into the synovial tissue of joints (Norii et al., 2006), where they produce pro-inflammatory cytokines such as interferon- γ . An excessive T cell response is also a key feature of inflammatory bowel disease (Gálvez, 2014), which will be discussed in detail in Section 1.4. In the context of cancer, CD4+ T cells are responsible for mediating anti-tumor immunity and may influence the outcome of cancer immunotherapies (Zanetti, 2015).

1.3.1 Approaches to imaging immune cells

Clinical assessment of immune cells is commonly performed via flow cytometric or histological analysis of samples procured from peripheral blood draws or biopsies. Blood draws are relatively noninvasive and can be done serially to track changes over time. Biopsies give site-specific information about cells in the context of the tissue from which they are collected. However, both of these methods have clear disadvantages. Less than 2% of the body's lymphocytes exist in the peripheral blood at one time (Trepel, 1974), the vast majority residing in lymphoid tissues and other immune compartments,

so blood draws sample only a tiny percentage of the total immune cells. Furthermore, although the procedure can be repeated serially, the results can be highly variable on an intra-individual basis, as lymphocyte populations in the blood can change based on a number of factors including the time of day and physical exercise (Suzuki et al., 1997). Biopsies give site-specific information, but local inhomogeneity – for instance, in different regions of a tumor – can lead to incomplete data about the region. Therefore, a more comprehensive method would aid in complete assessment of immune cells throughout the body.

Molecular imaging provides a method of detection and tracking of immune cells *in vivo*. Non-invasive imaging based on cell surface biomarkers can provide valuable information about the localization and migration of immune cells, in an inherently dynamic system. Systemic *in vivo* imaging presents an exciting solution to this problem, extending the temporal and spatial nature of information that can be collected. Importantly, tracking immune cell subsets, key to differential immune responses, could provide *in vivo* insight into diagnosis, mechanisms, and treatment of inflammation, infection, autoimmunity, and other diseases. For example, inflammation accompanies the development of many malignancies. Tracking systemic cell localization would be especially advantageous in cell-based immunotherapy, wherein it is critical that modified immune cells successfully traffic to and reside in tumors. Immunomodulatory treatments (such as checkpoint inhibitor antibodies targeting CTLA-4 or PD-1/PD-L1 interactions) are dependent on the presence of appropriate immune cell subsets (such as CD8⁺ T lymphocytes). Immune system reconstitution following a hematopoietic stem cell

transplant could be non-invasively monitored, as could graft rejection and host-vs-graft disease after organ transplantation.

To date, several non-antibody-based methodologies have been used to track immune cells throughout the body, including targeted MRI, reporter gene technologies, nanoparticles, and *ex vivo* radiolabeling of immune cells for SPECT imaging (Ahrens and Bulte, 2013; Mandl et al., 2012; Nair-Gill et al., 2008; Weissleder et al., 2014). Cell tracking in humans is commonly done by performing SPECT imaging of *ex vivo* ^{111}In -oxine-radiolabeled white blood cells (Ahrens and Bulte, 2013). This method is costly and complex, as it requires the removal of leukocytes from the patient followed by labeling, reinfusion, and scanning. The probe also becomes diluted over time as cells divide (Nair-Gill et al., 2008). Reporter gene technology, in which cells are engineered to produce a protein marker that is the target of an imaging probe, is advantageous in that only cells that are genetically modified will produce a signal. The major limitation is that it requires genetic modification and thus is an invasive procedure (Nair-Gill et al., 2008). Nanoparticle-based imaging has been of particular interest for imaging macrophages due to their high endocytic activity (Weissleder et al., 2014), and intravital imaging has shown promise in preclinical models (Germain et al., 2012), but both could be significantly enhanced by incorporating antibodies in order to add specificity.

1.3.2 Antibody imaging of immune cells

Antibodies are advantageous for imaging immune cells because the ability to choose specific cell-surface biomarkers enables assessment of defined cell subsets.

Preclinical imaging studies using antibodies for several types of immune cells have been reported. For SPECT imaging of myeloid-specific suppressor cells, which are markers of the inflammatory microenvironment in tumors, Cheng et al. used a ^{99m}Tc -labeled anti-CD11b antibody (Cheng et al., 2015). The presence of tumor-infiltrating T cells in subcutaneous colon tumors was analyzed with PET using a ^{64}Cu -labeled anti-CTLA-4 mAb antibody (Higashikawa et al., 2014), and CD8⁺ T cells were imaged systemically with a ^{89}Zr -labeled minibody (Figure 1.10) (Tavaré et al., 2014a). Griessinger et al. used the internalization of the T cell receptor complex to their advantage so that they could stably label T cells for PET imaging (Griessinger et al., 2015). Imaging of B cells was conducted in a huCD20 transgenic mouse model using ^{64}Cu -labeled rituximab (Natarajan et al., 2012). Optical imaging with antibody probes has also been utilized to image immune cells. In a study of eosinophil recruitment to the airways during asthma, imaging with AlexaFluor-labeled anti-Siglec-F antibody showed accumulation of Siglec-F-expressing eosinophils in the lungs of affected mice (Markus et al., 2014). Natural killer cells labeled *ex vivo* with quantum dot-conjugated anti-CD56 were injected intratumorally into mice and imaged to monitor their presence in the tumor (Lim et al., 2009).

Antibodies and fragments have been used in humans to study several autoimmune diseases. In a phase I proof of principle study using ^{99m}Tc -labeled anti-CD4-Fab to image CD4⁺ T cells in patients with rheumatoid arthritis, 70% of clinically affected (painful or swollen) joints were positive on the scan (Steinhoff et al., 2014). The authors suggest that the low detection rate may be due to non-correlation between symptoms and presence of CD4⁺ T cells in the synovial joints, and that other cells may be involved in joint

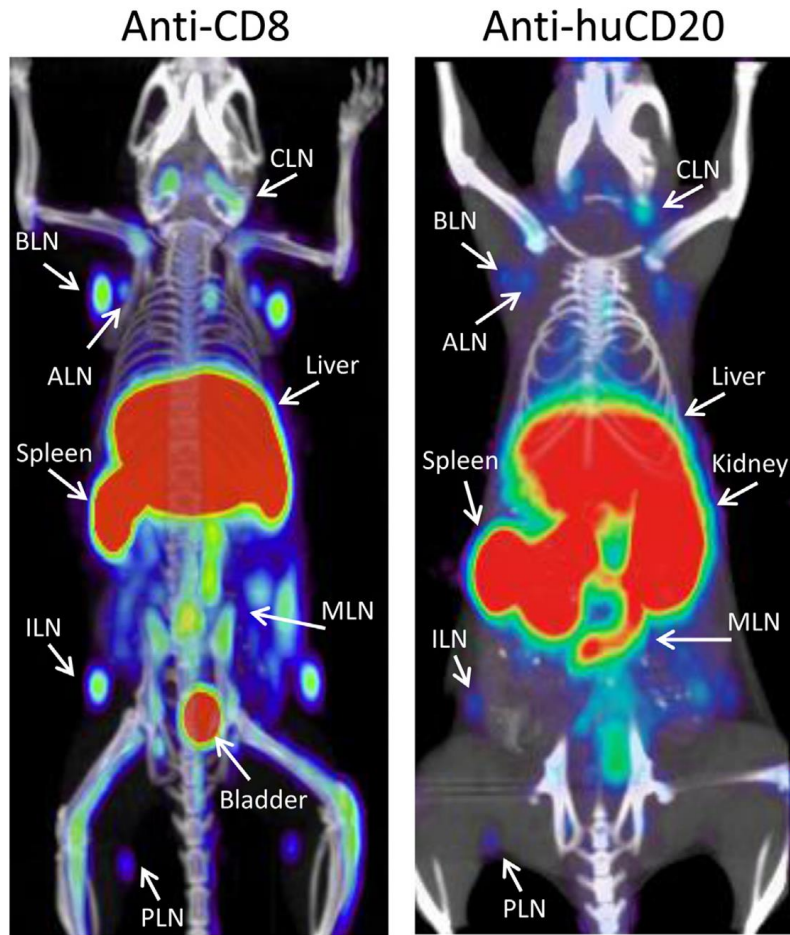


Figure 1.10 Imaging immune cells

Tracking CD8+ T cells could help detect and stage CD8+ lymphomas and aid in monitoring T cell immunotherapy. Here, imaging of CD8+ T cells with a ^{64}Cu -NOTA-anti-CD8 minibody in wild type mice visualizes the spleen and lymph nodes (left panel). ^{89}Zr -DFO-anti-huCD20 cys-minibody imaging of a transgenic mouse expressing huCD20 reveals B cells in the spleen and lymph nodes (right panel); this could also be applied for the detection of B-cell lymphomas. Reprinted from (Freise and Wu, 2015); original data from (Tavaré et al., 2014a; Zettlitz et al., 2013)

inflammation. Even so, this represents a potentially useful diagnostic application. In Crohn's disease, current treatments, including the antibody adalimumab, aim to neutralize the proinflammatory cytokine tumor necrosis factor alpha ($\text{TNF}\alpha$), but only 50% of patients respond to adalimumab and those that do not respond are exposed to potentially harmful side effects (Atreya et al., 2014). Atreya et al. addressed this need to stratify

patients by using fluorescently labeled adalimumab applied topically to inflamed regions of the bowel during a colonoscopy, followed by confocal laser endomicroscopy to quantify fluorescence. The response rate to subsequent adalimumab was correlated with the expression of $TNF\alpha$. Results suggested that prescreening with fluorescently-labeled antibodies can successfully segregate patients into responders and nonresponders (Atreya et al., 2014). A recent clinical study using ^{99m}Tc -labeled CXCL8 for SPECT imaging of neutrophils, CD8+ T cells, and macrophages in human inflammatory bowel disease found that the probe had good sensitivity for detecting active disease, but that its specificity was lower compared to traditional endoscopy (Aarntzen et al., 2016). The authors suggested that the probe could still be useful for making decisions regarding immune-modulating drugs. In sum, immunoPET is a promising new tool for improving assessment of immune cells in the context of numerous conditions, and may prove useful for not only detecting disease but also for predicting response to treatment.

1.4 Inflammatory bowel disease

1.4.1 Inflammatory bowel disease in humans

Inflammatory bowel disease (IBD) is a family of disorders which includes Crohn's disease and ulcerative colitis, both of which are characterized by inflammation in the bowel, have a genetic component, and can lead to increased risk of colon cancer (Kaser et al., 2010). Crohn's disease affects the entire gastrointestinal tract, while ulcerative colitis affects the colon. While the etiology of disease is not yet known, IBD is a

multifactorial disease, influenced by genetics, environmental factors, intestinal microbiota, and the immune system.

Both Crohn's disease and ulcerative colitis are characterized by an aberrant T cell response. In Crohn's disease, mucosal T cells have reduced apoptosis and expand faster than normal mucosal T cells, leading to inappropriate T cell accumulation (de Souza and Fiocchi, 2016). Historically, ulcerative colitis was thought to be an atypical Th2-driven response while Crohn's disease was thought to be Th1-driven; however, in the past decade, additional work in the field has shown that both diseases are driven by multiple, complex, and overlapping immune pathways (Bamias et al., 2016). For example, studies on the contribution of IL-17-producing Th17 CD4+ T cells in Th1-driven animal models of IBD has led to recognition of the role that Th17 cells play in Crohn's disease (de Souza and Fiocchi, 2016). Although much work remains to be done to fully understand the role of both innate and adaptive immune cells in IBD, it is clear that CD4+ T cells are involved and therefore they represent a potential target for both diagnosis and treatment of IBD.

Therapeutic agents targeting various aspects of IBD pathology have been identified and are routinely used in the clinic, but to limited success for many patients. Treatments include various antibodies and small molecules which deplete or inhibit T cells, inhibit intestinal T cell homing, and inhibit various pro-inflammatory cytokines (Cader and Kaser, 2013). Given the targeted nature of these therapeutics, careful study of the immunological effects would be beneficial not only for guiding future treatment decisions, but also to contribute to better understanding of immune dysregulation in IBD. Unfortunately, many clinical trials determine the outcome of investigational drugs in a binary fashion and rarely examine or report the immunological changes induced by

treatment (Cader and Kaser, 2013). Molecular imaging of immune cells or other biomarkers of gut inflammation could prove useful as a tool to rapidly and noninvasively investigate the effect of new therapeutics on a per-patient basis, in addition to detecting disease lesions and the severity of inflammation.

1.4.2 Clinical imaging of IBD

In IBD, multiple foci of inflammation can develop throughout the intestinal tract. Currently the standard methods of diagnosis and monitoring for IBD combines blood tests, endoscopy and endoscopy-guided biopsy; for Crohn's disease, occasionally contrast-enhanced X-rays are employed (Hendrickson et al., 2002). While routine, endoscopic evaluation of disease carries a small risk of bowel perforation, which is increased in patients with bowel inflammation. Repeated endoscopies are uncomfortable for patients; furthermore, invasive procedures are especially undesirable in pediatric patients. Therefore, noninvasive imaging could enable visualization of the entire intestine while avoiding, or at least decreasing the frequency, of intrusive procedures such as endoscopy.

Several nuclear imaging approaches have been used to image IBD (McBride, 2010). Cell tracking studies have been done using ^{99m}Tc -hexamethylpropyleneamine oxime (^{99m}Tc -HMPAO)-radiolabeled autologous lymphocytes, which can be reinfused and imaged with SPECT to identify regions of inflammation; in one clinical study, responders to cyclosporin A immunosuppressive treatment had significantly lower levels of ^{99m}Tc -HMPAO-labeled lymphocyte accumulation after treatment, whereas nonresponders did not (Bennink et al., 2004). Another common imaging agent is ^{18}F FDG, which can be

used to identify regions of inflammation with PET. Normal physiological uptake of FDG in the gut is variable which may reduce its utility as a general screening tool (Aarntzen et al., 2016), but it has found success in imaging patients with known active IBD; a meta-analysis of multiple clinical studies found that [¹⁸F]FDG had an estimated sensitivity of 85% and specificity of 87% in IBD patients (Treglia et al., 2013). Immune targets including granulocytes (Bruno et al., 2002), E-selectin (Bhatti et al., 1998), and CXCL8 (Aarntzen et al., 2016) have been imaged in IBD patients. As of yet, CD4+ T cells have not been targeted for imaging in IBD patients. Additional targets have been imaged in murine models of IBD, which will be discussed in Chapter 4.

1.4.3 Dextran sulfate sodium mouse model of inflammatory bowel disease

Multiple murine models of IBD have been characterized to determine contributions by various subsets of immune cells. The dextran sulfate sodium (DSS) model of colitis is the most widely used model, due to its simplicity, reproducibility, and similarities to human ulcerative colitis (Chassaing et al., 2014). DSS, a polysaccharide, is administered in drinking water to induce colitis, which typically develops in less than a week. DSS causes damage to the epithelial layer, allowing luminal contents (such as bacteria) to infiltrate the tissue and inducing inflammation as a result.

The DSS model is typically used to investigate innate immune contributions, as initial damage is caused by massive influx of neutrophils. Furthermore, colitis can be induced with DSS in mice depleted of CD4+ T cells, athymic mice, SCID mice, and NK-cell depleted SCID mice (Axelsson et al., 1996; Dieleman et al., 1994). However, the contribution of CD4+ T cells to DSS colitis is still controversial. Although the DSS model

does not require T cells for induction of colitis, they still infiltrate into the colon (Hall et al., 2011), and CD4⁺ T cells appear to play a role in the chronic stage of colitis, after DSS administration ceases and mice begin recovery (Dieleman et al., 1998; Melgar et al., 2005). Adoptive transfer of DSS-primed CD4⁺ T cells into recipient mice treated with DSS exaggerated colitis (Shintani et al., 1998). In another study, adoptive transfer of Qa-1-restricted CD8⁺ Treg cells (which suppress CD4⁺ T cell activation) into colitic mice or depleting CD4⁺ T cells both resulted in mild reduction of signs of colitis (Yao et al., 2013). Conversely, athymic CD-1 nu/nu mice treated with DSS developed more severe clinical signs of colitis than normal mice, suggesting that T cells may be protective in DSS colitis (Axelsson et al., 1996). Further investigation into the role of CD4⁺ T cells in DSS colitis is needed to fully understand when and how they affect the progression of the disease, and imaging provides a useful tool for comprehensive analysis of these cells.

Molecular imaging has been used to assess inflammation in murine models of colitis. [¹⁸F]FDG was used in the dextran sulfate sodium (DSS) model of colitis to detect inflammation at several time points during progression of acute disease (Hindryckx et al., 2011), and to correlate uptake in the colon with histologic damage and expression of perforin (Bettenworth et al., 2013), indicating that PET may serve as an effective tool for noninvasively monitoring disease severity. [¹⁸F]FDG has also been utilized to identify inflammation in several models with mild or severe chronic colitis, including the CD4⁺CD45RB^{high} and Gαi2^{-/-}CD3⁺ T cell transfer models (Brewer et al., 2008). For investigation into the specific subsets of cells involved in IBD, a more specific probe is required. Molecular imaging with antibodies enables imaging and quantitation of cell-surface biomarkers, and antibodies have been used to image immune cell biomarkers in

models of colitis. Kanwar et al. used a non-depleting intact anti-CD4 antibody for SPECT imaging of CD4⁺ T cells in acute DSS colitis, and showed that uptake in the lower abdomen correlated with disease severity and the number of CD4⁺ T cells present (Kanwar et al., 2008). The integrin β_7 subunit, expressed on lymphocytes activated in Peyer's patches and mesenteric lymph nodes, was recently used as a target for SPECT imaging in DSS-treated colitic mice (Dearling et al., 2010). These studies used intact antibodies, which typically require several days after probe injection for enough to clear to produce a high-contrast image; engineering antibodies into fragments of various sizes allows customization of pharmacokinetics and radiolabeling strategies, enabling same- or next-day imaging (Freise and Wu, 2015). Dearling et al. developed fragments of the anti-integrin β_7 probe and showed that they could also be used to image lymphocytes in the guts of colitic mice (Dearling et al., 2016).

In Chapter 4, the use of an anti-CD4 antibody fragment, GK1.5 cys-diabody, to image CD4⁺ T cells in DSS-treated mice is described. In Chapter 5, GK1.5 cys-diabody is used to investigate treatment success in the DSS model.

2 GK1.5 cys-diabody

2.1 History and applications of intact GK1.5 antibody

The discovery of intact GK1.5 antibody was published in 1983 by Dialynas et al., who were attempting to identify cell surface molecules involved in antigen-specific cytotoxicity by murine T cells (Dialynas et al., 1983). They screened over 4000 hybridoma lines to find an antibody with cytotoxicity-blocking activity, and identified GK1.5, a rat monoclonal anti-mouse CD4 (named anti-L3T4a at the time) antibody. Characterization of GK1.5 demonstrated that it had the following functional effects: blocking of MHCII antigen-specific cytotoxicity, blocking of MHCII antigen-specific proliferation at the induction stage, and blocking of antigen-driven release of IL-2, colony-stimulating factor, and interferon (Dialynas et al., 1983). The authors note that since GK1.5 blocked antigen-driven functions, the most likely mechanism was that GK1.5 blocks antigen recognition. Further characterization of GK1.5 found that the functional effect of GK1.5 on T cell proliferation and cytokine release was time-specific: inhibition only occurred if GK1.5 was added within 3 hours of culture initiation (Wilde et al., 1983). This inhibitory effect was dose-dependent: incomplete inhibition of IL-2 release could be produced if the concentration of GK1.5 was titrated down (Wilde et al., 1983).

The valency of GK1.5 modulates its effects on CD4+ T cells. The mechanism of action of GK1.5 on T cell activation and proliferation were investigated by Haque et al. with intact IgG and a monovalent Fab fragment of GK1.5. The Fab fragment was still able to block antigen-specific activation of T cells, although about the concentration of the Fab

fragment needed to be about 5-fold that of the IgG, possibly due to decreased affinity (Haque et al., 1987). The Fab fragment was unable to block antigen-independent activation by phytohemagglutinin (PHA), a lectin that induces T cell activation independently of MHC II:TCR coupling; the IgG did block PHA-induced activation. The authors suggested that the inhibitory activity of the Fab fragment is due to steric hindrance of the MHC II:CD4 interaction (Haque et al., 1987), a hypothesis supported by results showing that the epitope bound by GK1.5 is in Domain I of CD4 (Dianzani et al., 1992), the domain responsible for interacting with MHC II and stabilizing the complex. Interestingly, T cell activation induced by anti-TCR antibodies was augmented by intact GK1.5 but not by the Fab fragment, indicating that concurrent TCR crosslinking is required in order for GK1.5 to stimulate activation, and that GK1.5-induced crosslinking and internalization of CD4 in the absence of TCR crosslinking results in inhibition of activation (Haque et al., 1987).

The function for which GK1.5 is best known is its depleting activity on CD4+ cells in mice. GK1.5 is a complement-fixing antibody but its depleting function is independent of C1q and C5, and also of antibody-dependent cell-mediated cytotoxicity (ADCC) (Csencsits et al., 2008; Ghobrial et al., 1989). Compared to CD4+ lymphocytes from the spleen, blood, and lymph nodes, thymocytes required a 1000-fold higher dose of GK1.5 (produced from ascites fluid) to achieve even partial depletion (Ghobrial et al., 1989). In comparative studies using purified GK1.5 mAb, the authors suggest that 10-100 µg GK1.5 is sufficient for depletion of CD4+ T cells from blood and lymph nodes, whereas 20 mg would be required for complete depletion of CD4+ thymocytes (Ghobrial

et al., 1989); this finding becomes especially relevant in the imaging studies described below, because GK1.5 cDb does not image the thymus.

Given the known functional effects of intact GK1.5 as well as its fragments, it was crucial to identify whether GK1.5 cys-diabody had biological activity as well. Biological and functional characterization of GK1.5 cDb is described in Chapter 3. Here, a summary of the methods for production, purification, and labeling of GK1.5 cDb is provided. Reformatting of intact GK1.5 into GK1.5 cDb was performed by Dr. Richard Tavaré, and relevant methodological details were published in (Tavaré et al., 2015).

2.2 Expression and production of GK1.5 cDb

A mammalian expression system was used to produce GK1.5 cDb. HEK293-F cells (Life Technologies) were cultured in DMEM/10% fetal calf serum (FCS)/1% non-essential amino acids. 1×10^6 cells were plated in a 6-well plate in 2 mL medium. On the following day cells were washed with phosphate-buffered saline (PBS), and 1.6 mL OptiMEM reduced-serum media (Gibco) was added to the cells. 6.7 μ L Lipofectamine™ 2000 (Invitrogen) was mixed with 166 μ L OptiMEM and incubated for 5 minutes. 2.7 μ g pSec-GK1.5 cDb DNA was added to 166 μ L OptiMEM, mixed with the Lipofectamine, and allowed to incubate for 20 min at room temperature. The Lipofectamine-DNA mixture was then added to cells. After 6 hours media was replaced with new OptiMEM. 24 hours later, cells were diluted 1:10 in growth media. The next day, cells were treated with Zeocin (InvivoGen) at 300 μ g/mL to create a stable cell line. Selective media was changed every 72 hours to replace consumed Zeocin. Cells were expanded into triple flasks and cultured in OptiMEM to enhance protein production. GK1.5 cDb expression was monitored by

SDS-PAGE and anti-HIS western blot detection. Supernatant containing secreted protein was collected every 3-4 days. Sodium azide was added to a final concentration of 0.02% to inhibit microbial growth, and supernatant was stored at 4°C. For a typical production, up to 1 L of supernatant per triple flask was collected.

2.3 Purification of GK1.5 cDb

Supernatant was filtered using a Stericup 0.22 µm vacuum filter (Millipore). A Labscale liquid concentrator (Millipore) fitted with a 10 kDa molecular weight cutoff nitrocellulose filter (Pelicon) was used to concentrate supernatant down to a final volume of ~50 mL. Concentrated supernatant was filtered again with a Steriflip 0.22 µm filter unit (Millipore), and imidazole was added to the concentrate to a final concentration of 20 mM. The concentrate was purified using an imidazole gradient with a 1 mL HisTrap HP nickel-exchange column (GE) fitted to an ÄKTA fast protein liquid chromatography purifier (GE);

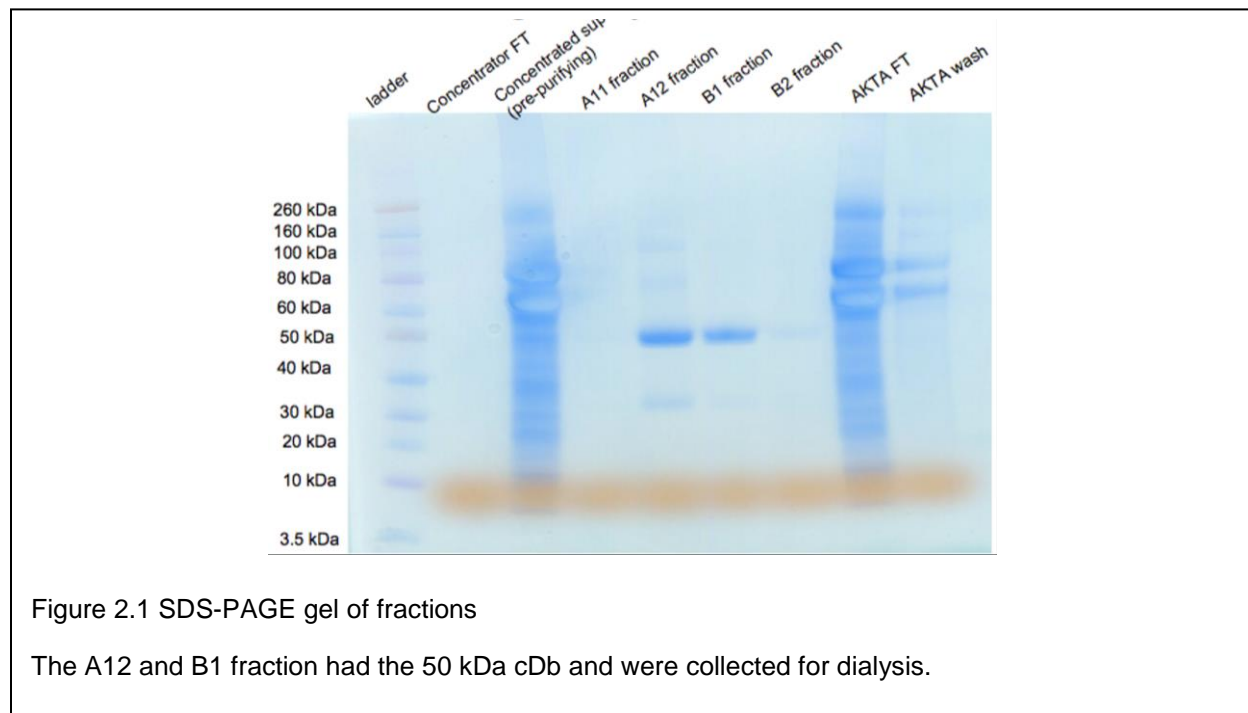


Figure 2.1 SDS-PAGE gel of fractions

The A12 and B1 fraction had the 50 kDa cDb and were collected for dialysis.

20 mM imidazole was used to load the supernatant, and a three-step gradient up to 500 mM imidazole was used to elute. Fractions containing the protein of interest as determined by SDS-PAGE (Figure 2.1) were collected, combined, and dialyzed three times against PBS using a 3-12 mL Slide-a-Lyzer dialysis cassette (Thermo Fisher). Protein was concentrated again using an Amicon 2 mL spin column (Millipore). The final concentration was determined using a Nanodrop 2000 spectrophotometer (Thermo). The average yield of GK1.5 productions was 0.3 mg/L (n=8 productions).

2.4 Conjugation and labeling of GK1.5 cDb

GK1.5 cDb was reduced with 20-fold molar excess of tris (2-carboxyethyl) phosphine hydrochloride (TCEP; stock: 20 mM Pierce) for 30 min at room temperature. Site-specific conjugation was performed by incubating reduced GK1.5 cDb with 20-fold molar excess of maleimide-desferrioxamine (malDFO; stock: 20 mM; Macrocyclics) for radiolabeling, or 20-fold molar excess of maleimide-biotin (malBiotin; stock: 20 mM; Sigma) for affinity studies, for 2 hours at room temperature. Conjugated protein was purified on a Micro BioSpin 6 column (Bio-Rad); approximately 10-20% of the protein was lost during spin column purification, so additional protein was reduced and conjugated to take this loss into account. A typical reduction and conjugation experiment would use approximately 150 µg protein from a stock of 1-3 mg/mL, and volumes of TCEP and malDFO or malBiotin would be less than 2 µL each; this would result in at least 100 µg conjugated protein for use in later experiments.

For radiolabeling, ⁸⁹Zr-oxalate (3D Imaging) was incubated with 40% (v/v) 2 M Na₂CO₃ and allowed to incubate for 3 min at room temperature. A 2.5x volume of 1M N-

(2-hydroxyethyl)piperazine-*N*-(2-ethanesulfonic acid) (HEPES; pH 7.0) was added to the activity. pHydrion pH indicator strips (Micro Essential Laboratory) were used to confirm that the pH of the activity was between 6.8-7.2. malDFO-GK1.5 cDb and activity were then mixed at a ratio of about 6 $\mu\text{Ci}/1 \mu\text{g}$ and incubated for 1 hour at room temperature; a typical reaction contained 100 μg malDFO-GK1.5 and 600 μCi (added in less than 5 μL) in a total volume of 100 μL . Radiolabeling efficiency was determined by pipetting approximately 1 μL of the reaction mixture onto an instant thin-layer chromatography strip (Biodex Medical Systems), using 20 mM citrate buffer (pH 5.6) as the mobile phase. Strips were cut in half to separate the region containing protein (region 1) and the region with free activity (region 2), and activity of each region was measured in counts per minute (CPM) using a Wizard 3" 1480 Automatic Gamma Counter (Perkin-Elmer). Radiolabeling efficiency (RE) was calculated as follows:

$$\text{RE} = 100 * (\text{CPM region 1}) / (\text{CPM region 1} + \text{CPM region 2})$$

^{89}Zr -malDFO-GK1.5 cDb was purified using a Micro BioSpin 6 column (Bio-Rad) equilibrated with 2% FCS in PBS, and radiochemical purity was then assessed in the same manner as the radiolabeling efficiency. Specific activity was calculated as follows:

$$\text{Specific activity} = (\text{activity incubated with protein}) * (\text{RE}) / (\text{mass of protein})$$

Purified ^{89}Zr -malDFO-GK1.5 cDb was diluted in sterile PBS so that the desired administered activity could be delivered intravenously in a volume of 100 μL , and doses were drawn into 0.5 cc syringes. The activity in each syringe was measured using a dose calibrator (AtomLab).

3 ImmunoPET imaging of murine CD4⁺ T cells using anti-CD4 cys-diabody: Effects of protein dose on T cell function and imaging

3.1 Introduction

CD4⁺ T cells orchestrate the immune system, guiding both pro- and anti-inflammatory responses. The CD4 co-receptor interacts with the T cell receptor (TCR) complex and the major histocompatibility complex class II (MHC II), which is expressed on antigen presenting cells, to increase CD4⁺ T cell sensitivity to antigen. Upon antigen recognition, CD4⁺ T cells become activated, proliferate, produce cytokines for immune cell recruitment and activation, and assist B cells to produce antibodies and activate other immune cells (Zhu and Paul, 2008). As a consequence of their role in regulating immunity, accurate measurement of CD4⁺ T cells has implications for monitoring and treatment of a variety of diseases and disorders, including HIV infection (Byrareddy et al., 2016; Di Mascio et al., 2009), autoimmune diseases such as rheumatoid arthritis (Becker et al., 1990; Steinhoff et al., 2014) and inflammatory bowel disease (Kanwar et al., 2008), and cancer (Zanetti, 2015). Current methods of collecting CD4⁺ T cells include peripheral blood draws, which are relatively noninvasive, and biopsies, which allow testing from a precise location of interest. However, these methods give a limited representation of tissue-resident CD4⁺ T cells throughout the immune system (McCracken et al., 2016). In humans only $\leq 2\%$ of total lymphocytes are in the blood at any time; the majority reside

in lymphoid tissues (e.g. spleen and lymph nodes) as well as in non-lymphoid organs (Trepel, 1974; Westermann and Pabst, 1992). Biopsies can sample solid tissues, but are invasive and can give variable results due to CD4⁺ T cell inhomogeneity. Furthermore, growing interest in tumor-infiltrating lymphocytes and the influence of CD4⁺ T cells on the outcome of cancer immunotherapy (Zanetti, 2015) suggests a need for measurement of T cells throughout the entire tumor and nearby lymphoid organs (Tavaré et al., 2016). For a comprehensive assessment of CD4⁺ T cells, a method that can simultaneously survey CD4⁺ T cell reservoirs throughout the body is desirable.

Radionuclide-based molecular imaging, including positron emission tomography (PET) and single photon emission computed tomography (SPECT), enables sensitive, noninvasive, whole-body imaging of cells, biomarkers, and cellular processes. Sites of inflammation can be identified by adoptive transfer of *ex vivo* radiolabeled autologous lymphocytes and tracking their migration after reinfusion. This is done clinically using ¹¹¹In-oxine or ^{99m}Tc-hexamethylpropyleneamine oxime (^{99m}Tc-HMPAO) to track cells with SPECT (McCracken et al., 2016); for tracking lymphocytes using PET, ⁸⁹Zr- and ⁶⁴Cu-labeled probes are emerging as effective candidates (Griessinger et al., 2015; Sato et al., 2015). To image an endogenous subset of cells, the targeting of a biomarker-specific probe is required. Antibody-based imaging (immunoPET or immunoSPECT) combines the exquisite specificity of antibodies and the sensitivity and tissue penetration of nuclear imaging to noninvasively image and quantitate endogenous cell surface biomarkers. Radiolabeled antibodies have been used to image CD4⁺ T cells, mainly in preclinical settings. Rubin et al. utilized ¹¹¹In-labeled GK1.5 anti-CD4 antibody to assess distribution of murine CD4⁺ T cells with gamma camera imaging (Rubin et al., 1996). In a murine

model of colitis, ^{111}In -labeled YTS 177 non-depleting anti-CD4 antibody was used for SPECT imaging of excess CD4⁺ T cells in the gut (Kanwar et al., 2008). ImmunoSPECT with ^{111}In -labeled anti-CD4 antibody enabled tracking of CD4⁺ T cells in simian-HIV-infected rhesus macaques, and *ex vivo* biodistribution data was used to revise the proposed number of total lymphocytes in the human body (Di Mascio et al., 2009). Clinical use of anti-CD4 immunoSPECT has been explored in the context of rheumatoid arthritis with mixed results. Uptake in inflamed joints correlated well with clinical symptoms in one study, which utilized intact $^{99\text{m}}\text{Tc}$ -labeled anti-CD4 antibody Max.16H5 (Becker et al., 1990), but in a later study, a $^{99\text{m}}\text{Tc}$ -labeled Fab fragment of the same antibody identified only 68% of clinically affected joints (Steinhoff et al., 2014). These results led the authors to suggest that the presence of CD4⁺ T cells does not always correlate with pain and swelling in arthritic joints.

A major concern in the development of new PET tracers is the effect on target cells. Ideally, a tracer should have minimal effects on cell viability and function. Intact antibodies mediate effector function via the Fc region and can induce depletion of or functional changes in cells expressing the target antigen. For example, intact rat anti-mouse CD4 antibody GK1.5 depletes CD4⁺ T cells *in vivo* and can affect induction of proliferation and cytokine release (Dialynas et al., 1983; Haque et al., 1987; Wilde et al., 1983). In addition, intact antibodies have a long half-life (serum $t_{1/2}$ = 1-3 weeks) due to recycling through the neonatal Fc receptor, and require several days of clearance to acquire a high-contrast image. To address the drawbacks of Fc-mediated effector functions and long half-life, antibodies can be engineered into various fragments with

customized pharmacokinetics, conjugation capabilities, Fc receptor binding ability, and excretion route (Freise and Wu, 2015).

We previously developed an anti-CD4 antibody fragment, GK1.5 cys-diabody (cDb), for immunoPET imaging of murine CD4⁺ T cells and described its use in monitoring CD4⁺ T cell reconstitution after hematopoietic stem cell transplantation (Tavaré et al., 2015). GK1.5 cDb lacks the Fc region and clears rapidly through the kidney, enabling same- or next-day imaging. Subsequent studies demonstrated that GK1.5 cDb caused decreased surface expression of CD4, which prompted investigation of the potential impact of GK1.5 cDb on CD4⁺ T cells. Here, the effects of GK1.5 cDb dose on CD4⁺ T cell biology and immunoPET imaging were explored. A series of protein doses was evaluated for changes on T cell surface CD4 expression, antigen-driven proliferation, cytokine production, immunoPET image contrast, and biodistribution.

3.2 Materials and Methods

3.2.1 Animals

Female C57BL/6 and OT-II (B6.Cg-Tg(TcraTcrb)425Cbn/J) mice between 6-12 weeks of age were obtained from Jackson Laboratories and housed by the Department of Laboratory Animal Medicine at the University of California, Los Angeles (UCLA). Animal studies were conducted under protocols approved by the Chancellor's Animal Research Committee at UCLA. All applicable institutional and/or national guidelines for the care and use of animals were followed.

3.2.2 Conjugation and labeling of GK1.5 cDb

GK1.5 cDb production, conjugation, and labeling are described in detail in Chapter 2. Briefly, GK1.5 cDb was reduced with tris (2-carboxyethyl) phosphine hydrochloride (TCEP; Pierce) and site-specifically conjugated with maleimide-desferrioxamine (malDFO; Macrocyclics) for radiolabeling, or maleimide-biotin (malBiotin; Sigma) for affinity studies. In this work, malDFO-GK1.5 cDb (272 μ g) was radiolabeled with Zr-89 (40.3 MBq; 3D Imaging), purified, and labeling efficiency and radiochemical purity were assessed with instant thin layer chromatography.

3.2.3 Production of soluble murine CD4

Polymerase chain reaction (PCR) was used to amplify DNA encoding the extracellular domain of murine CD4 (Lys1 – Val360) from the complete mouse CD4 sequence (Sino Biologics). 5' *AgeI* and 3' *NotI* restriction digest sites (underlined) were added during amplification using the following primers: Forward primer: 5' – CACACAACCGGTAAGACGCTGGTGCTGGGGAA; reverse primer: 5' – TGTGTGCGCCCGCAACCTGGATCCTGGAGTC. The PCR product was digested with *AgeI* and *NotI* (New England Biolabs) and inserted into the TOPO subcloning vector which previously contained the 2.43 minibody (Tavaré et al., 2014a), to add a 5' mouse Ig Kappa secretion signal sequence and a 3' hexahistidine tag. *XbaI* and *EcoRI* (New England Biolabs) were then used to subclone the sCD4-His into the mammalian expression vector pEE12 (Lonza). Sequence verification was performed at the GenoSeq core at UCLA. NS0 electroporation, clonal selection using Ni-NTA HisSorb plates (Qiagen), protein production, and Ni-NTA purification were performed using previously

described methods (Tavaré et al., 2014a) except anti-CD4 (clone GK1.5; UC San Francisco Monoclonal Antibody Core) and alkaline phosphatase-conjugated anti-rat Fc (Sigma) were used to detect sCD4-His on the HisSorb plates. Concentrations of purified sCD4 or GK1.5 cDb were determined by measuring UV absorbance at 280 nm with a NanoDrop spectrophotometer (Thermo) and using the calculated molecular weight and the theoretical extinction coefficient (Geneious).

3.2.4 Soluble antigen binding assays

For the enzyme-linked immunosorbent assay (ELISA), 96-well high-binding polystyrene plates (Costar) were coated overnight at 4°C with 100 µL of 5 µg/mL soluble murine CD4. The next day, plates were washed and blocked with 2% non-fat milk (Bio-Rad) in PBS for 2 hours at room temperature. GK1.5 cDb-malBiotin or biotinylated GK1.5 Ab (Biolegend) were serially diluted (1:4 dilutions; 500 nM-0.0085 nM, in triplicate) in 2% non-fat milk and added to the plate for a 1 hour incubation. After washing with 0.1% PBS-Tween, streptavidin-alkaline phosphatase (Jackson ImmunoResearch) was added at a dilution of 1:2500 for 15 minutes, washed, and detected using *p*-nitrophenyl phosphate substrate (Sigma). Absorbance at 405 nm was read using an Infinite m200 Pro plate reader (Tecan). Affinities were estimated using a one site – specific binding model in Prism (GraphPad).

To investigate complex formation, soluble murine CD4 and GK1.5 cDb were incubated at a mass ratio of 2:1 at room temperature for 10 minutes and chromatographed on a Superdex 75 (GE) size exclusion chromatography (SEC) column using PBS for running buffer.

3.2.5 ImmunoPET imaging and biodistribution

MicroPET and microCT imaging was performed as described previously (Tavaré et al., 2015). A range of ^{89}Zr -malDFO-GK1.5 cDb doses (2-40 μg ; 0.26-5.2 MBq) were prepared in 100 μL saline and injected intravenously into mice. Mice were anesthetized with 2% isoflurane and PET and CT images were acquired 20 h post-injection. MicroPET images were acquired on an Inveon PET (Siemens) scanner for 600 sec and reconstructed using a 3D-ordered subset expectation maximization (OSEM) algorithm with 2 iterations, followed by maximum *a posteriori* (MAP) with 18 iterations (beta=0.1) with a zoom factor of 2.1, without attenuation correction. Whole-body CT images were acquired using the MicroCAT II (Imtek) scanner, with the x-ray source based at 70 kVp and 500 μA and an exposure time of 180 s (0.5 s per projection). A Feldkamp reconstruction algorithm was applied (Feldkamp et al., 1984). A Medical Imaging Data Examiner (AMIDE) software (<http://amide.sourceforge.net>) was used to view PET and CT scans. Images are displayed as 25 mm (coronal) or 2 mm (transverse) maximum intensity projections (MIP). Following the final PET/CT scan, *ex vivo* biodistribution was performed. Organs were removed, weighed, and counted in a Wizard 3" automatic gamma counter (Perkin Elmer) and the decay-corrected percent injected dose/gram (% ID/g) for each organ was calculated.

3.2.6 Flow cytometry

Blood from euthanized C57BL/6 mice was collected in a heparinized tube. Thymus, lymph nodes, and spleen were harvested and single-cell suspensions prepared

by mashing organs through 70 µm nylon filters using a syringe plunger. Filters were rinsed with PBS/2% FBS and red blood cells were lysed with RBC Lysis Buffer (Biolegend). Cells were then incubated in PBS/2% FBS for 15 minutes on ice, and stained for 30 min on ice with the following fluorescently labeled antibodies: anti-CD45-PE/Dazzle (clone 30F11), anti-CD4-PE (RM4-4), anti-CD4-BV421 (GK1.5), anti-CD8-AlexaFluor 700 (53.67) (Biolegend), and anti-CD3-APC (17A2; eBioscience). Stained cells were washed twice and analyzed on a BD Fortessa SORP X-20 flow cytometer. Blood and organs from individual mice were processed and stained as single samples. Data were analyzed using FlowJo analysis software (FlowJo LLC).

For analysis of changes in CD4 expression, C57BL/6 mice were injected with 2 or 40 µg GK1.5 cDb (n=3-4 mice/group). After 24 or 72 hours, blood, spleen, inguinal lymph nodes, and thymus were processed as above and the mean fluorescence intensity (MFI) of CD4 (BV421 or PE) by CD45⁺ cells was calculated for each organ. The average MFI for each organ in the untreated control group was designated as 100% (maximum), and individual values from experimental mice were compared to the maximum to evaluate modulation of CD4 expression. Change in expression is reported as mean ± standard deviation per experimental group of mice.

3.2.7 Proliferation assays

CD4⁺ T cells were isolated from the spleen and inguinal lymph nodes of C57BL/6 or OT-II mice. Organs were harvested, mashed through a mesh filter and washed with PBS/2% FBS. Negative selection was performed using the EasySep™ Mouse CD4⁺ T Cell Isolation Kit and EasySep magnet (StemCell Technologies). Purity was ~93% as

determined by flow cytometry. Cells were labeled with 5 μ M carboxyfluorescein succinimidyl ester (CFSE; Life Technologies) according to a published protocol (Quah et al., 2007).

To assay antigen-specific T cell proliferation, wild type C57BL/6 splenocytes were plated in 96-well plates (2×10^5 cells/well, in triplicate) and incubated overnight in the presence of 1 mg/mL ovalbumin (OVA) (Sigma). 24 hours later, 1×10^5 CFSE-labeled OT-II CD4⁺ T cells were added to the splenocytes, followed immediately by addition of various concentrations (0-100 nM, in triplicate) of GK1.5 cDb. Proliferation was assayed 72 hours later using flow cytometry. The proliferation platform of FlowJo was used to calculate percent divided (the percent of CFSE-labeled cells that divided at least once) and replication index (the fold-expansion of divided cells).

To assay antigen-specific T cell proliferation *in vivo*, 2×10^6 CFSE-labeled OT-II CD4⁺ T cells were injected intravenously into C57BL/6 recipients. 24 hours later, mice were intravenously administered PBS, 100 μ g OVA, 100 μ g OVA + 2 μ g GK1.5 cDb, or 100 μ g OVA + 40 μ g GK1.5 cDb. After 72 hours, the spleen, ILN, thymus, and blood were harvested, processed, and analyzed with flow cytometry to determine extent of proliferation.

3.2.8 Cytokine assays

Cytokine analysis was performed by the Immune Assessment Core at UCLA, using the ProcartaPlex Mouse Essential Th1/Th2 Cytokine Panel (6 plex) (eBioscience). Briefly, 50 μ L undiluted supernatant samples from the *in vitro* CD4⁺ T cell proliferation assays (in duplicate) were mixed with 50 μ L magnetic beads and incubated overnight at 4°C, with

shaking for 30 minutes before and after the incubation period. Plates were then washed three times manually with manufacturer-supplied wash buffer. 25 μ L of biotinylated detection antibody was added and incubated for 30 min at room temperature. After three washes, 50 μ L streptavidin-phycoerythrin conjugate was added to the reaction mixture and incubated for 30 minutes at room temperature. Following an additional three washes, beads were resuspended in manufacturer-supplied reading buffer and shaken for 5 min at room temperature. Fluorescence was quantified using a Luminex FLEXMAP 3D instrument. Data were analyzed using MILLIPLEX Analyst 5.1 software.

3.2.9 Statistical analysis

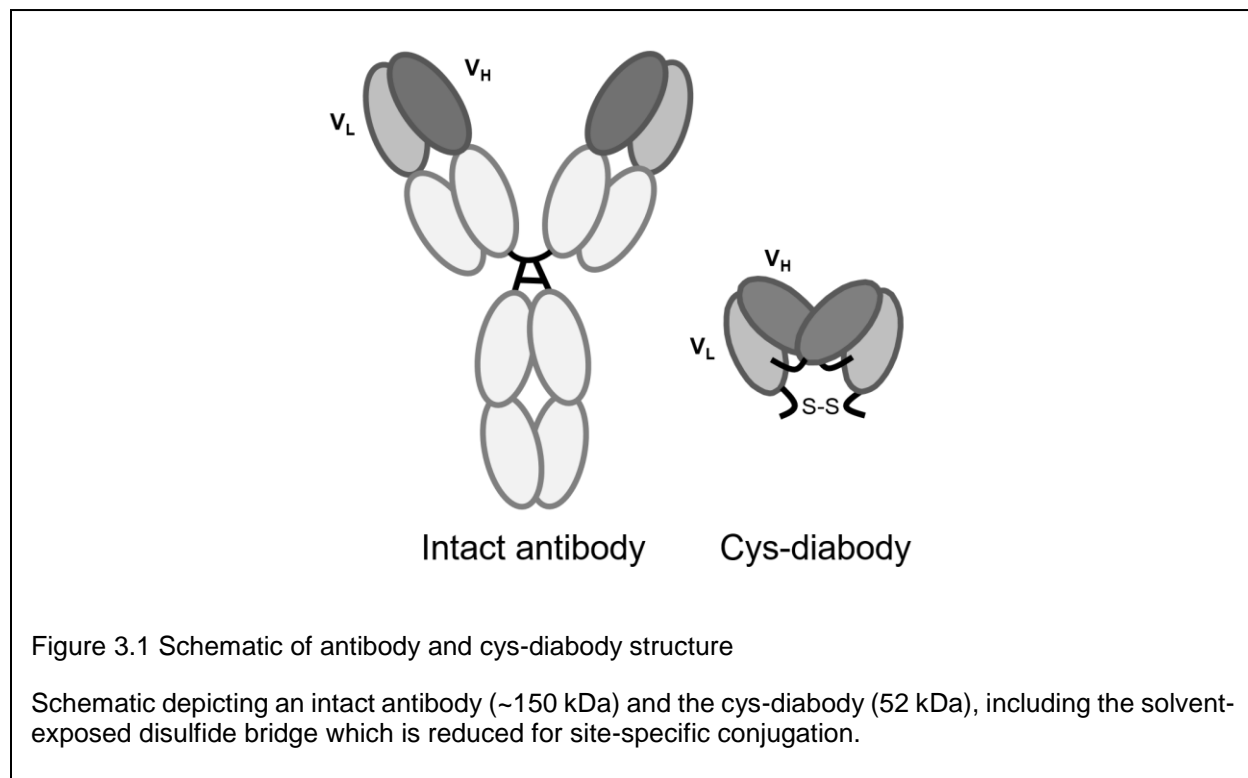
Summary statistics (means, standard deviations, and standard errors) were computed for each group. Two-sample Student's t-tests were used to compare the means of outcome measurement between groups. To correct for multiple comparisons in evaluating multiple organs and dosages in the *ex vivo* biodistribution study and the studies involving *in vivo* administration of GK1.5 cDb, the false discovery rates in the Benjamini-Hochberg step-up procedure (Benjamini and Hochberg, 1995) have been reported with a 5% threshold for significance.

Unless indicated otherwise, values are reported as mean \pm standard deviation. For flow cytometry assays, cytokine assays, and imaging experiments, experimental groups were compared individually to control groups. For the GK1.5 cDb dose escalation imaging and *ex vivo* biodistribution studies, the 2, 6, and 40 μ g protein doses were compared to the previously published 12 μ g protein dose [18]. Analyses of experimental data were performed using Prism (GraphPad; version 7) and SAS (SAS Institute; version 9.4).

3.3 Results

3.3.1 GK1.5 cDb retains specificity and affinity for murine CD4

GK1.5 cDb is a covalent dimer of two single-chain variable fragments (Figure 3.1). To confirm that GK1.5 cDb binds to CD4, antibody-antigen complex formation in solution was assayed by SEC. Free sCD4 (50 kDa) and free GK1.5 cDb (52 kDa) eluted as separate peaks; after incubation of sCD4 and GK1.5 cDb at a 2:1 molar ratio, a major peak representing a higher molecular weight complex eluted (Figure 3.3) To evaluate the affinity for GK1.5 cDb to CD4, a saturation binding assay was performed using parental GK1.5 Ab as a control. The apparent affinities for both were similar (GK1.5 Ab $K_d = 1.1 \pm 0.06$ nM; GK1.5 cDb $K_d = 2.7 \pm 0.20$ nM; $n = 3$ independent experiments) (Figure 3.2).



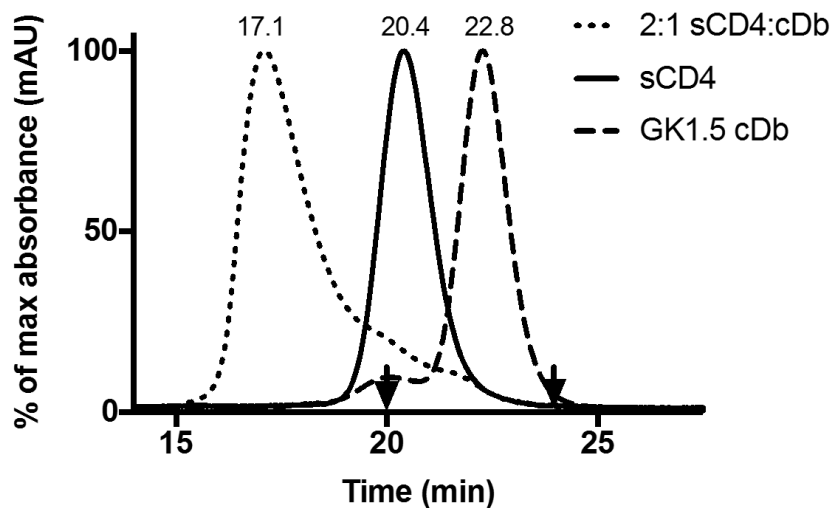


Figure 3.3 Conformation of GK1.5 cDb

Size exclusion chromatography of GK1.5 cDb (dashed line), soluble murine CD4 (solid line), and soluble murine CD4 in complex with GK1.5 cDb following incubation at a 2:1 molar ratio (dotted line), with elution times in minutes noted above peaks. Arrows indicate elution of markers albumin (66 kDa) at 20.0 minutes and carbonic anhydrase (29 kDa) at 24.0 minutes.

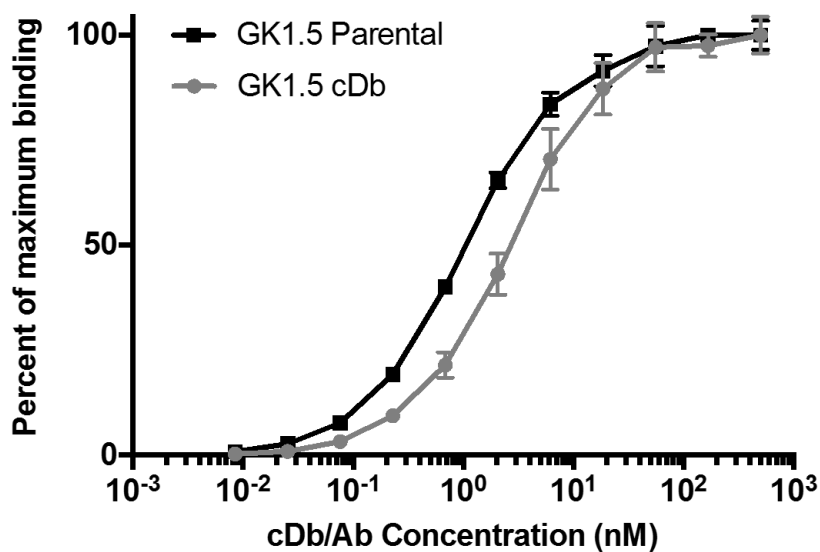
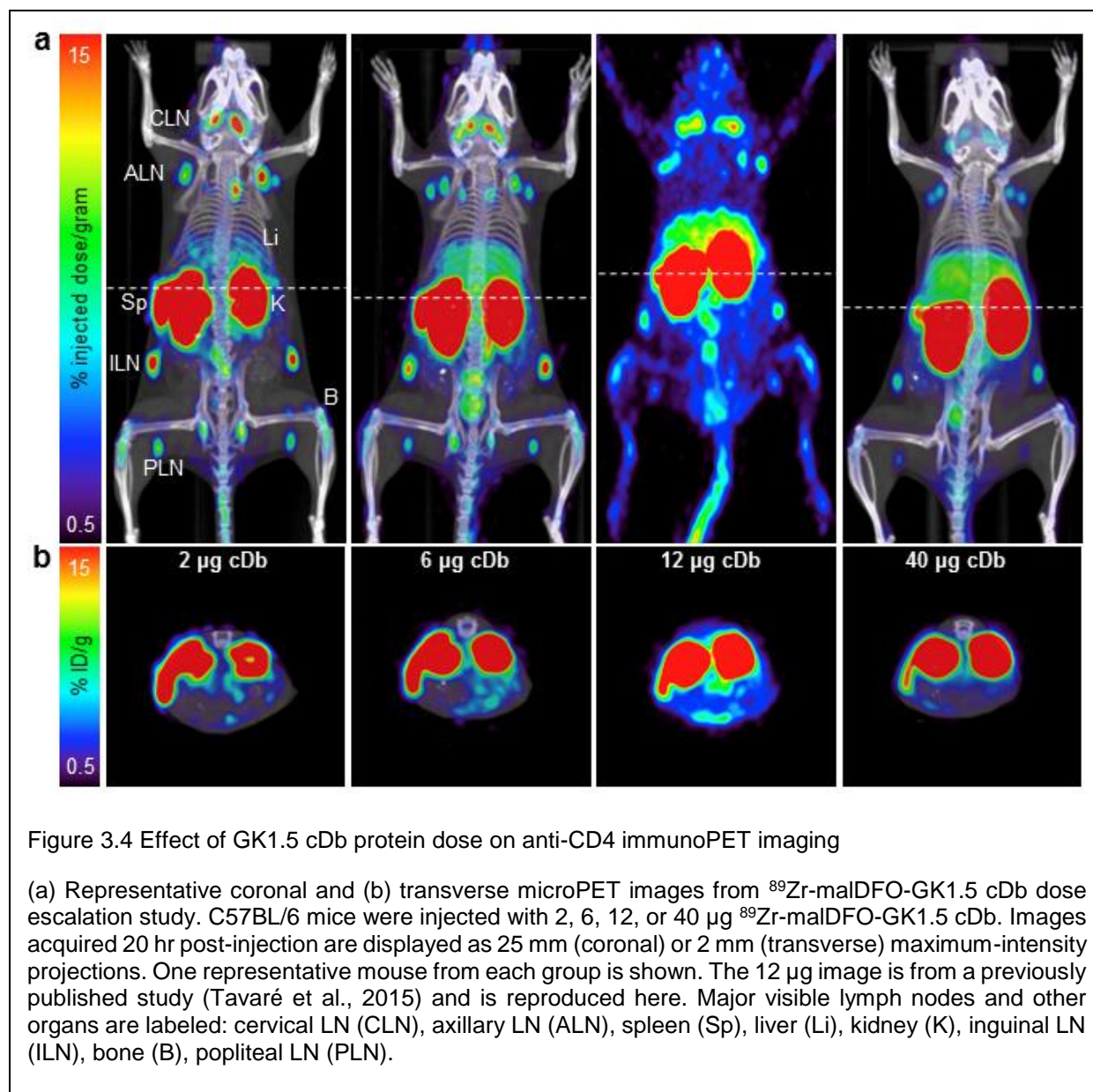


Figure 3.2 Affinity of GK1.5 cDb

Affinities of intact GK1.5 Ab and GK1.5 cDb were estimated with ELISA, using immobilized soluble CD4 antigen (n=3 independent experiments; results of one representative experiment shown).

3.3.2 ImmunoPET with low-dose ^{89}Zr -malDFO-GK1.5 cDb yields high-contrast images of lymphoid organs

MalDFO-GK1.5 cDb was successfully radiolabeled with Zr-89. Radiolabeling efficiency and radiochemical purity of ^{89}Zr -malDFO-GK1.5 cDb as determined by instant thin layer chromatography were both ~99%. Specific activity of ^{89}Zr -malDFO-GK1.5 cDb was 0.12 MBq/ μg . To determine the effect of protein dose on specific uptake by lymphoid organs, 2, 6, 12, or 40 μg (0.26-5.0 MBq) of ^{89}Zr -malDFO-GK1.5 cDb were injected intravenously into C57BL/6 mice (n=4 for 2, 6, and 40 μg protein doses; n=3 for 12 μg protein dose, previously published (Tavaré et al., 2015)). PET images at 20 h post-injection (p.i.) showed uptake of ^{89}Zr -malDFO-GK1.5 cDb in spleen and cervical, axillary, inguinal, and popliteal lymph nodes at all protein doses (Figure 3.4). Consistent with previously published studies (Tavaré et al., 2015), thymic uptake of ^{89}Zr -malDFO-GK1.5 cDb was not observed on microPET images; however, small regions of uptake are visible at the anterior end of the lung cavity and may represent parathymic lymph nodes which are normally associated with the thymus (Griessinger et al., 2014). Higher protein doses resulted in a blocking effect, as seen by reduced contrast of lymphoid organs in the 12 and 40 μg images (Figure 3.4).



Ex vivo biodistribution studies confirmed that uptake in lymph nodes and spleen was high. The %ID/g was significantly higher at the 2 μg dose compared to the previously published 12 μg dose (Tavaré et al., 2015) in ILN (2 μg : 106 ± 13 ; 12 μg : 45 ± 5.3 %ID/g; $p < 0.05$). Both the 2 μg and 6 μg doses resulted in significantly higher uptake in the spleen compared to the 12 μg dose (2 μg : 70 ± 1.4 ; 6 μg : 46 ± 5.0 ; 12 μg : 30 ± 3.4 %ID/g; $p < 0.05$) (Figure 3.5; Table 1). Uptake in lymphoid organs was not significantly different between

the 40 and 12 μg doses. Thymic uptake was not observed at any dose (Figure 3.5; Table 1). Lymphoid tissue:muscle ratios were also higher at lower protein doses (Figure 3.6). Non-specific background uptake was observed in organs of clearance, primarily the kidney as GK1.5 cDb is below the molecular weight threshold (~ 60 kDa) for renal clearance (Figure 3.5; Table 1).

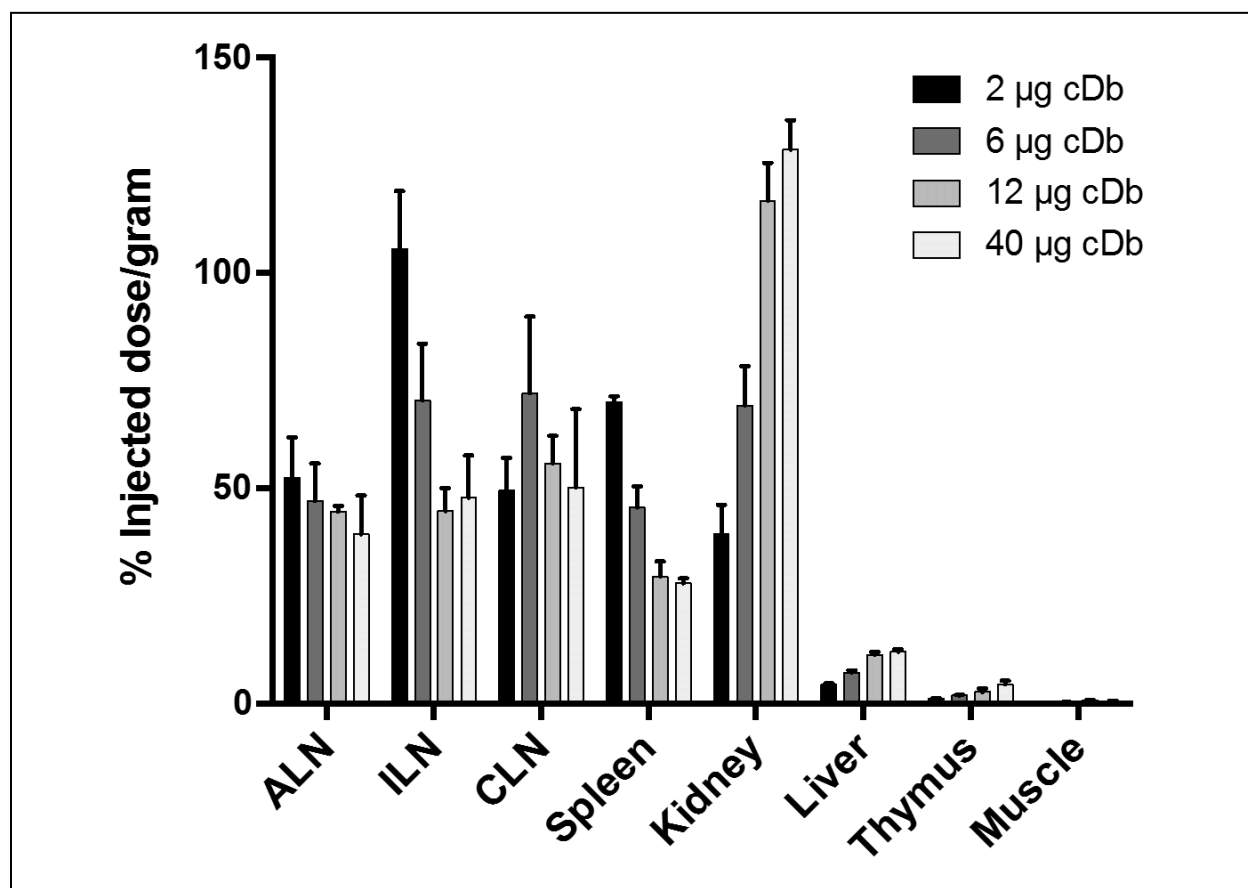


Figure 3.5 *Ex vivo* biodistribution from ^{89}Zr -malDFO-GK1.5 cDb dose escalation

Ex vivo biodistribution from ^{89}Zr -malDFO-GK1.5 cDb dose escalation immunoPET study. Following the PET scan 20 hr post-injection of probe, organs were removed, weighed, and counted to determine activity in each organ (expressed as % ID/g). Complete biodistribution data are provided in Table 1. Data for the 12 μg group are from a previously published study (Tavaré et al., 2015). (n=4 for 2, 6, and 40 μg protein doses; n=3 for 12 μg protein dose).

Table 1 Ex vivo biodistribution of ⁸⁹Zr-malDFO-GK1.5 cDb dose escalation immunoPET study

Organ	Percent injected dose per gram (%ID/g)			
	2µg GK1.5 cDb	6µg GK1.5 cDb	12µg GK1.5 cDb	40µg GK1.5 cDb
Blood	0.21 ± 0.03 *	0.29 ± 0.05	0.33 ± 0.01	0.36 ± 0.01 *
ALN	53 ± 9.3	47 ± 8.5	45 ± 1.4	39 ± 9.0
ILN	106 ± 13 *	70 ± 13	45 ± 5.3	48 ± 9.9
CLN	49 ± 7.6	72 ± 18	56 ± 6.4	50 ± 18
Spleen	70 ± 1.4 *	46 ± 5.0 *	30 ± 3.4	28 ± 1.1
Stomach	0.75 ± 0.31	1.44 ± 0.86	1.6 ± 0.49	1.1 ± 0.30
Intestines	2.4 ± 0.07	3.0 ± 0.30	3.1 ± 0.59	3.4 ± 0.31
Liver	4.4 ± 0.26 *	7.2 ± 0.47 *	11 ± 0.68	12 ± 0.6
Kidney	39 ± 6.7 **	69 ± 9.2 *	117 ± 8.7	129 ± 6.8
Thymus	1.1 ± 0.08	1.9 ± 0.21	2.7 ± 0.73	4.4 ± 0.83
Heart	0.56 ± 0.03 **	0.99 ± 0.17 *	1.8 ± 0.05	1.5 ± 0.12 *
Lung	1.02 ± 0.08 **	1.6 ± 0.22 *	2.4 ± 0.13	2.4 ± 0.28
Muscle	0.19 ± 0.02	0.36 ± 0.03	0.72 ± 0.15	0.58 ± 0.17
Bone	4.2 ± 1.1	4.1 ± 0.31	3.6 ± 0.37	4.1 ± 0.12
Carcass	0.59 ± 0.05 **	0.81 ± 0.08 **	1.3 ± 0.06	1.1 ± 0.09 *
Tail	5.2 ± 2.4	5.0 ± 1.1	7.9 ± 1.4	6.7 ± 0.76
Ratios				
<u>Spleen:Muscle</u>	341 ± 62	166 ± 48	91 ± 11	78 ± 3.8
<u>ALN:Muscle</u>	257 ± 65	168 ± 28	137 ± 6.3	110 ± 25
<u>ILN:Muscle</u>	539 ± 27	254 ± 64	138 ± 18	134 ± 31
<u>CLN:Muscle</u>	243 ± 71	252 ± 20	171 ± 23	141 ± 54

The 2, 6, and 40 µg groups (n=4 mice/group) were compared individually to the 12 µg group (n=3), data from which has been previously published (Tavaré et al., 2015). Values are represented as mean ± standard deviation. * p<0.05, ** p<0.005, *** p<0.0005. Abbreviations: axillary LN (ALN), inguinal LN (ILN), cervical LN (CLN).

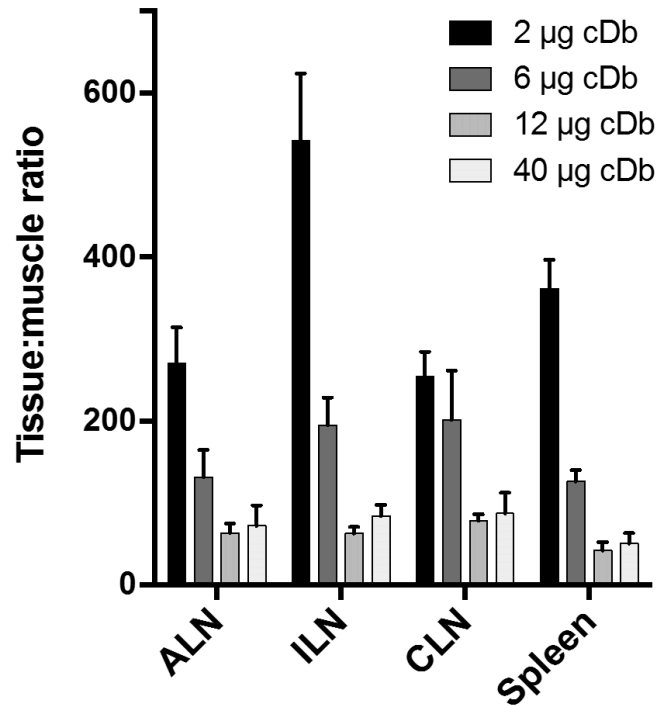


Figure 3.6 Target:muscle ratios from ^{89}Zr -malDFO-GK1.5 cDb dose escalation study

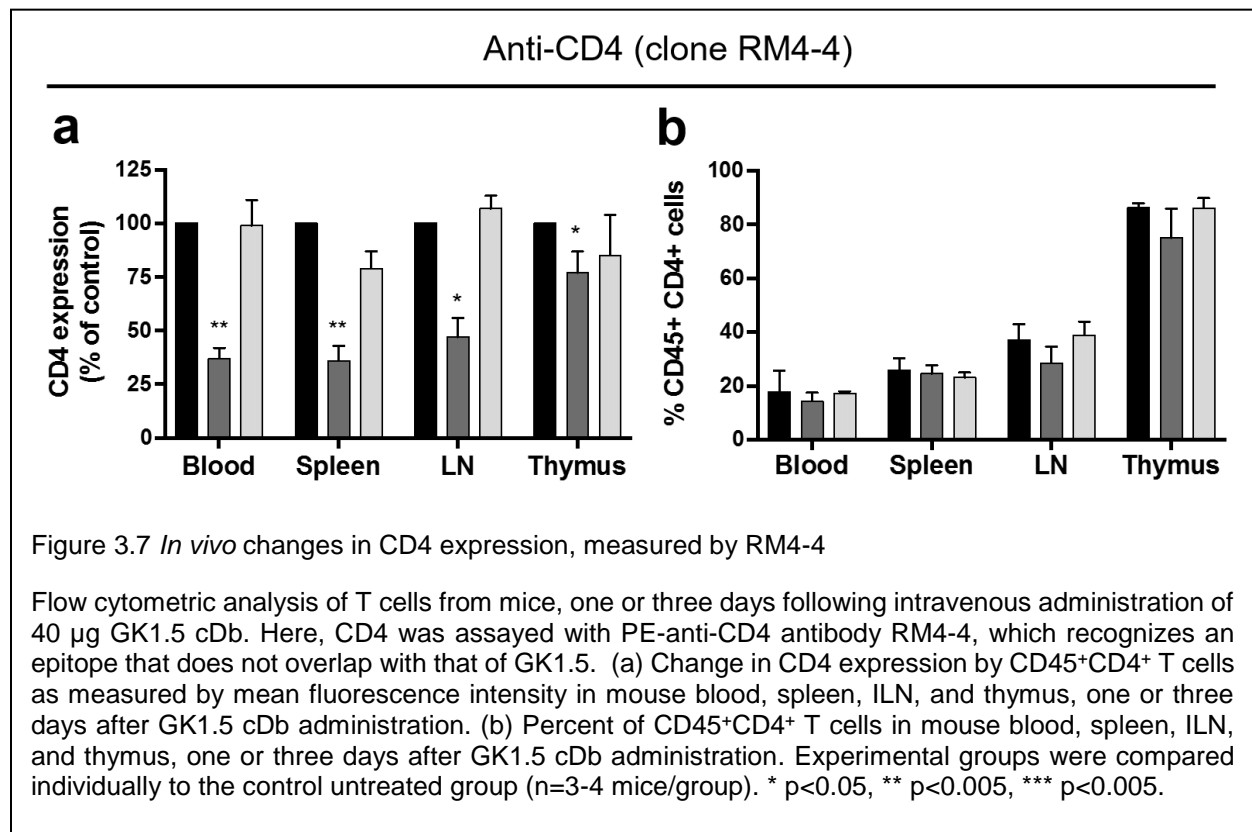
Target:muscle ratios from ^{89}Zr -malDFO-GK1.5 cDb dose escalation immunoPET study. Tissue:muscle ratios for secondary lymphoid organs including spleen and axillary, inguinal, and cervical lymph nodes from biodistribution data. Data for the 12 µg group are from a previously published study (Tavaré et al., 2015). (n=4 for 2, 6, and 40 µg protein doses; n=3 for 12 µg protein dose).

3.3.3 GK1.5 cDb causes transient decrease in CD4 expression *in vivo*

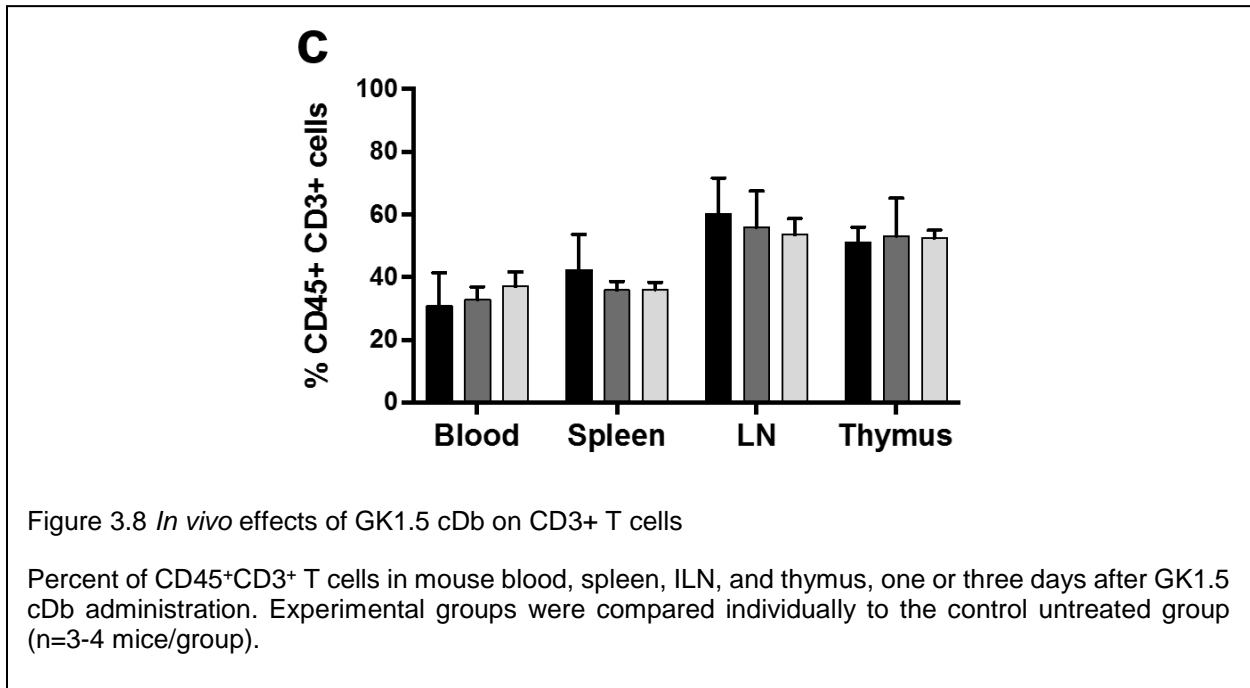
To investigate effects of GK1.5 cDb on the expression of CD4 by CD4⁺ T cells, we injected 40 µg GK1.5 cDb into C57BL/6 mice and measured surface CD4 expression by T cells in blood, spleen, ILN, and thymus after one or three days. Due to the possibility that GK1.5 cDb could induce downmodulation of CD4, or block staining by fluorescently labeled GK1.5 antibody, flow studies on CD4 expression were performed using both GK1.5 and RM4-4 anti-CD4 antibodies, which have distinct, non-overlapping epitopes on extracellular CD4 (Vignali and Vignali, 1999). CD4 expression (measured with RM4-4) was significantly decreased one day p.i. in mice treated with GK1.5 cDb compared to

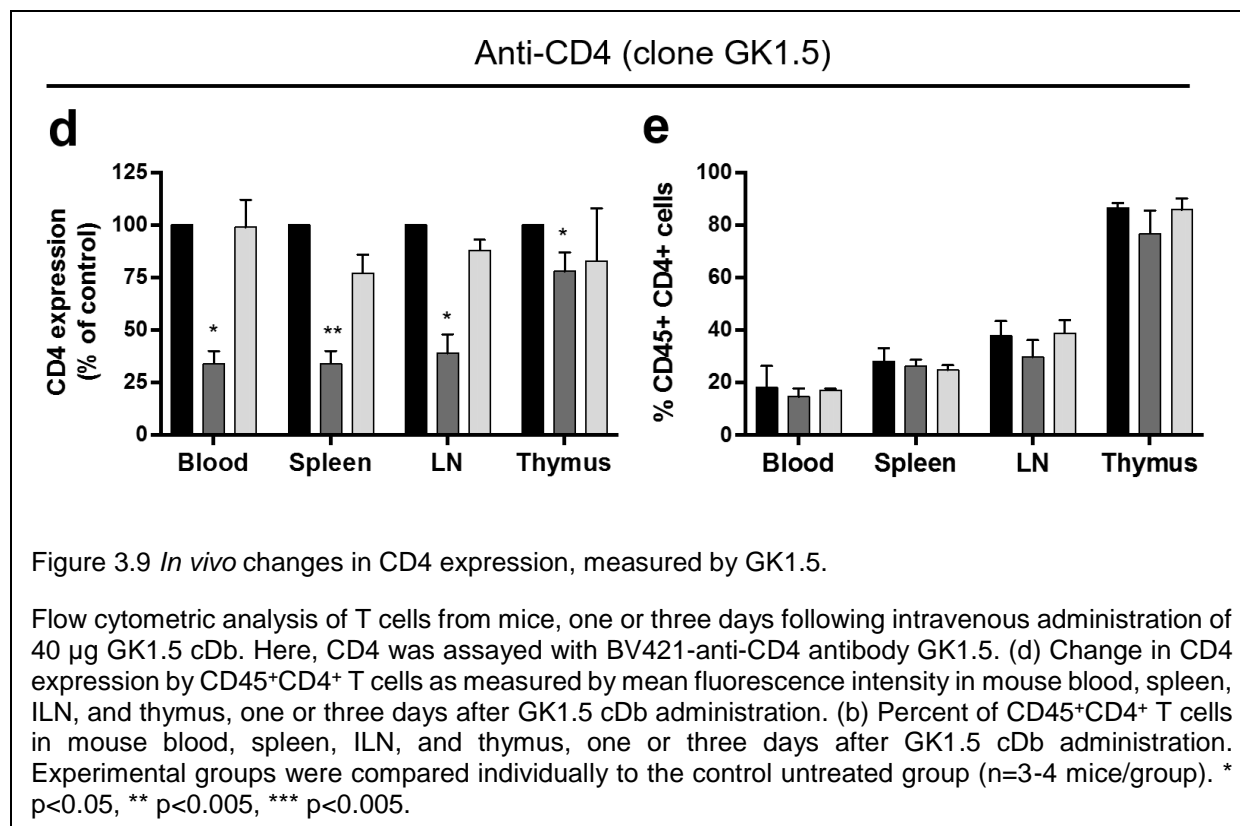
control untreated mice by $63 \pm 5\%$ (blood; $p < 0.005$), $64 \pm 7\%$ (spleen; $p < 0.005$), $53 \pm 9\%$ (ILN; $p < 0.05$), and $33 \pm 10\%$ (thymus; $p < 0.05$) (Figure 3.7a).

Three days later, CD4 expression on T cells had recovered in blood, LN, and thymus. Splenic CD4⁺ T cells showed a slower recovery on day 3 ($21 \pm 8\%$ decrease in MFI), but the difference was not statistically significant. Despite the decrease in expression as measured by mean fluorescence intensity, there were no significant changes in the percentages of CD45⁺CD4⁺ (Figure 3.7b) or total CD3⁺ T cells (Figure 3.8), showing that CD4⁺ T cells were not depleted by administration of GK1.5 cDb. Staining with GK1.5 Ab confirmed the results of staining with RM4-4, indicating that the epitopes for both antibodies were accessible (Figure 3.9). The lesser extent of decreased CD4 expression by T cells in the thymus suggests that GK1.5 cDb is less able to interact



with CD4⁺ T cells in the thymus compared to other lymphoid organs. This parallels the results of imaging and biodistribution studies, which showed no specific uptake of ⁸⁹Zr-malDFO-GK1.5 cDb in the thymus (Figure 3.4, Figure 3.5, Table 1) (Tavaré et al., 2015).





3.3.4 GK1.5 cDb alters CD4⁺ T cell proliferation and cytokine release in a dose-dependent manner *in vitro*

GK1.5 cDb could potentially affect antigen-specific CD4⁺ T cell proliferation because it binds to an epitope on Domain 1 of CD4 (Dianzani et al., 1992) which interacts with the beta2-domain of MHC II on antigen presenting cells (Wang et al., 2001). To evaluate this effect *in vitro*, OT-II CD4⁺ T cells (which recognize peptides 329-339 of OVA presented by MHC II) were cultured with OVA-pulsed splenocytes and serial concentrations of GK1.5 cDb. At 25 nM and above, GK1.5 cDb significantly inhibited the percentage of OT-II CD4⁺ T cells able to initiate cell division (Figure 3.10a). These concentrations also inhibited cells that were able to initiate division from continuing to proliferate (Figure 3.10b). Lower concentrations of GK1.5 cDb did not show any inhibition

of proliferation; interestingly, the lowest concentration (0.097 nM) seemed to stimulate proliferation, although this effect was not significant ($p=0.064$).

An additional readout of T cell activation is cytokine production. Changes in interferon- γ (IFN γ) production by cells *in vitro* paralleled the dose-dependent GK1.5 cDb-induced inhibition of proliferation. The concentration of IFN γ was significantly decreased at 25 nM and 100 nM GK1.5 cDb (Figure 3.11). Levels of other cytokines were also assayed, but no consistent trends were seen (data not shown).

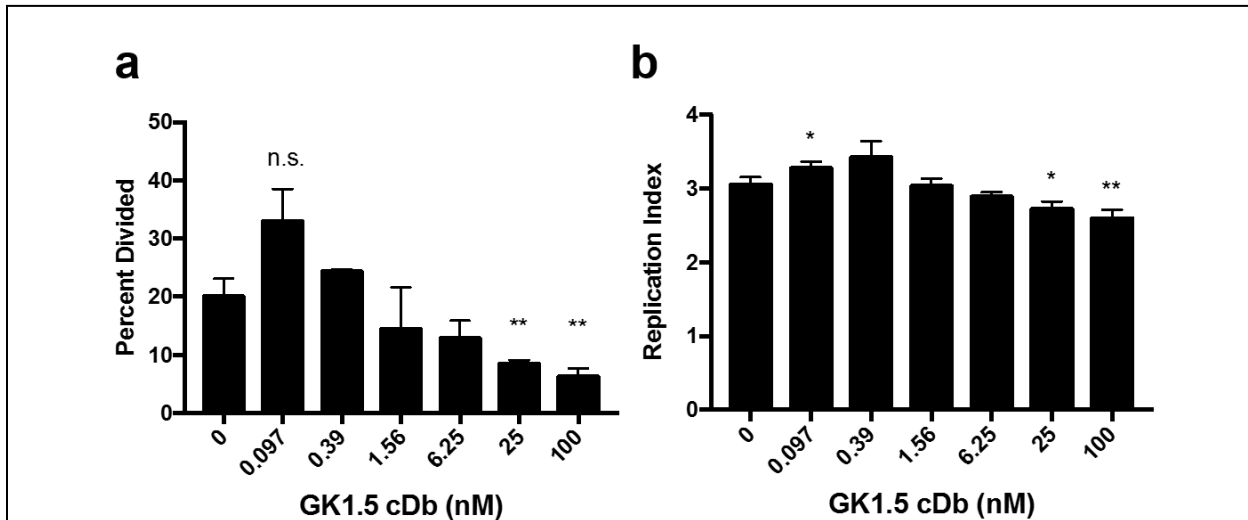


Figure 3.10 *In vitro* effects of GK1.5 cDb on T cell proliferation.

CFSE-labeled OT-II CD4⁺ T cells were cultured with OVA-pulsed splenocytes and incubated with various concentrations of GK1.5 cDb. (a) Proliferation was analyzed with flow cytometry 72 hours after addition of GK1.5 cDb, and percent divided was calculated by determining the percent of CFSE-labeled cells that divided at least once. (b) Replication index was determined by the fold-expansion of proliferative OT-II cells ($n = 3$ independent experiments). All concentrations of GK1.5 cDb were compared to control well. n.s.: not significant, * $p < 0.05$, ** $p < 0.005$.

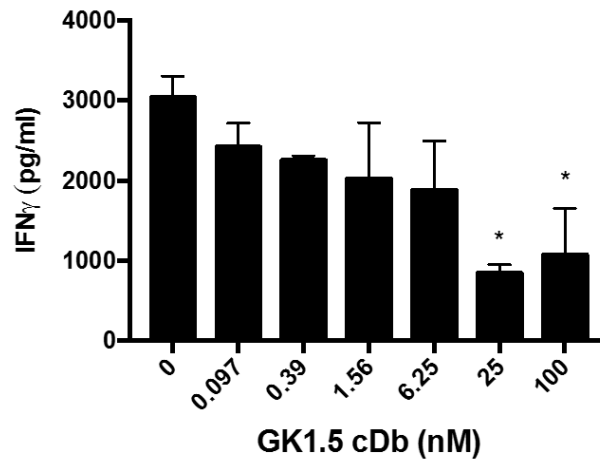


Figure 3.11 *In vitro* effects of GK1.5 cDb on T cell IFN γ production

CFSE-labeled OT-II CD4⁺ T cells were cultured with OVA-pulsed splenocytes and incubated with various concentrations of GK1.5 cDb. Culture supernatant was collected at 72 hours and concentration of IFN γ was assayed (n = 2 independent experiments). All concentrations of GK1.5 cDb were compared to control well. n.s.: not significant, * p<0.05, ** p<0.005.

3.3.5 GK1.5 cDb decreases CD4 expression and inhibits CD4⁺ T cell proliferation in a dose-dependent manner *in vivo*

To determine the impact of protein dose on surface CD4 expression by T cells *in vivo*, GK1.5 cDb was administered to mice at the 2 and 40 μ g doses used in the imaging study. The 2 μ g dose of GK1.5 cDb resulted in decreased expression of surface CD4 one day p.i., but to a lesser extent than the 40 μ g dose (Figure 3.12). To expand on the *in vitro* proliferation studies, C57BL/6 mice were administered OT-II CD4⁺ T cells one day prior to the injection of OVA and the low or high dose of GK1.5 cDb. Effects of GK1.5 cDb on antigen-specific proliferation *in vivo* were organ- and dose-dependent. Proliferation of OT-II CD4⁺ T cells in spleen was not significantly inhibited after administration of either 2

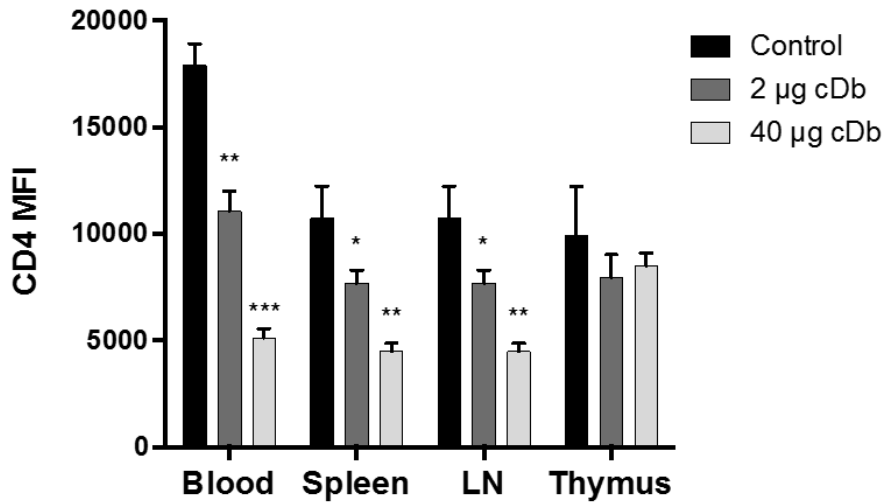


Figure 3.12 *In vivo* effects of GK1.5 cDb on CD4 expression

Change in surface CD4 expression by T cells from mice, one day following intravenous administration of 2 or 40 µg GK1.5 cDb (n=4 mice/group). Experimental groups were compared individually to control untreated group. (b) * p<0.05, ** p<0.005, *** p<0.0005, **** p<0.0001.

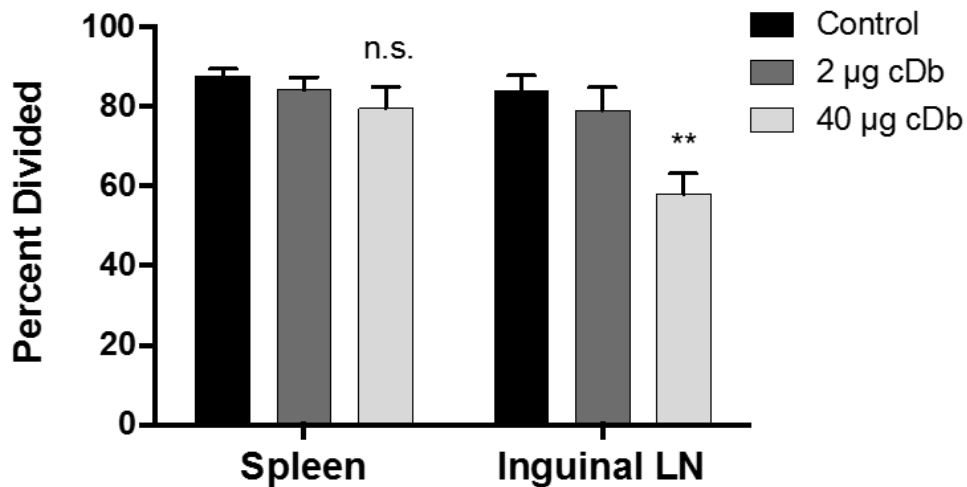


Figure 3.13 *In vivo* effects of GK1.5 cDb on CD4+ T cell proliferation

Percent OT-II cells divided in ILN and spleens of OVA-stimulated mice was assessed 72 hours after administration of GK1.5 cDb (n=3 mice/group). ** p<0.005. Experimental groups were compared individually to control (OVA + T cells only) group.

µg or 40 µg of GK1.5 cDb (Figure 3.13, Figure 3.14). OT-II CD4⁺ T cells isolated from the ILN showed significantly inhibited proliferation at 40 µg, but not at 2 µg, confirming that

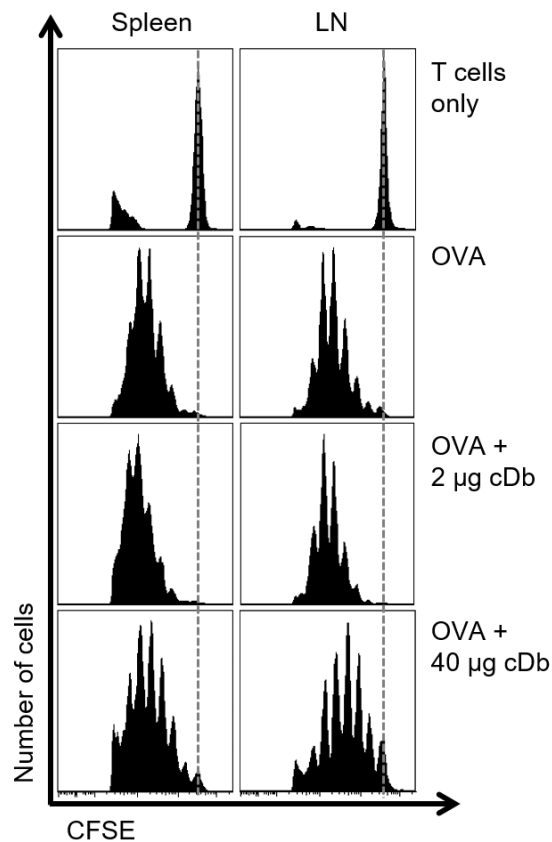


Figure 3.14 GK1.5 cDb administration affects proliferation *in vivo*

Representative CFSE histograms of OVA-stimulated OT-II CD4⁺ T cells from spleen and ILN 72 h after administration of GK1.5 cDb. Dashed line indicates undivided cells.

higher doses of GK1.5 cDb result in impaired CD4⁺ T cell antigen-driven division (Figure 3.13, Figure 3.14).

3.4 Discussion

The CD4 co-receptor is required for efficient activation of CD4⁺ T cells by antigen presenting cells, and modulation of co-receptor availability by an immunoPET imaging probe could affect the ability of cells to respond to antigen presentation. Investigation of the potential impact of GK1.5 cDb on CD4⁺ T cells is of particular importance because

the parental intact GK1.5 Ab has long been used for its CD4⁺ T cell depleting properties; furthermore, GK1.5 binds to the domain of CD4 that interacts with MHC II (Dianzani et al., 1992). Its ability to suppress the induction of antigen-specific CD4⁺ T cell proliferation and cytokine release has been documented (Wilde et al., 1983), and does not require the Fc region, as demonstrated by a study showing that the monovalent Fab fragment of GK1.5 inhibits induction of CD4⁺ T cell proliferation in response to antigen *in vitro* (Haque et al., 1987). In addition, a bivalent F(ab')₂ GK1.5 fragment inhibited humoral immunity in mice (Gutstein and Wofsy, 1986), indicating that fragments of GK1.5 can have potentially severe effects on not only CD4⁺ T cells but indirectly on other compartments of the immune system as well. Here, various protein doses relevant to those used for imaging were assessed to determine whether GK1.5 cDb modulated CD4⁺ T cell viability, surface CD4 expression, proliferation, or cytokine production.

Anti-CD4 immunoPET provides a method of noninvasively monitoring CD4⁺ T cells in a comprehensive manner, and can complement and expand on the information gained from blood samples and biopsies. *Ex vivo* biodistribution data collected from the dose-escalation imaging study showed that the 2 µg protein dose of ⁸⁹Zr-malDFO-GK1.5 cDb resulted in significantly higher %ID/g in spleen and ILN compared to protein doses of 12 or 40 µg (Figure 3.5, Table 1). These results are favorable, as the 2 µg protein dose resulted in a milder effect on decreased CD4 expression, and did not inhibit CD4⁺ T cell proliferation *in vivo*. Lack of specific ⁸⁹Zr-malDFO-GK1.5 uptake in the thymus was consistent at all protein doses. We considered that thymic uptake might be Fc-region dependent (Tavaré et al., 2015), since the parental intact GK1.5 Ab depletes CD4⁺ T cells in the thymus successfully; however, Rubin et al. imaged with intact GK1.5 and also saw

no specific thymic uptake (Rubin et al., 1996). Interestingly, thymic T cells showed a small, but significant, decrease in CD4 expression after *in vivo* administration of GK1.5 cDb, suggesting that a small amount of GK1.5 cDb is able to enter the thymus (Figure 3.7). Parathymic LN were likely isolated with the thymus and may have acted as a source of extrathymic CD4⁺ T cells, which could have affected the results of biodistribution analysis and CD4 expression studies. Delivery to, retention, and activity of anti-CD4 Abs and Ab fragments in the thymus warrants further investigation.

The effect of GK1.5 cDb on CD4 expression was dose-dependent, as mice that received 2 µg GK1.5 cDb retained higher surface CD4 expression on CD45⁺ cells from the spleen, blood, ILN, and thymus than mice that received the 40 µg dose (Figure 3.9). Although the decrease in expression was significant, CD4 was still detectable at both doses. The change in CD4 MFI was transient and expression levels recovered within three days post-injection (Figure 3.7, Figure 3.9). Although cell surface expression of CD4 was decreased, the percentages of total CD3⁺ T cells and CD45⁺CD4⁺ cells in the spleen, blood, ILN, and thymus were not altered after one or three days, indicating that GK1.5 cDb does not deplete CD4⁺ T cells *in vivo* (Figure 3.7, Figure 3.8). Reduced CD4 expression levels are assumed to be due to GK1.5 cDb-induced downmodulation of CD4.

In vivo administration of GK1.5 cDb demonstrated dose-dependent effects on the proliferation of adoptively transferred CFSE-labeled OT-II CD4⁺ T cells: 2 µg GK1.5 cDb did not significantly inhibit OVA-induced proliferation in the spleen or ILN, but 40 µg did inhibit proliferation in the ILN (Figure 3.13). *In vitro* functional assays demonstrated a similar result; only at concentrations of 25 nM and above were cell division and IFN γ release inhibited (Figure 3.10, Figure 3.11). However, the lowest dose of 0.097 nM

caused increased proliferation and presents an interesting possibility: GK1.5 cDb administered at very low doses could have an immune-stimulating effect. Furthermore, the decreased proliferation seen at higher doses both *in vitro* and *in vivo* suggests that GK1.5 cDb could be used at higher doses to suppress CD4⁺ T cell proliferation without depleting the cells. Additional studies would be required to determine the optimal dose for agonistic or antagonistic effects of GK1.5 cDb activity *in vivo*.

Alternative approaches to reduce probe biological activity include creating a monovalent antibody fragment to prevent crosslinking and internalization of the biomarker, or targeting an epitope that is less likely to be involved in critical interactions such as CD4-MHC II binding. Additionally, reduction of radiation dose is especially important when imaging CD4⁺ T cells as they are particularly radiosensitive (Gridley et al., 2009). Here, the sensitivity of PET imaging enabled levels of administered activity as low as 0.26 MBq. Radiation produced by the microCT is also of concern, as ionizing radiation can induce multiple effects in lymphoid populations including changes in gene and protein expression, stimulation or inhibition of proliferation, and apoptosis (Gridley et al., 2009; Rödel et al., 2012; Shankar et al., 1999). To limit exposure, the use of advanced microCT instruments which require lower radiation doses would be beneficial.

While this work demonstrates the utility of anti-CD4 cDb in imaging CD4⁺ T cells throughout an organism, one disadvantage is that subsets of CD4⁺ T cells and other CD4-expressing cells such as dendritic cells cannot be distinguished using a single anti-CD4 probe. Therefore, GK1.5 cDb is limited in its ability to identify, for example, whether signal is due to a pro-inflammatory Th1 cell, an inflammation-suppressing Treg cell, or any other CD4⁺ cell. More specific biomarkers would need to be assessed either alone or in tandem

with GK1.5 cDb in order to localize and quantify certain CD4⁺ cell populations. Although GK1.5 cDb alone cannot provide information about the various subsets present, its use in imaging total CD4⁺ T cells is still highly valuable; anti-CD4 immunoPET gives spatial and quantifiable data about CD4⁺ T cells throughout the entire body in contrast to blood samples and biopsies, which sample a limited proportion of total CD4⁺ T cells. GK1.5 cDb can be used to investigate CD4⁺ T cells in mouse models of disease and to test treatment efficacy rapidly and noninvasively. The ability to image and quantify total CD4⁺ T cells has implications for monitoring diseases including HIV infection (Byrareddy et al., 2016; Di Mascio et al., 2009), colitis (Kanwar et al., 2008), and rheumatoid arthritis (Becker et al., 1990; Steinhoff et al., 2014). Recent interest in the potential of CD4⁺ T cells for tumor immunotherapy also suggests a role for careful monitoring of CD4⁺ T cells in the context of anti-tumor immunity (Zanetti, 2015). Further studies may include use of this probe to study cell trafficking throughout the immune system and recruitment of CD4⁺ T cells to sites of inflammation.

3.5 Conclusions

Low dose GK1.5 cDb yields high-contrast immunoPET images with minimal biological effects on CD4⁺ T cells, and is a promising agent for noninvasive, whole-body investigation of CD4⁺ T cells in mice. When developing new imaging probes, dose may therefore be a key condition for optimization in order to image a target without perturbing the biomarker of interest or the cells by which it is expressed.

4 ImmunoPET imaging of CD4⁺ T cells in mesenteric lymph nodes and colons of colitic mice

4.1 Introduction

The gut is a crucial compartment of the immune system. Lymphocytes reside in multiple locations throughout the gut including the intestine, gut-associated lymphoid tissue such as Peyer's patches and lymphoid follicles, and mesenteric lymph nodes (Brandtzaeg et al., 2008). The immune system must balance the maintenance of tolerance to the many food- and microbiome-derived antigens sampled from the gut and mounting an immune response to pathogens. Dysregulation of this delicate balance can lead to inflammatory bowel disease (IBD), a family of disorders characterized in part by abnormal and excessive T cell responses (Geremia et al., 2014).

CD4⁺ T cells are known mediators of inflammation in IBD. Crohn's disease and ulcerative colitis each involve different subsets of CD4⁺ T cells, including Th1, Th2, and Th17 (Geremia et al., 2014). Numerous mouse models of IBD have helped to advance understanding of how certain immune cell subsets, including CD4⁺ T cells, contribute to gut inflammation. Several murine models, such as the CD4⁺CD45RB^{hi} T cell transfer model and the TNBS/oxalozone model, are CD4⁺ T cell-dependent and are often used to study contributions of the adaptive immune system to IBD (Wirtz and Neurath, 2007). The dextran sulfate sodium (DSS) model of colitis is often used to study innate immune cell contributions, as it is characterized by an initial influx of neutrophils, followed by later infiltration of T cells. While CD4⁺ T cells are not required for the induction of DSS colitis

(Axelsson et al., 1996; Dieleman et al., 1994), they do increase in number in the large intestine as the disease progresses (Hall et al., 2011). Hall et al. found that following 3% DSS administration for six days, the peak number of CD4+ T cells occurred on day 12 (d 12) after initiation of DSS administration. In addition, changes in the percent of T cells in spleen and MLN can occur as early as d 1 (Hall et al., 2011), indicating that even during the acute phase of colitis, the adaptive immune system is already changing, even though T cells are not required for induction. Thus, continued investigation into the role of CD4+ T cells in the DSS colitis model is warranted.

IBD presents a challenge for disease monitoring in both humans and animals; the gut is convoluted and foci of inflammation can occur at multiple sites, requiring numerous points of sampling to get a representative picture of disease. The current standard diagnostic method, endoscopy, is intrusive and uncomfortable for patients. Molecular imaging, which enables visualization of a target biomarker or biological process throughout the entire body, could aid by providing a noninvasive method of investigating multiple foci of inflammation. Furthermore, biomarker-specific probes can give insight into the subsets of cells involved in inflammation, which can inform decisions regarding treatment, and makes imaging a valuable tool for investigating how various immune cells such as CD4+ T cells may contribute to animal models of IBD.

We previously described GK1.5 cys-diabody (cDb), an anti-mouse CD4 antibody fragment, and demonstrated its use in tracking immune system reconstitution post-hematopoietic stem cell transplant (Tavaré et al., 2015). Subsequent studies investigated the effect of protein dose on image contrast and biological effect on CD4+ T cells, and showed that low-dose GK1.5 cDb produces high-contrast images of lymphoid organs with

minimal effects on CD4+ T cell function *in vivo* (Freise et al., in press). Here, the utility of GK1.5 cDb as a probe for regions of inflammation in the mouse DSS model of IBD has been evaluated. Anti-CD4 immunoPET, *ex vivo* biodistribution analysis, flow cytometry, and immunohistochemistry (IHC) were used to assess CD4+ T cells in the intestines and lymphoid organs of mice with DSS-induced colitis.

4.2 Materials and Methods

4.2.1 Animals

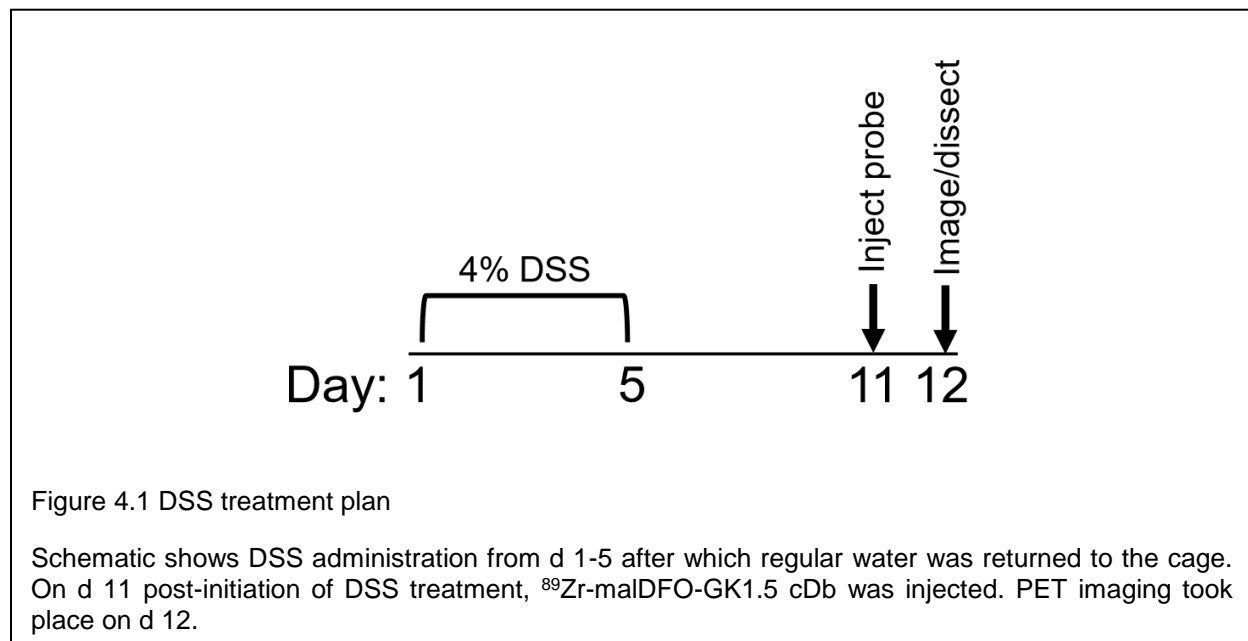
Female C57BL/6 mice between 6-12 weeks of age were obtained from Jackson Laboratories and housed by the Department of Laboratory Animal Medicine at the University of California, Los Angeles (UCLA) under specific pathogen-free conditions. Animal studies were conducted under protocols approved by the Chancellor's Animal Research Committee at UCLA.

4.2.2 Induction and assessment of colitis

DSS (40,000 kDa, Sigma) was dissolved in autoclaved tap water, sterile filtered, and provided *ad libitum*. Based on previously published literature (Hall et al., 2011) and our own dose-finding pilot studies (data not shown), we determined that 4% DSS administered for five days (d 1-5) would induce infiltration of mononuclear immune cells into the colon by d 12 post-induction (data not shown). Therefore, mice were treated with 4% DSS on d 1-5, followed by regular drinking water for seven days until d 12 (Figure

4.1). DSS intake per cage (four mice/cage) was monitored by weighing water bottles. Mice were weighed every day and examined for signs of colitis, evaluated by a disease activity index (DAI) modified from Sha *et al.* (Sha *et al.*, 2013): Weight loss (0: none, 1: 1–4%, 2: 5–10%, 3: 11-20% 4: >20%), fecal blood (0: none, 2: blood present in stool/hemocult positive, 4: gross bleeding from anus), and stool consistency (0: normal, 2: loose stools, 4: diarrhea/stool sticking to fur).

On d 12, mice were euthanized and the colon, cecum, and mesenteric lymph nodes were removed. After measuring the length of the colon, it was excised from the cecum, and feces were gently pushed out from both organs with the blunt end of scissors. MLN were pooled per individual mouse, weighed, and divided by the number of MLN collected to get the average weight of one MLN for each mouse.



For analysis of MLN cellularity, two MLN were mashed gently through a 70 µm nylon filter, rinsed with 2.5mL PBS/2% FBS, and the number of viable cells was determined using a Vi-Cell XR automatic cell counter (Beckman Coulter).

4.2.3 Histopathological evaluation of inflammation and CD4+ T cell infiltration

Colons and ceca were cut open longitudinally and wrapped, lumen facing outward, around a wooden dowel to create a Swiss roll (Moolenbeek and Ruitenbergh, 1981). Rolls were placed in 10% phosphate-buffered formalin overnight and transferred to 70% ethanol, followed by paraffin embedding, sectioning, and staining with hematoxylin & eosin or anti-CD4 antibody for IHC.

A veterinary pathologist examined sections of hematoxylin and eosin-stained colonic Swiss rolls for histologic damage. Three parameters (surface epithelial loss, crypt destruction, and inflammatory cell infiltration into mucosa) were evaluated according to a system adapted from Nishiyama (Nishiyama et al., 2012): 0: normal, 1: localized and mild, 2: localized and moderate, 3: localized and severe, 4: extensive and moderate. The scores for each parameter per colon were added. Lymphoid aggregates (including normal gut-associated lymphoid tissues and tertiary lymphoid structures) in each section were also counted.

For anti-CD4 IHC staining, slides were deparaffinized in xylene and a series of ethanol baths. Slides were incubated in 3% hydrogen peroxide and methanol for 10 minutes, washed with distilled water, and then incubated in citrate buffer (pH 6) for 25 minutes at 95°C. After returning to room temperature, slides were washed with PBS-Tween (0.05% Tween-20) and incubated with rabbit monoclonal anti-mouse CD4 antibody (Abcam, ab183685) at a 1:200 dilution for 1 hour at room temperature. Slides were rinsed, incubated with Dako EnVision+ System –HRP Labelled Polymer Anti-Rabbit

(Dako, K4003) for 30 min at room temperature, rinsed again, and incubated with 3,3'-diaminobenzidine to visualize CD4. Slides were then washed in tap water, stained with Harris' Hematoxylin, dehydrated in ethanol, and mounted with media.

IHC slides were scanned on an Aperio ScanScope AT (Leica) and analyzed using Tissue Studio image analysis software (Definiens). Two complete 4 μ m sections of colon or cecum Swiss roll, separated by 100 μ m, were analyzed per mouse. Regions of interest were drawn automatically around whole tissue sections by the software and manually confirmed for accuracy. The software was trained using a set of 12 sample images to designate the threshold for positive CD4 HRP staining and for hematoxylin staining of nuclei. After training was complete, the total number of cells and number of cells positive for CD4 were counted for each sample, and the percent of CD4+ cells in each sample was calculated.

4.2.4 Flow cytometry

Lymphocyte populations in mesenteric lymph nodes and spleens were analyzed by flow cytometry. Organ harvesting, processing, and preparation for flow cytometric analysis was performed as described in Chapter 3.

4.2.5 PET/CT Imaging

Anti-mouse CD4 GK1.5 cDb, a covalent dimer of two single-chain antibody variable fragments, was produced and purified as described previously (Freise et al., in press; Tavaré et al., 2015). GK1.5 cDb reduction, conjugation, and radiolabeling are described in detail in Chapter 2.

^{89}Zr -malDFO-GK1.5 cDb was administered (2 μg ; 0.38 MBq) intravenously and PET and CT scans were acquired 20 h post-injection. One hour before imaging, 100 μL Gastrografin (diatrizoate meglumine and diatrizoate sodium solution; Bracco) was administered via oral gavage for CT contrast of the upper gastrointestinal tract. Immediately prior to imaging, mice were anesthetized with 2% isoflurane and 100 μL Gastrografin was administered via intrarectal instillation for large intestine contrast. PET scans were acquired on an Inveon microPET scanner (Siemens) for 600 s. CT scans were acquired on the CrumpCAT, a fast microCT prototype developed at our institution (Taschereau et al., 2014). The CrumpCAT uses a 50 kVp, 200 μA x-ray source, and 720 frames were acquired over 360° with an exposure time of 100 ms per frame. After the *in vivo* PET/CT scan, mice were euthanized and colons, ceca, and MLN were removed. Feces was removed from the intact colon, and *ex vivo* PET/CT scans were acquired using the same parameters as above. All organs were weighed and gamma counted for *ex vivo* biodistribution analysis, and the decay-corrected % injected dose/gram (%ID/g) and %ID/organ for each tissue were calculated. In addition, colons and ceca were fixed and processed as above for histopathological and IHC analysis of tissue sections.

PET/CT images were viewed using A Medical Imaging Data Examiner (AMIDE) software (<http://amide.sourceforge.net>). Whole-body images are displayed as 25 mm maximum intensity projections (MIP). *Ex vivo* scans are displayed as 12 mm MIPs.

4.2.6 Image reconstruction and analysis

PET images were reconstructed with a 3D-ordered subset expectation maximization (OSEM) algorithm with 2 iterations, followed by maximum *a posteriori*

(MAP) with 18 iterations (beta=0.1) with a zoom factor of 2.1, with no attenuation correction. For quantitative analysis of uptake in the intestines, first the skeleton was manually removed from the CT image with the use of several regions of interest (ROI), and then a 3D isocontour ROI around the contrast-enhanced small and large intestines was created by choosing a point in the colon and setting a minimum value for CT intensity. ROIs were quantified in AMIDE.

4.2.7 Statistical analysis

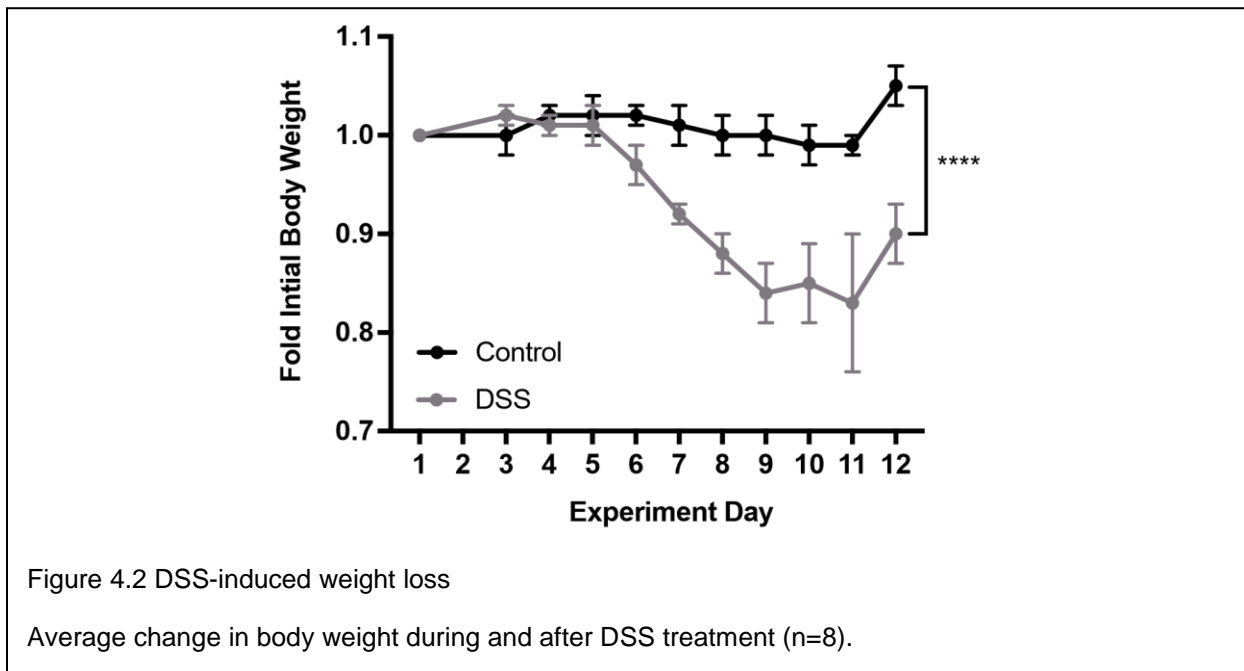
Statistical analyses were performed using a two-tailed Student's T test. A p-value of less than 0.05 was considered to be statistically significant. For T tests on organs from the *ex vivo* biodistribution study, the Holm-Sidak correction for multiple comparisons was applied. Prism software (GraphPad) was used to analyze data, perform statistical analysis, and create histograms. Values are reported as mean \pm standard deviation unless indicated otherwise. * $p < 0.05$, ** $p < 0.005$, *** $p < 0.0005$, **** $p < 0.0001$.

4.3 Results

4.3.1 DSS-induced colitis results in gross anatomical changes

Mice treated with 4% DSS for 5 days (Figure 4.1) showed signs of colitis. Weight loss began on d 6 and continued until approximately d 9. On d 12, the body weight of DSS-treated mice was reduced to 87 ± 0.06 % of their initial weight ($p < 0.0001$; $n = 8$) (Figure 4.2). DSS-treated mice also had significantly higher scores on the DAI compared to control mice as a result of increased weight loss, loose stool, and fecal bleeding (Figure 4.3).

Colons from DSS-treated mice (6.0 ± 0.7 cm) were significantly shorter than control colons (6.9 ± 0.9 cm; $p < 0.05$; $n = 8$) (Figure 4.4) The colon weight:length ratio was higher



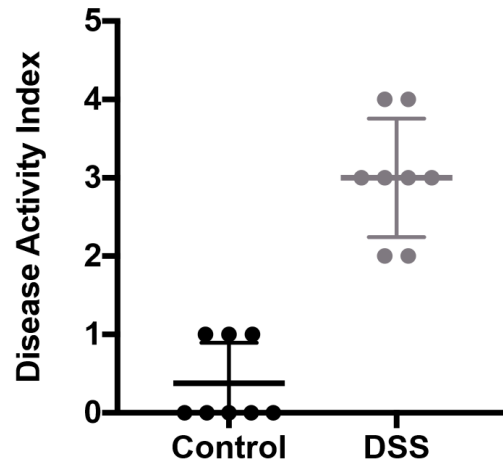


Figure 4.3 Disease activity index scores of colitic mice

Clinical signs were quantified using the disease activity index (DAI), which scored symptoms including weight loss, stool consistency, and fecal bleeding, at the time of sacrifice (n=8).

in colitic mice (Figure 4.4). Individual MLN from DSS-treated mice weighed more on average (6.1 ± 3.0 mg; range: 1.4-11) compared to MLN from control mice (2.1 ± 1.1 mg; range: 0.4-4.4; $p < 0.0001$; n=8 mice) (Figure 4.5, Figure 4.6); furthermore, MLN cellularity was higher on average in DSS mice (Figure 4.6).

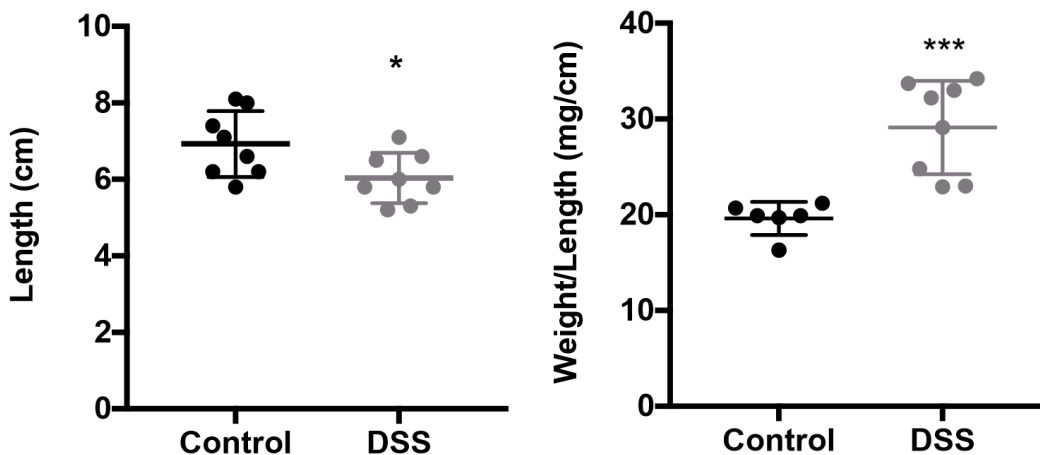


Figure 4.4 DSS induces gross anatomical changes in the colon

Colons were cut just below the cecum, laid flat next to a ruler, and measured. The ratio of colon weight to length was determined after removing stool from the colon (n=8). * $p < 0.05$, *** $p < 0.0005$.

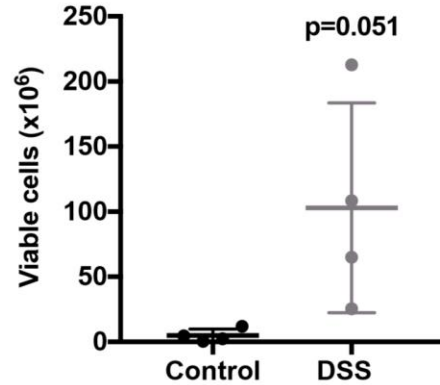
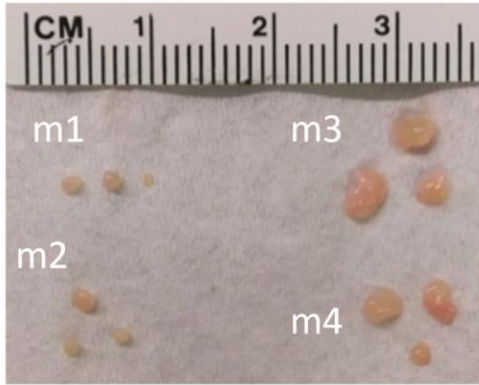


Figure 4.5 DSS-induced changes in MLN size and cellularity

Image shows three representative MLN from two control mice (left) and two DSS-treated mice (right). For the plot showing the average cellularity of MLN each point represents a value from a single control or DSS-treated mice (n=4 mice).

Histopathological signs of colitis were also present at the cellular level. Colons from DSS-treated mice had higher histopathological damage scores, based on the presence of epithelial loss, crypt destruction, and infiltration of inflammatory cells into the mucosa (Figure 4.6). These signs were severe but localized in most mice. DSS-treated mice also had significantly more lymphoid aggregates throughout the colon (Figure 4.6).

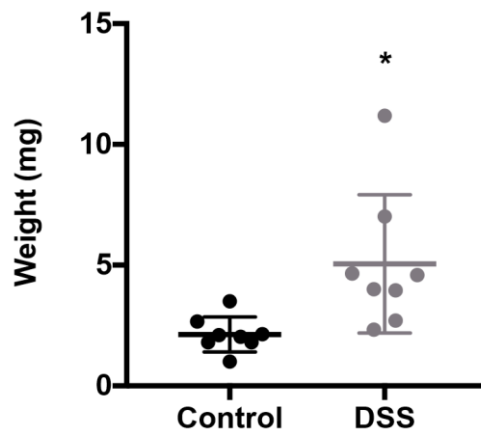
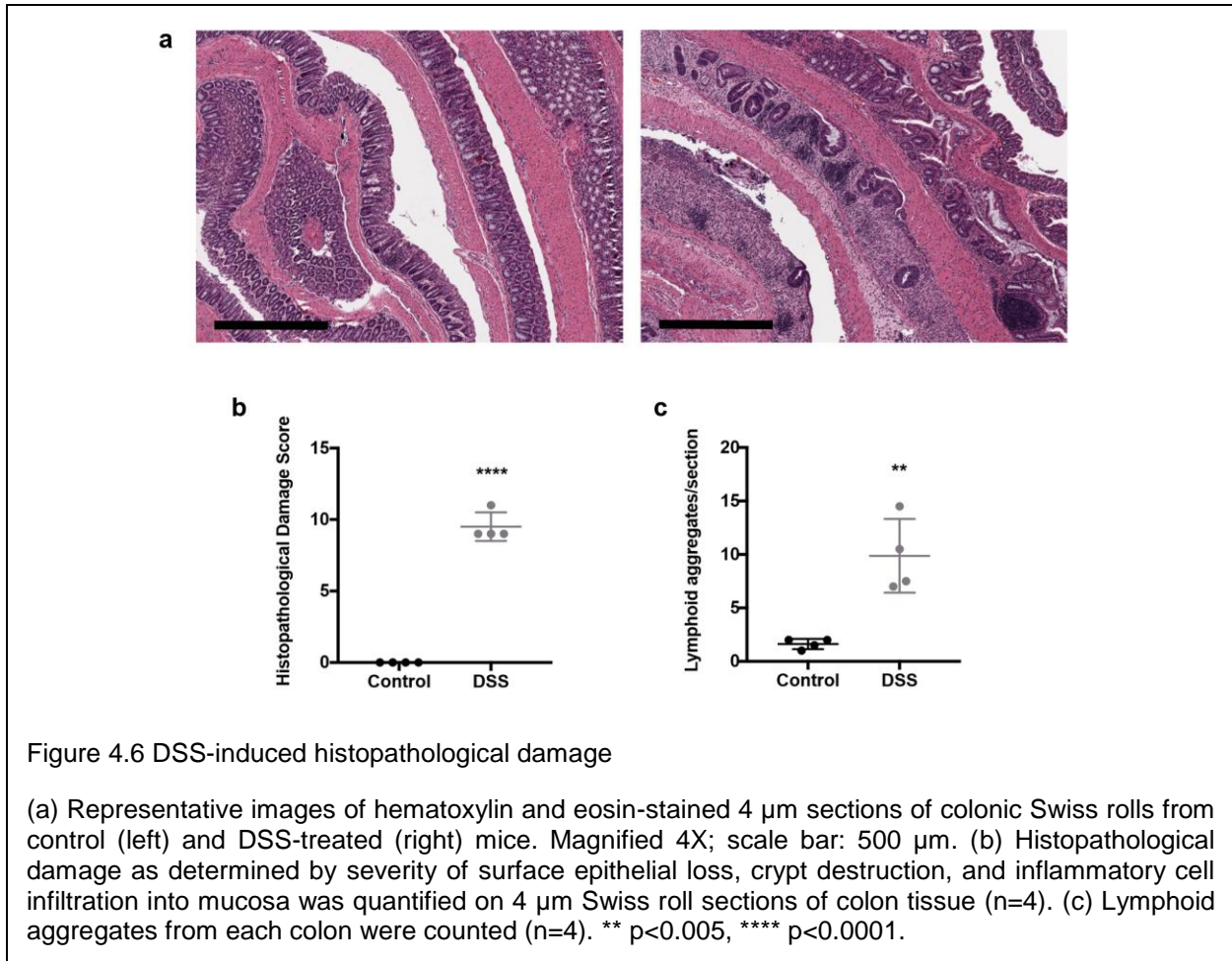


Figure 4.6 DSS increases average MLN weight.

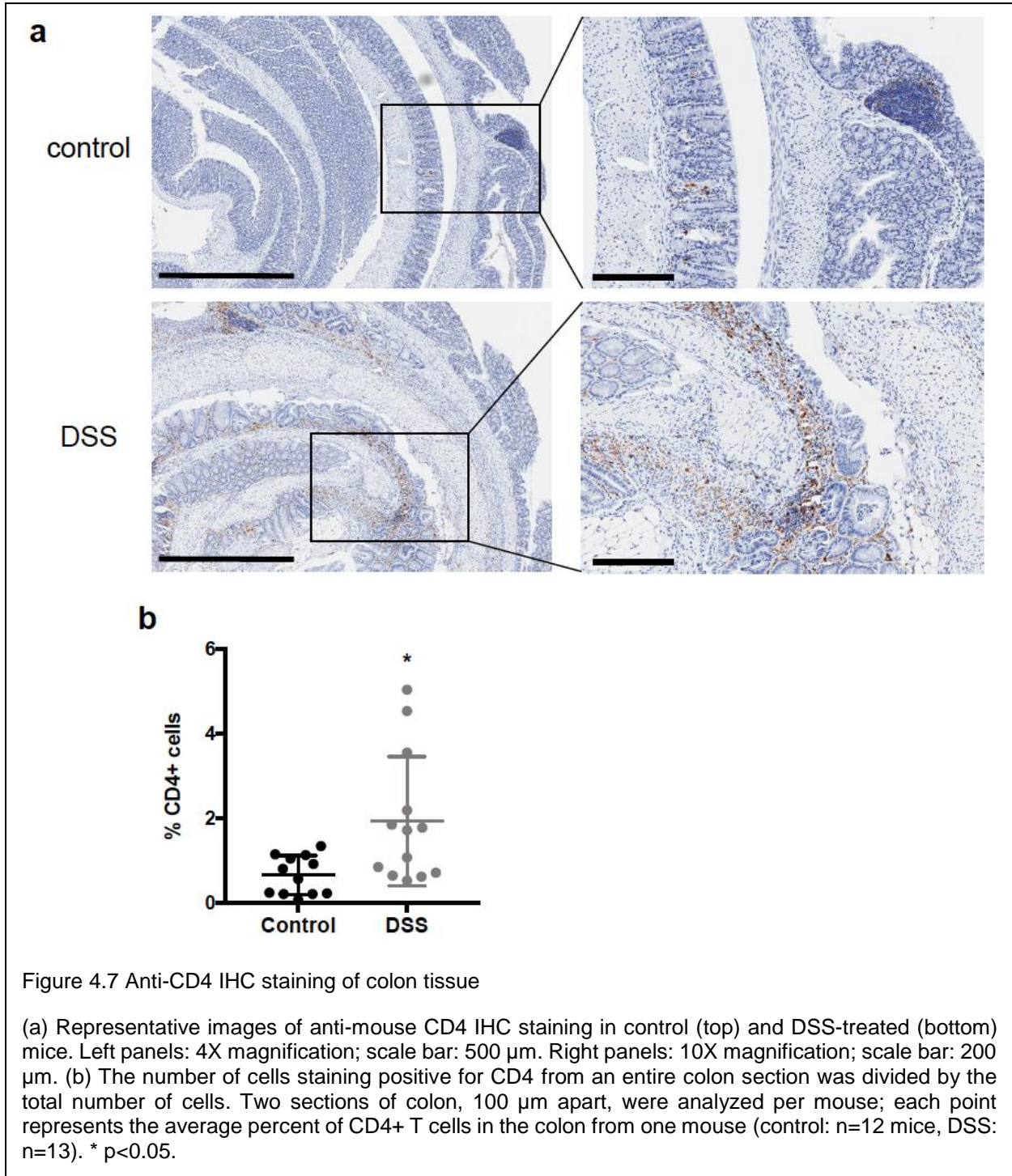
MLN were removed, counted, pooled per mouse, and weighed. Each dot represents the average weight of one MLN from an individual mouse (n=8 mice). * p<0.05.

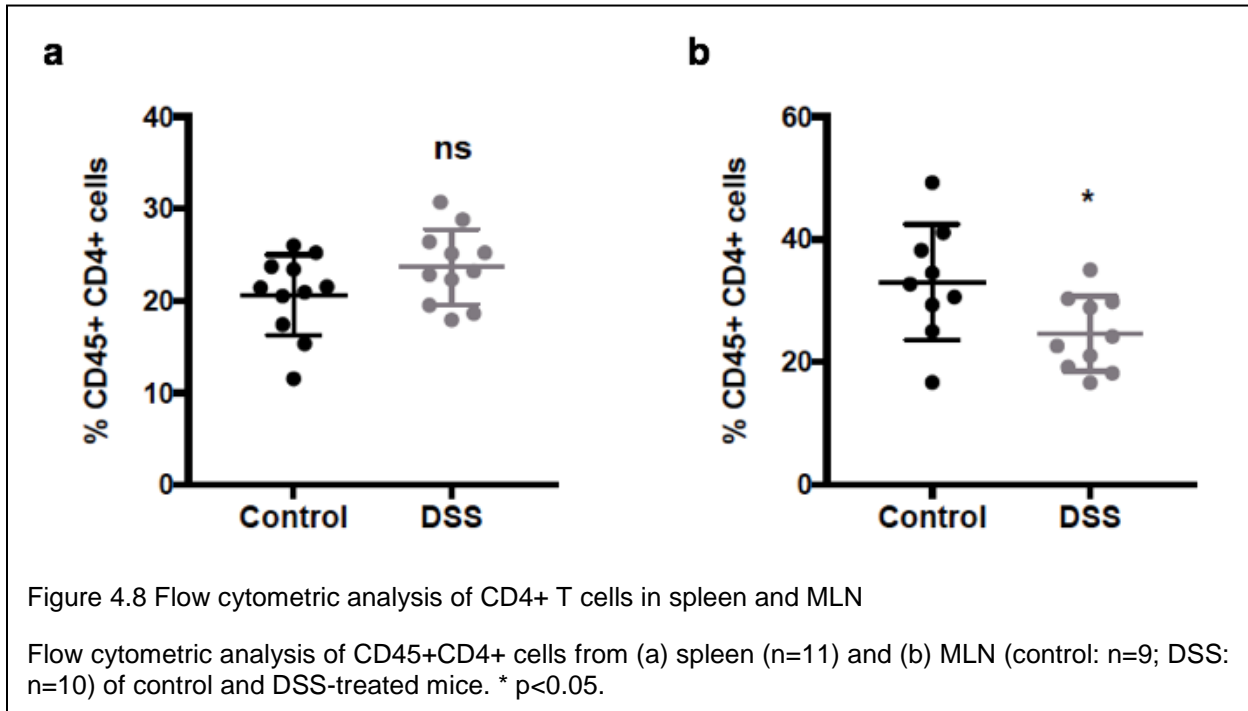


4.3.2 Changes in CD4+ T cells in DSS-treated mice

Anti-CD4 IHC staining showed increased infiltration of CD4+ T cells into the colons of DSS-treated mice. CD4+ cells were on average 0.66 ± 0.46 % of the total cells in each section of colon in control mice, whereas DSS-treated mice had an average of 1.9 ± 1.5 % CD4+ cells ($p < 0.05$; control n=12 mice, DSS n=13 mice) (Figure 4.7). Flow cytometric analysis showed that the percent of CD45+ CD4+ cells in the spleen increased slightly in DSS mice, though not significantly (control: 20.6 ± 4.4 %; DSS: 23.7 ± 4.1 %; n=11 mice) (Figure 4.8a). The percent of CD45+ CD4+ cells in MLN of DSS mice decreased

significantly (control: 33.0 ± 9.4 %; DSS: 24.6 ± 6.1 %; $p < 0.05$; control: $n = 9$ mice, DSS: $n = 10$ mice) (Figure 4.8b).





4.3.3 ImmunoPET imaging of CD4 in colitic mice

GK1.5 cDb was site-specifically conjugated to malDFO and radiolabeled with ^{89}Zr . Specific activity was $0.19 \pm 0.023 \text{ MBq}/\mu\text{g}$ ($9.9 \times 10^5 \pm 1.2 \times 10^5 \text{ MBq}/\text{mmol}$), and radiochemical purity and radiolabeling efficiency were >99% (n=3 labelings). ^{89}Zr -malDFO-GK1.5 cDb (2 μg ; 0.38 MBq) was injected into groups of mice (n=8; two independent experiments of n=4 mice/group). PET imaging confirmed visualization of spleens and by ^{89}Zr -malDFO-GK1.5 cDb (Figure 4.9). Compared to healthy mice, colitic mice had enlarged MLN which were visible in the PET scan (Figure 4.9a). The colons of colitic mice also show uptake of ^{89}Zr -malDFO-GK1.5 cDb, whereas the control mice show little to no uptake in the colon (Figure 4.9a). Oral and intrarectal instillation of CT contrast agent delineated the intestine clearly on the CT scan, and enabled a 3D isocontour ROI of the small and large intestines to be created based on intensity of CT signal after manual

removal of the skeleton. However, DSS-treated mice did not have significantly higher uptake in the intestinal ROI compared to control mice ($p=0.548$; Figure 4.9b).

Ex vivo scans confirmed the results of in the *in vivo* scans, showing a visible increase in uptake in colons, ceca, and MLN from DSS mice (Figure 4.10). The increased uptake seen in the images was further confirmed by *ex vivo* biodistribution studies. Total activity was higher in DSS-treated colons (DSS: 1.75 ± 0.40 % ID/organ, control: 0.45 ± 0.12 %); $p<0.0001$), ceca (DSS: 1.09 ± 0.38 % ID/organ, control: 0.35 ± 0.09 %; $p<0.005$), and MLN (DSS: 1.09 ± 0.58 % ID/organ, control: 0.37 ± 0.25 %; $p<0.05$) (Figure 4.11a; Table 2). On average, % ID/organ in the DSS group was higher by 3.1-fold in colons, 3.9-fold in ceca, and 3.0-fold in MLN. Comparing concentration of activity in each organ did not result in significant changes in uptake (Figure 4.11b; Table 3).

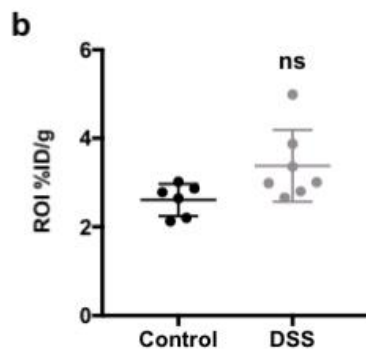
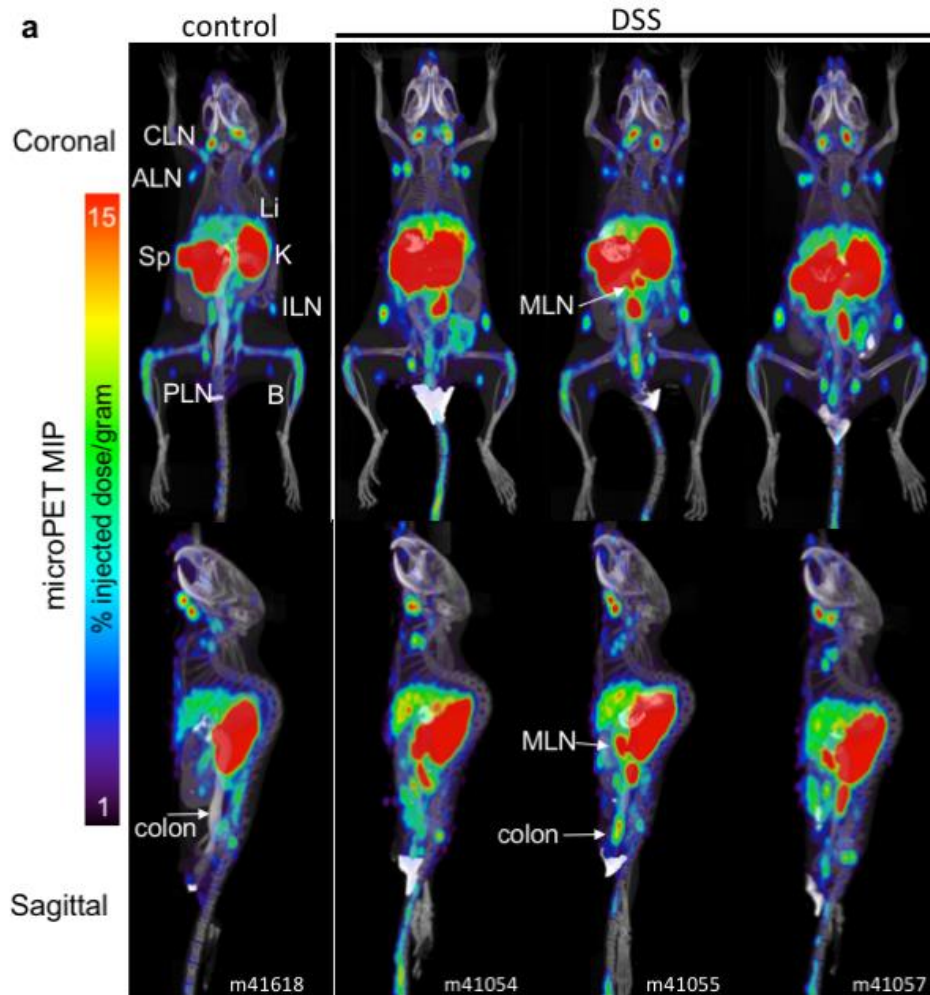


Figure 4.9 Anti-CD4 immunoPET of colitic mice

(a) Representative coronal (top) and sagittal (bottom) images of control or DSS-treated mice imaged with $2\mu\text{g}$ (0.34 MBq) ^{89}Zr -malDFO-GK1.5 cDb ($n=8$). Images were acquired 20 h post-injection of probe and are displayed as 25 mm maximum-intensity projections. Organs of interest are labeled: cervical LN (CLN), axillary LN (ALN), spleen (Sp), liver (Li), kidney (K), inguinal LN (ILN), bone (B), popliteal LN (PLN), mesenteric LN (MLN), colon. (b) Quantitative analysis of ROIs drawn around the intestines, using the 3D isocontour ROI function of AMIDE (control: $n=6$, DSS: $n=7$).

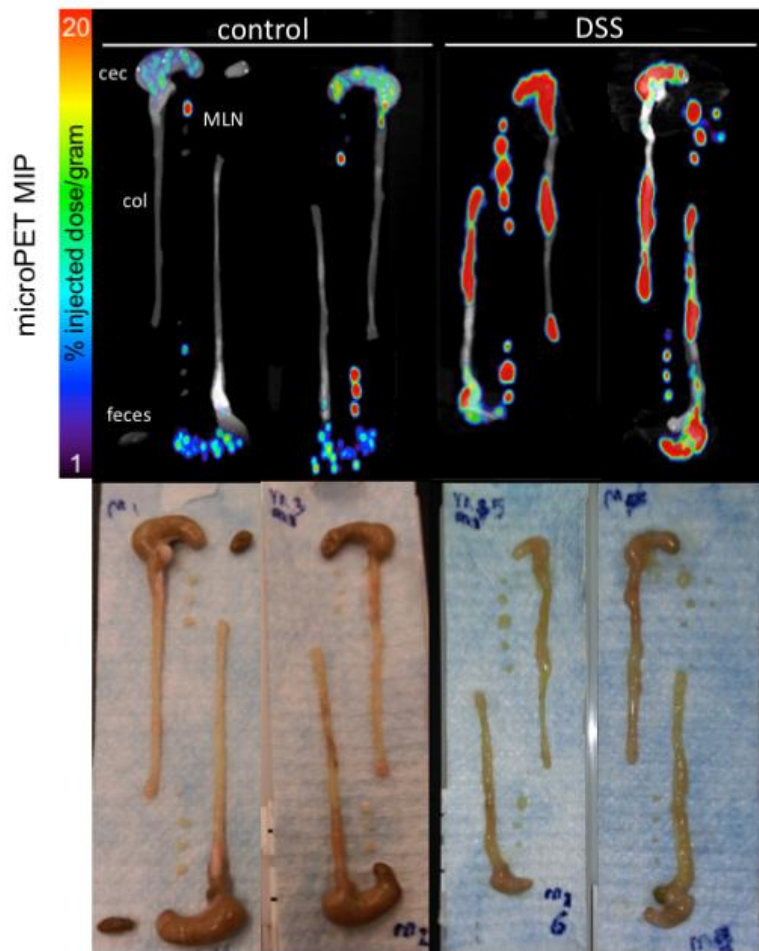


Figure 4.10 *Ex vivo* scans of colons, ceca, and MLN

After the *in vivo* PET/CT scan mice were euthanized, and ceca, colons, and MLN dissected and laid out for the *ex vivo* PET/CT scan (n=8 mice/group). Representative images are shown and displayed as 12 mm maximum-intensity projections.

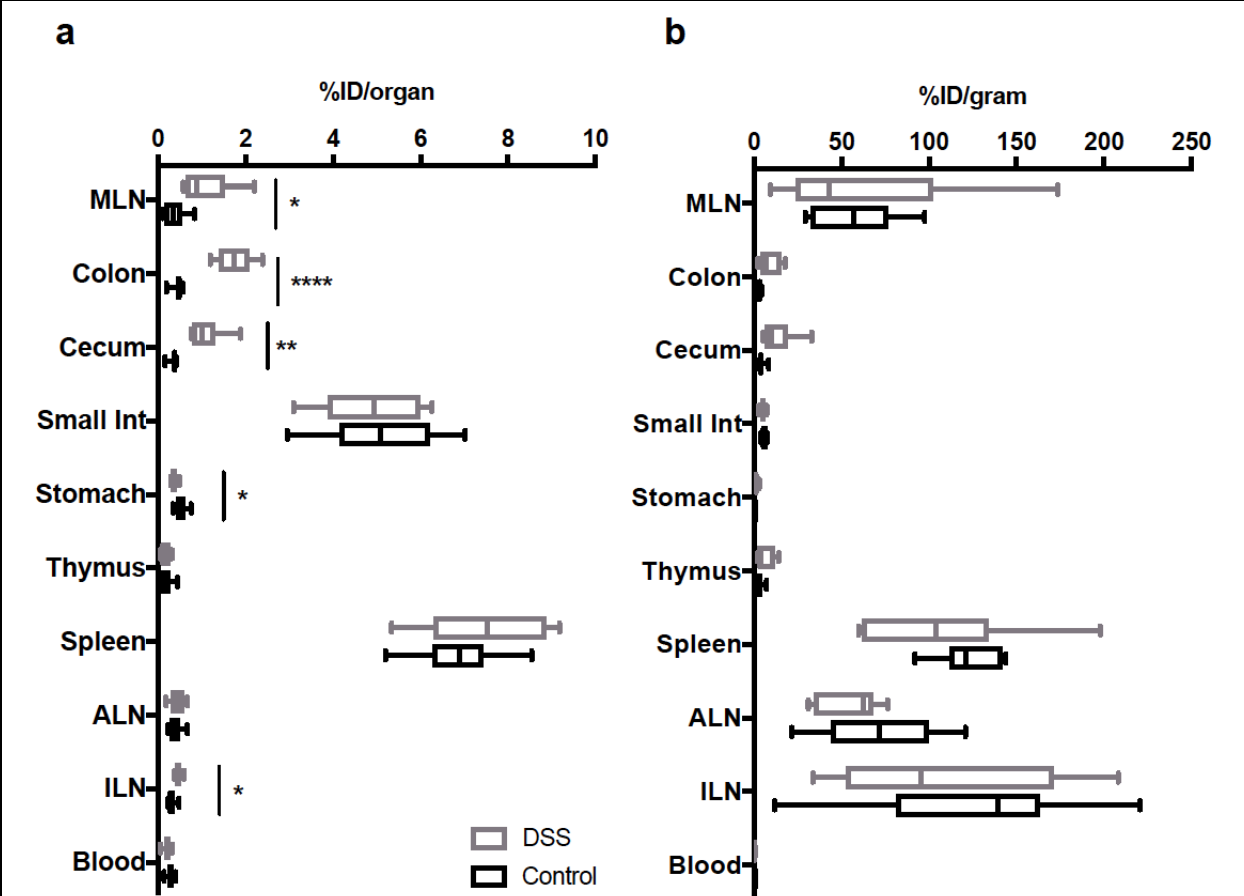


Figure 4.11 Ex vivo biodistribution analysis

After the PET scan, mice were euthanized, and blood and organs were removed, weighed, and counted. Decay-corrected values for uptake are displayed. (a) %ID/organ for lymphoid and gastrointestinal organs. (b) %ID/gram for lymphoid and gastrointestinal organs (n=8). * p<0.05, ** p<0.005, **** p<0.0001.

Table 2 *Ex vivo* biodistribution, % injected dose/organ

	Percent injected dose per organ (%ID/organ)					
	Control			DSS		
	Mean	SD	n	Mean	SD	n
Blood	0.28	0.08	8	0.22	0.08	8
ILN	0.31	0.09	8	0.46 *	0.07	8
ALN	0.41	0.14	8	0.45	0.17	8
Spleen	6.89	0.98	8	7.56	1.38	8
Thymus	0.17	0.14	8	0.16	0.11	8
Liver	9.84	2.64	8	13.37	1.01	8
Kidney	23.84	6.26	8	27.30	3.68	8
Heart	0.15	0.04	8	0.21	0.07	8
Lung	0.38	0.26	8	0.36	0.03	8
Muscle	0.04	0.01	8	0.05	0.01	8
Bone	0.69	0.17	8	0.49	0.10	8
Tail	4.19	3.63	8	3.25	0.72	8
Carcass	19.53	3.24	8	16.64	0.96	8
Stomach	0.53	0.13	8	0.37 *	0.07	8
Small Int	5.12	1.33	8	4.87	1.13	8
Cecum	0.35	0.09	8	1.09 **	0.38	8
Colon	0.45	0.12	8	1.75 ****	0.40	8
MLN	0.37	0.25	8	1.09 *	0.58	8

Total activity present in blood and organs from DSS-treated mice was compared to those from control mice. * $p < 0.05$, ** $p < 0.005$, **** $p < 0.0001$. Abbreviations: axillary LN (ALN), inguinal LN (ILN), mesenteric LN (MLN).

Table 3 Ex vivo biodistribution, % injected dose/gram

	Percent injected dose per gram (%ID/g)					
	Control			DSS		
	Mean	SD	n	Mean	SD	n
Blood	0.6	0.1	8	0.5	0.2	8
ILN	126.4	68.0	6	108.5	65.3	7
ALN	72.7	33.2	7	80.9	69.3	7
Spleen	123.6	18.2	8	106.1	47.4	8
Thymus	3.4	1.9	8	6.0	5.1	8
Liver	11.2	3.0	8	14.9	5.2	8
Kidney	99.6	28.8	8	114.1	36.4	8
Heart	1.6	0.5	8	2.3	1.0	8
Lung	3.2	1.9	8	2.8	0.7	8
Muscle	0.5	0.2	8	0.6	0.3	8
Bone	13.7	4.5	8	9.0	2.2	8
Tail	8.8	7.3	8	10.2	8.7	8
Carcass	1.4	0.3	8	1.5	0.2	8
Stomach	0.9	0.1	8	1.4	0.7	8
Small Int	5.9	1.5	8	5.1	1.6	8
Cecum	4.3	2.1	6	13.5	9.6	8
Colon	3.1	1.0	6	9.1	6.0	8
MLN	56.9	24.3	8	61.7	56.0	8

Activity present in blood and organs from DSS-treated mice was compared to those from control mice. Abbreviations: axillary LN (ALN), inguinal LN (ILN), mesenteric LN (MLN).

4.4 Discussion

Aberrant activation and infiltration of CD4+ T cells is a hallmark of IBD in humans, and in numerous mouse models of IBD. ImmunoPET with anti-mouse CD4 probe ⁸⁹Zr-malDFO-GK1.5 cDb successfully detected CD4+ T cells in the colons and mesenteric lymph nodes (MLN) of colitic mice, and identified enlarged MLN where T cells accumulate in the context of gut inflammation. *Ex vivo* scans and biodistribution analysis confirmed increased presence of CD4+ T cells in colons, ceca, and MLN from DSS-treated mice. These findings demonstrate that anti-CD4 immunoPET may be useful for investigating abdominal foci of inflammation in which CD4+ T cells are present.

In the present study, after 5 days of 4% DSS administration, treated mice displayed signs of weight loss, loose stool, and fecal bleeding (Figure 4.2). DSS colons were shortened and the MLN were enlarged (Figure 4.4, Figure 4.6). DSS-induced damage to the epithelium and crypts and infiltration of inflammatory cells was confirmed by histopathological analysis of the colon (Figure 4.6). The percent of CD4+ T cells was significantly increased in the colons of DSS-treated mice on d 12 (Figure 4.7), as expected (Dieleman et al., 1998; Hall et al., 2011; Morgan et al., 2013). In accord with previous work, no significant change in the percent of splenic CD4+ T cells from colitic mice was detected, and MLN showed a decrease in the percent of CD4+ T cells (Figure 4.8) (Hall et al., 2011); however, MLN were enlarged and had increased cellularity compared to control MLN (Figure 4.5).

The presence of CD4+ T cells in the colon of DSS-treated mice on d 12 was confirmed by immunoPET imaging with ⁸⁹Zr-malDFO-GK1.5 cDb (Figure 4.9). According to previous work, the most severe damage in the DSS model has been reported to occur

in the distal portion of the colon (Dieleman et al., 1994; Kitajima et al., 1999); here, the *ex vivo* scans show that CD4+ T cell infiltration occurs throughout the colon and the cecum (Figure 4.10). Furthermore, observation of enlarged MLN in colitic mice, which were clearly visible on both PET scans, demonstrates the importance of CD4+ T cells within MLN and associated lymphatics in the development of DSS colitis and raises the possibility of the prognostic value of inflammatory staging sites such as MLN.

Quantification of uptake via *ex vivo* biodistribution confirmed a significant increase in %ID/organ for colons, ceca, and MLN of DSS-treated mice (Figure 4.11a; Table 2). However, when represented as %ID/g, uptake was not significantly higher in DSS mice (Figure 4.11b, Table 3). For the colon, this may be due to the increased weight/length ratio in DSS mice. In DSS-treated MLN, although there was a decrease in the percent of CD4+ T cells, the MLN were significantly enlarged which suggests that both CD4+ T cells and other types of immune cells (such as B cells) were present in higher numbers, resulting in heavier weight but not increased uptake. In recent work from our lab, in which we imaged murine immune cell reconstitution post-stem cell transplantation, a similar lack of increased %ID/g was observed; as the inguinal lymph nodes grew larger over a period of weeks, the %ID/g remained constant despite an increase in % CD8+ T cells (Tavaré et al., 2015). Quantifying uptake in an ROI encompassing the small and large intestines presented a challenge because the probe cleared through the kidneys, resulting in signal spillover into the anterior region of the ROI; differences in ROI values were not significant between control and DSS-treated mice (Figure 4.9b). In future studies, the problem of kidney spillover could be addressed by using a higher molecular weight probe that clears

through the liver. Furthermore, identifying foci of intestinal inflammation in humans may be more straightforward as the intestines are much larger.

These results confirm and expand on the work of Kanwar *et al.*, who employed indium-111-labeled intact anti-CD4 antibody for SPECT imaging of CD4+ T cells in DSS mice; in that work, a protein dose of 350 μg was used (Kanwar *et al.*, 2008). We previously explored protein doses and found that amounts as low as 2 μg GK1.5 cDb enabled imaging CD4+ T cells in the lymph nodes and spleen with minimal biological effects (Freise *et al.*, in press). Here, 2 μg GK1.5 cDb was sufficient to image CD4+ T cells in the DSS model. In addition, PET is up to two orders of magnitude more sensitive than SPECT (James and Gambhir, 2012), allowing imaging with a lower radiation dose which is of particular importance for imaging radiosensitive immune cells (McCracken *et al.*, 2016). ImmunoPET with GK1.5 cDb was performed using 0.38 MBq/mouse, whereas anti-CD4 SPECT imaging used 100-fold higher activity (34 MBq/mouse) (Kanwar *et al.*, 2008). Finally, Kanwar *et al.* drew an ROI that encompassed the entire lower abdomen and referred to this as “colon uptake” but did not discuss signal from CD4+ T cells in the MLN (Kanwar *et al.*, 2008), which are likely to have been included in the ROI. Therefore, while whole-abdomen ROIs may have prognostic value in IBD, they must be interpreted with the consideration of the presence of MLN and associated lymphatic tissue.

While the use of GK1.5 cDb enabled visualization and quantification of total CD4+ cells in the gut, it does not provide information about CD4+ T cell subsets such as Th1, Th2, Th17, or Tregs, which is disadvantageous given the different pro- and anti-inflammatory roles of each of these subsets. However, GK1.5 cDb can still be used to identify multiple sites where CD4+ T cells are present, and more detailed analysis by

traditional methods such as biopsy can then be performed to determine the subsets present. Further studies using GK1.5 cDb in mouse models of IBD could include imaging CD4 in a T-cell dependent model or imaging at several timepoints during the development of colitis to investigate the course of T cell infiltration into the intestines and MLN.

CD4⁺ T cells play a key role in human IBD, and identifying them throughout the bowel could be of use in monitoring disease severity and predicting treatment success. Molecular imaging is less intrusive than colonoscopies, which are uncomfortable for patients and carry a small risk of bowel perforation; furthermore, inflammation can vary depending on the position within the bowel. Anti-CD4 immunoPET could provide an overview of inflammatory sites throughout the intestines, from which sites for additional diagnostic methods such as biopsy could be chosen. Other immune targets, including granulocytes (Bruno et al., 2002), E-selectin (Bhatti et al., 1998), and CXCL8 (Aarntzen et al., 2016), have been imaged in IBD patients. Aarntzen et al. suggest that anti-CXCL8 imaging could be used as a tool for making decisions about immune-modulating treatment (Aarntzen et al., 2016); a similar application could apply for anti-CD4 imaging.

Anti-CD4 imaging could also aid in diagnosis and monitoring of other diseases, disorders, and treatments. Standard blood samples can be used to monitor lymphocytes, but only a fraction (<2%) of all lymphocytes are in the blood at any one time (Trepel, 1974); the rest reside in other immune compartments including the gut and gut-associated lymphoid tissue. Anti-CD4 immunoPET was recently used to image repopulation of CD4⁺ T cells in the gut and other lymphoid tissues of macaques infected with simian immunodeficiency virus and treated with antiretroviral therapy and anti- $\alpha 4\beta 7$ integrin antibody (Byrareddy et al., 2016); it has also been used to image inflamed joints in

patients with rheumatoid arthritis (Steinhoff et al., 2014). Recognition of the role of CD4+ T cells in cancer immunotherapies (Zanetti, 2015) suggests that imaging lymphocytes in the context of cancer could provide a comprehensive assessment of CD4+ T cells within a tumor as well as systemically.

Anti-CD4 immunoPET with GK1.5 cDb enabled detection of CD4+ T cells in inflamed mouse colons and in enlarged MLN, and should provide a useful tool for investigating CD4+ T cells in murine models of IBD and cancer immunotherapy.

5 ImmunoPET imaging of CD4+ T cells in colitic mice after cyclosporin A immunosuppressive treatment

5.1 Introduction

Treatment of IBD often utilizes anti-inflammatory or immune-modulating drugs to suppress inflammation in the intestines. The widespread use of the DSS mouse model, and its similarities to human ulcerative colitis, have also made it a common model for testing therapeutic agents. Many agents, including steroids, antibodies, and peptides, have been explored in the DSS model. Prednisolone, a corticosteroid, was found by multiple groups to ameliorate signs of colitis as measured by the disease activity index, but had variable effects on body weight loss (J. M. Kim et al., 2010; Sha et al., 2013), including an increase in weight lost in at least one study (Yamamoto et al., 2013). Sulfasalazine is a small molecule with poor absorption in the intestine; when delivered orally it improved weight loss and DAI if given preventatively (starting on the same day as DSS treatment) (J. M. Kim et al., 2010; S. J. Kim et al., 2010), but did not improve weight loss if given as a post-DSS treatment (Sha et al., 2013). Anti-IL-12/23p40 showed promising effects in two studies, reducing weight loss and improving DAI scores when delivered during and/or after DSS treatment (Melgar et al., 2008; Sha et al., 2013). Anti-TNF α antibody appears to have pro- or anti-inflammatory effects depending on the phase of colitis during which it is administered. One group found that when delivered during acute colitis (100 μ g daily during d3-7, during DSS treatment of d1-7), anti-TNF α worsened symptoms of colitis; if chronic colitis was induced by treating mice with multiple

cycles of DSS and normal drinking water, the antibody ameliorated colitis (Kojouharoff et al., 1997). On the contrary, Sha et al. found that administration of anti-TNF α (0.1mg/kg, on d5 and d8) during the acute phase significantly ameliorated colitis (Sha et al., 2013); this effect may be due to the lower dose used in comparison to Kojouharoff et al. These results are especially interesting because two approved drugs for treatment of clinical IBD are anti-TNF α antibodies infliximab and adalimumab. While these antibodies are efficacious for some patients, treatment of IBD with anti-TNF α remains a challenge because 10-40% of patients are non-responders (Ben-Horin et al., 2014), and only a third of primary responders remain in remission after one year (Danese, 2012), indicating a need for better prediction of treatment response.

Cyclosporin A (also known as cyclosporine) is an immunosuppressant commonly used after transplantation to prevent graft rejection and graft-versus-host disease. The inhibitory actions of CsA on T cells have been well characterized: CsA forms a complex with cyclophilins in the cytoplasm and then blocks the phosphatase activity of calcineurin, inhibiting translocation of NFAT transcription factors into the nucleus and halting transcription of cytokine genes including IL-2 and IL-4 (Matsuda and Koyasu, 2000). While CsA is known as a selective T cell suppressor, studies suggest it has effects on other immune cells as well. Neutrophils treated with CsA *in vitro* had reduced mobility, superoxide production, and degranulation (Spisani et al., 2001). Another study found that CsA treatment attenuated airway hyperresponsiveness in mice but that this effect was not due to inhibition of T cells; the authors suggested that other cells such as eosinophils may have been indirectly inhibited, resulting in decreased inflammation (Ewart et al.,

1996). CsA was also able to induce changes in cytokine release by alveolar macrophages, although these changes were mild (Losa Garcia et al., 1998).

CsA has been used with mixed success to treat DSS colitis. Melgar et al. found that 25 mg/kg delivered orally on d 1-7 resulted in amelioration of weight loss, improved DAI, and improved histopathological score of damage in the colon (Melgar et al., 2008). Sann et al. confirmed that 25 mg/kg delivered orally on d 1-8 ameliorated weight loss, but did not improve DAI or histopathological scoring; they also found that 50 mg/kg improved all parameters, but noted that the mice drank less DSS-treated water which may be the actual reason for decreased colitis severity (Sann et al., 2013). Others have suggested that the route of CsA administration is crucial to treatment success: Murthy et al. reported that oral administration of CsA had no effect on colitis, but that intrarectal instillation of the drug at 2.5 mg/kg resulted in complete amelioration of disease (Murthy et al., 1993).

The reported success of CsA when delivered during acute colitis is an interesting finding, because although T cells begin infiltrating into the colon as early as d 3 after DSS initiation, they do not reach peak levels until 1-2 weeks later (Hall et al., 2011). Imaging could be a useful tool not only to assess the potential of CsA as a therapeutic agent in this model, but also to determine whether its success or failure has anything to do with its effect on CD4⁺ T cells in the gut. Here, we administered CsA to DSS-treated mice and used anti-CD4 immunoPET to determine whether amelioration of colitis was due to a change in the presence of intestinal CD4⁺ T cells.

5.2 Materials and Methods

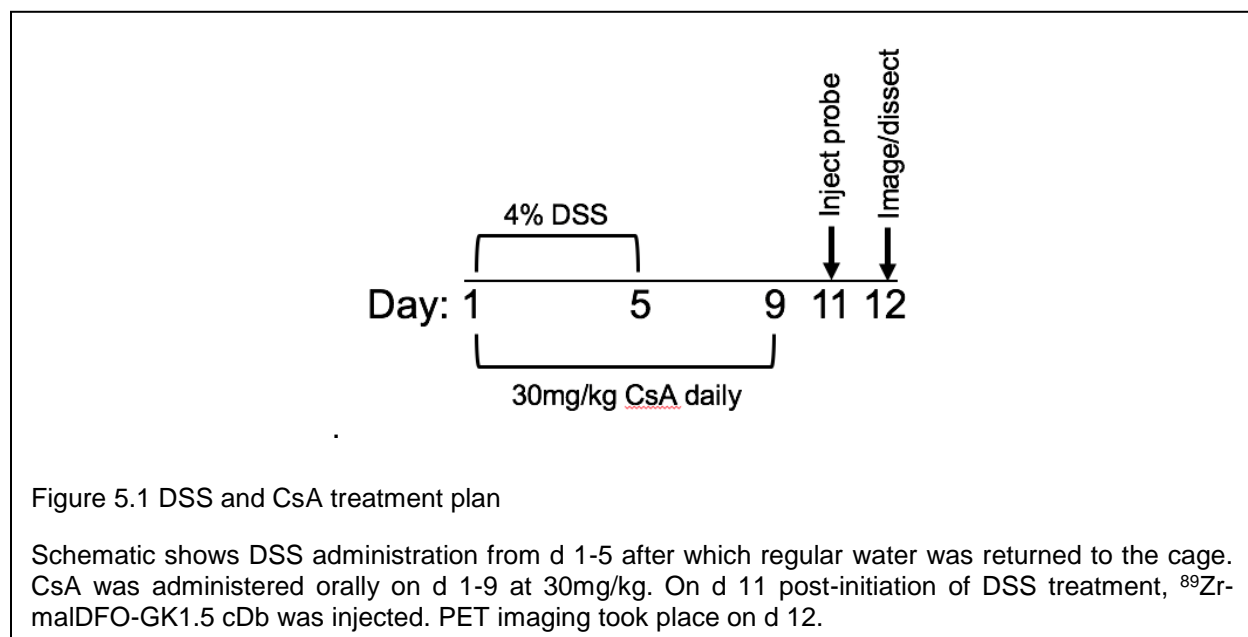
DSS treatment, analysis, and imaging were carried out as in Chapter 4. Additional details are provided here regarding CsA treatment.

5.2.1 Preparation of CsA

Lyophilized CsA was dissolved in 100% EtOH and aliquoted for storage of stocks at -80°C . On each day of treatment, one aliquot of CsA was diluted roughly 1:10 in olive oil and mixed well to produce an emulsion.

5.2.2 CsA treatment

Treatment began on the same day as DSS administration (d1) and continued until d9 (Figure 5.1). Each day, CsA-olive oil emulsion was administered to mice via oral gavage at 30mg/kg.



5.3 Results

5.3.1 CsA treatment ameliorates some signs of colitis

CsA-treated mice tolerated repeated oral gavage well during d 1-9. Weight loss began on d 6 and continued until approximately d 9; for mice treated with CsA, weight loss was less severe (Figure 5.2). On d 12, the body weight of DSS+CsA-treated mice was still significantly decreased compared to that of control mice, but weight loss was slightly ameliorated compared to DSS-only mice (Figure 5.2). DSS+CsA treated mice also had a significant reduction in DAI scores compared to DSS-only mice, indicating improvement of signs such as weight loss, loose stool, and fecal bleeding (Figure 5.3).

CsA treatment improved colon length, but not the colon weight:length ratio, indicating that colons from CsA-treated mice were still heavier despite their length being returned to normal. (Figure 5.3). The average weight of an individual MLN from

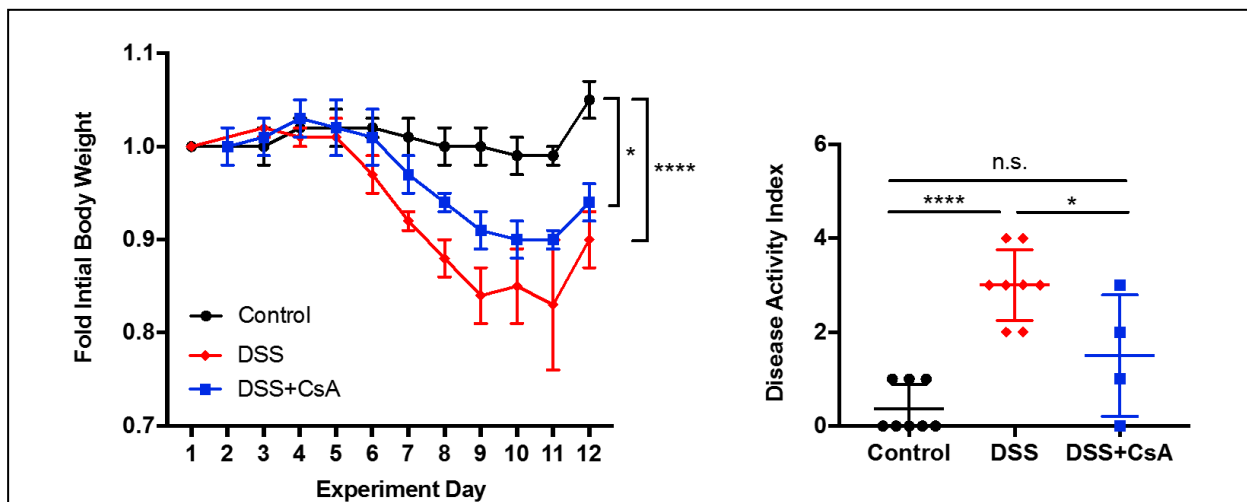


Figure 5.2 Effects of CsA on body weight and disease activity index

Average change in body weight during and after DSS treatment (n=8). Clinical symptoms were quantified using the disease activity index (DAI), which scored symptoms including weight loss, stool consistency, and fecal bleeding, at the time of sacrifice (control/DSS: n=8; DSS+CsA: n=4). $p < 0.05$, **** $p < 0.0001$.

DSS+CsA-treated mice was decreased compared to DSS-treated mice, and not significant compared to control mice (Figure 5.4).

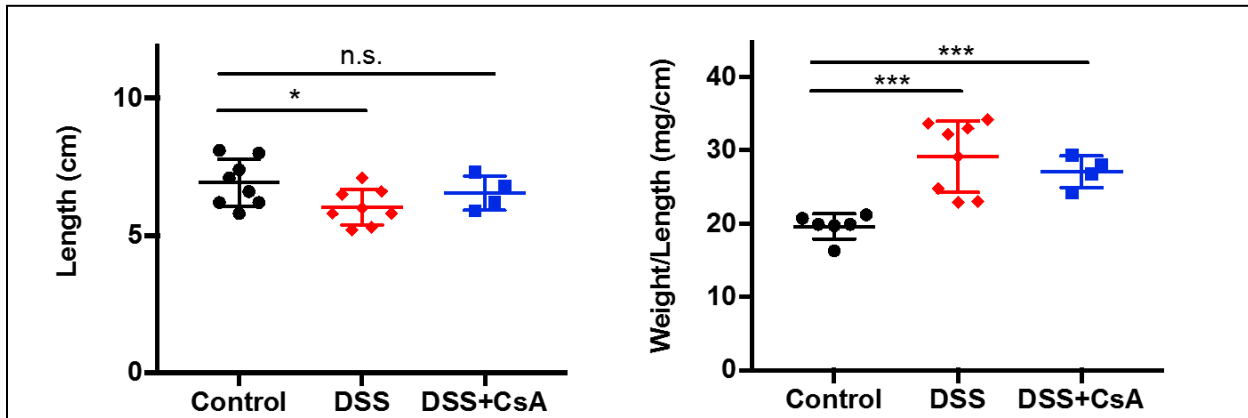


Figure 5.3 Effects of CsA on colon gross anatomy

Colons were cut just below the cecum, laid flat next to a ruler, and measured. The ratio of colon weight to length was determined after removing stool from the colon (control/DSS: n=8; DSS+CsA: n=4). * p<0.05, *** p<0.0005.

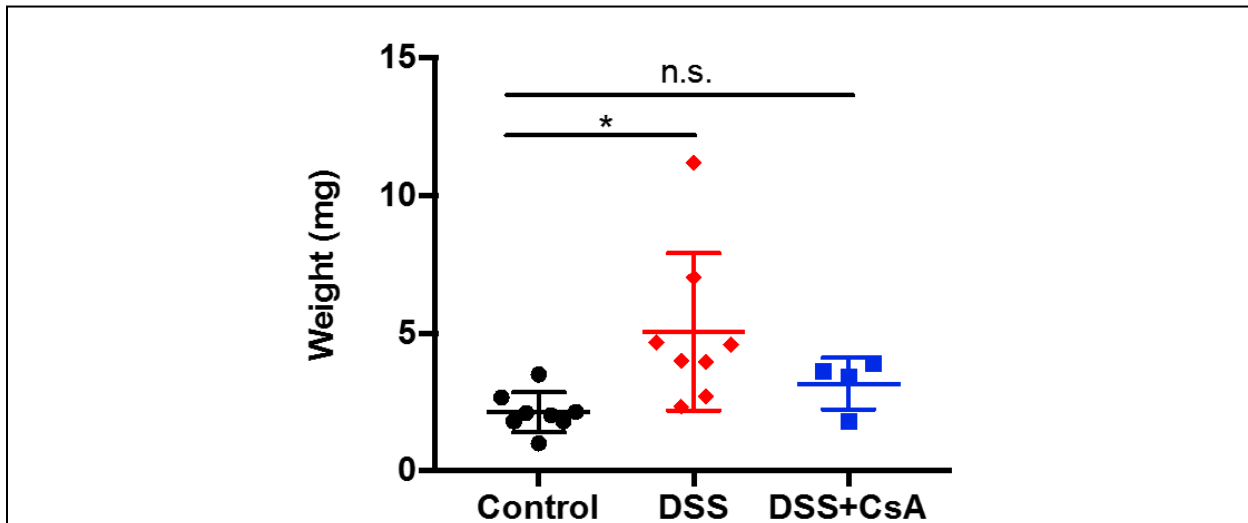
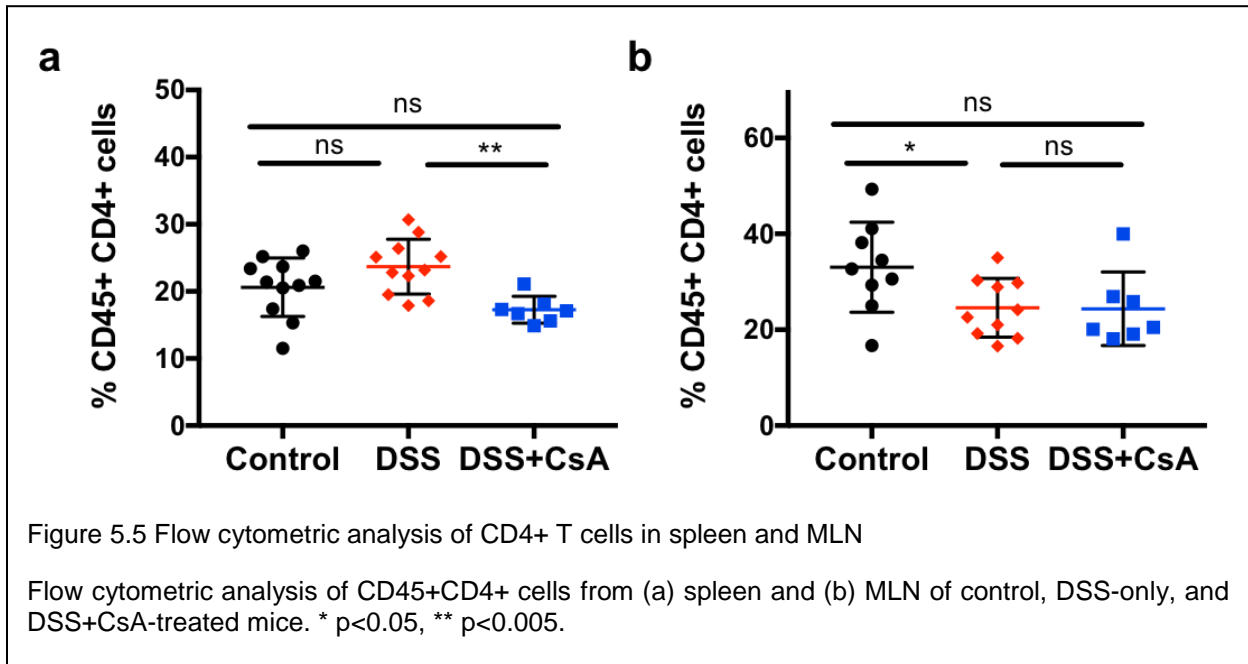


Figure 5.4 Effects of CsA on average MLN size

MLN were removed, counted, pooled per mouse, and weighed. Each dot represents the average weight of one MLN from an individual mouse (control/DSS: n=8; DSS+CsA: n=4). * p<0.05.

5.3.2 CsA treatment alters percentage of CD4+ T cells in the spleen

Flow cytometric analysis showed that the percent of CD45⁺ CD4⁺ cells in the spleen was not significantly changed, but mice treated with DSS+CsA had a significant decrease in the percent of this population (control: 20.6 ± 4.4 %; DSS: 23.7 ± 4.1 %; DSS+CsA: 17.3 ± 2.0 %; control, DSS: n=11, DSS+CsA: n=7) (Figure 5.5a). The percent of CD45⁺ CD4⁺ cells in MLN of both DSS-only and DSS+CsA-treated mice decreased significantly (control: 33.0 ± 9.4 %; DSS: 24.6 ± 6.1 DSS+CsA: 24.4 ± 7.7 %; control: n=9 mice, DSS: n=10 mice, DSS+CsA: n=7) (Figure 5.5b).



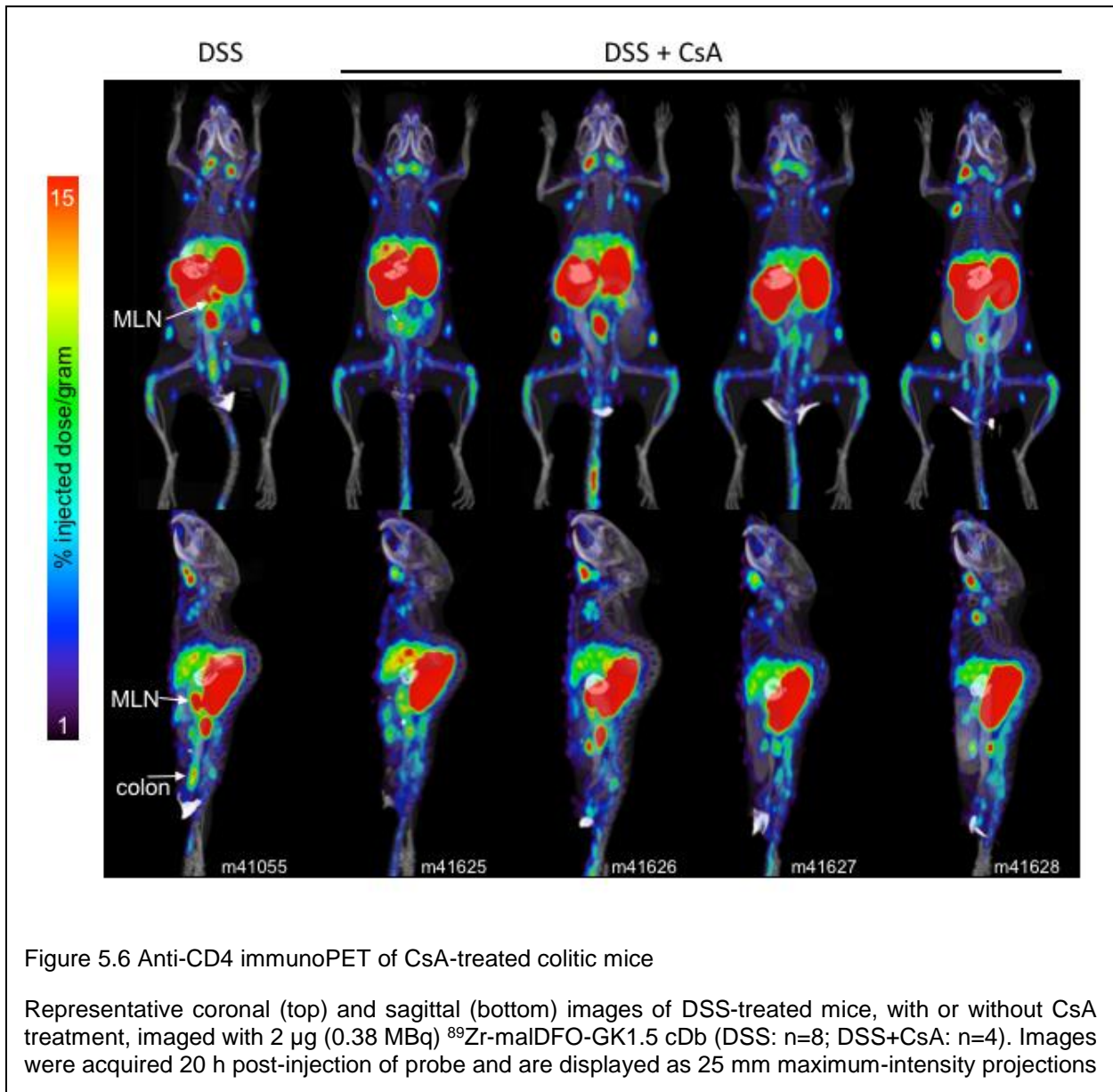
5.3.3 Anti-CD4 immunoPET imaging of CsA-treated mice

GK1.5 cDb was site-specifically conjugated to maIDFO and radiolabeled with ⁸⁹Zr as in Chapter 4. The specific activity was 0.19 ± 0.023 MBq/μg and radiochemical purity and radiolabeling efficiency were >99%. ⁸⁹Zr-maIDFO-GK1.5 cDb (2 μg; 0.38 MBq) was injected into groups of mice: control, DSS-treated, and DSS+CsA-treated (n=4

mice/group). Here, images from a representative DSS-treated mouse and all four DSS+CsA-treated mice are shown (Figure 5.6). The CsA-treated mice show a range of ^{89}Zr -malDFO-GK1.5 cDb uptake: for example, one mouse showed uptake in the distal colon (m41625) whereas the other mice did not. However, all DSS+CsA-treated mice showed increased signal in MLN, many but not all of which were enlarged (Figure 5.6). Two mice showed low uptake in the intestinal region (m41627 and m41628), comparable to control mice (data not shown).

The variability between mice in *in vivo* scans was also seen in the *ex vivo* scans of the colons, ceca, and MLN (Figure 5.7). Colons from two DSS+CsA-treated mice showed high uptake in the cecum and along the colon, similar to that seen in colons from all DSS-treated mice. However, the other two colons and ceca showed only minimally increased uptake in localized regions of the colon.

Ex vivo biodistribution studies showed that there was no significant change in uptake in any organ from DSS+CsA-treated mice compared to DSS-treated mice (Figure 5.8). When data is represented as total activity per organ (Figure 5.8a), there appears to be a slight downward trend in activity in the colons, ceca, and MLN of DSS+CsA-treated mice, but this difference was not statistically significant. Comparing concentration of activity in each organ did not result in significant changes in uptake (Figure 5.8b).



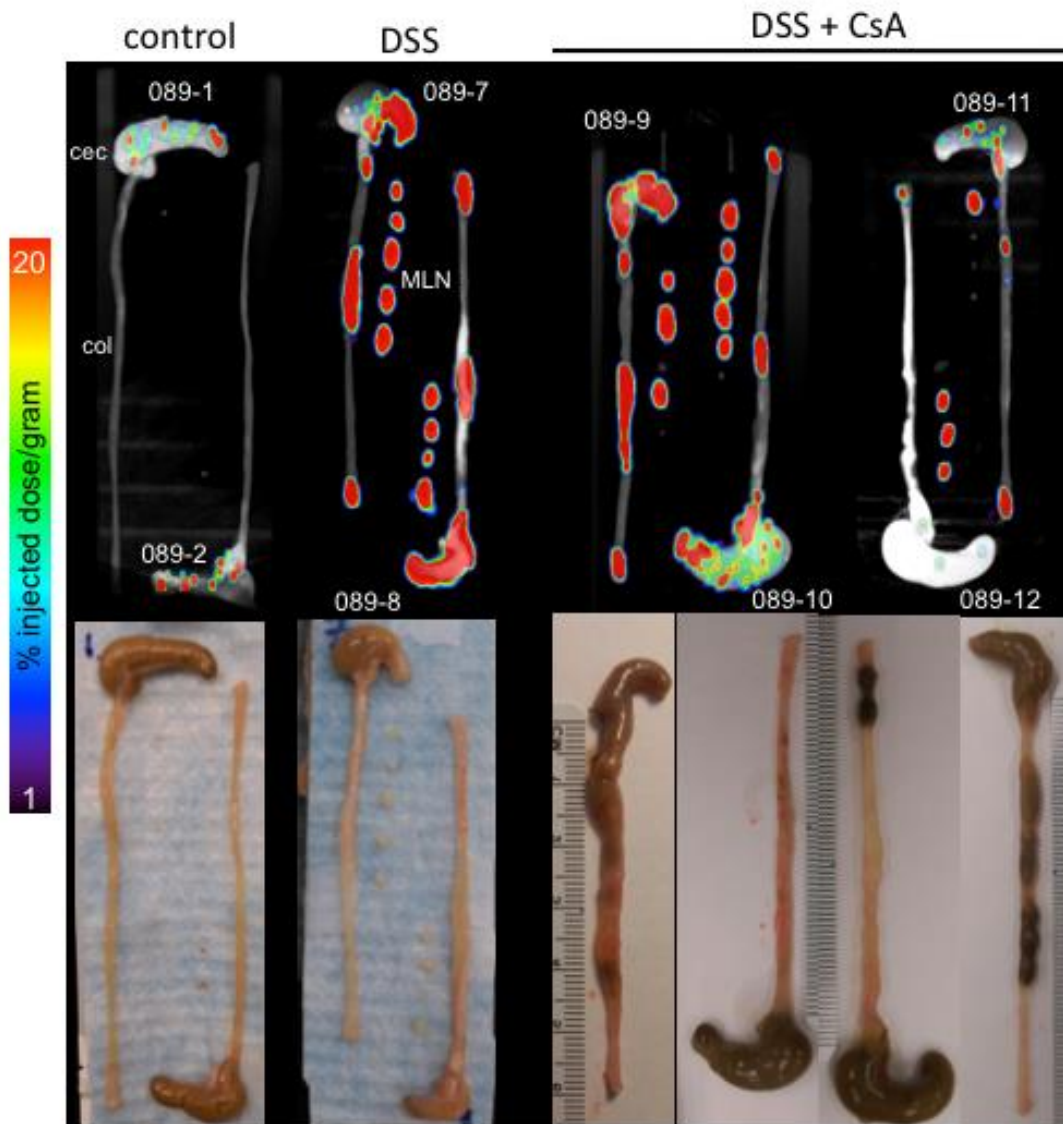
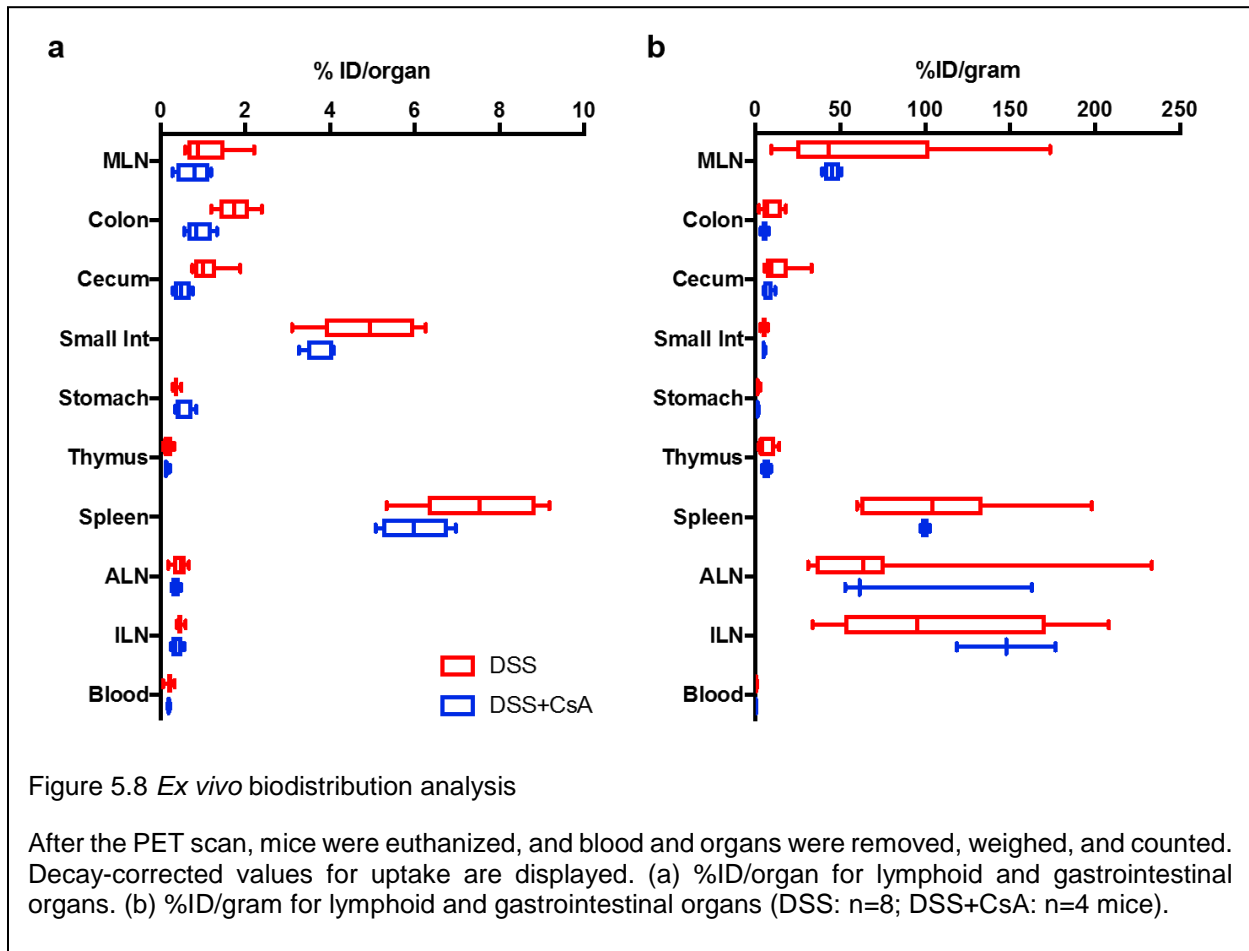


Figure 5.7 *Ex vivo* scans of colons, ceca, and MLN

After the *in vivo* PET/CT scan mice were euthanized, and ceca, colons, and MLN dissected and laid out for the *ex vivo* PET/CT scan (DSS: n=8; DSS+CsA: n=4 mice). Representative images are shown and displayed as 12 mm maximum-intensity projections.



5.4 Discussion

ImmunoPET can be used to determine whether a treatment is affecting cells of interest. Here, although CsA ameliorated some signs of DSS colitis, there was no significant change in GK1.5 cDb uptake in the colon or MLN of DSS mice treated with CsA. These results indicate that although CsA was somewhat successful as a therapeutic agent, anti-CD4 immunoPET could not detect a statistically significant change in the presence of CD4+ T cells in the colons of colitis mice.

CsA treatment returned colon length of DSS-treated mice to that of healthy mice, but did not improve the colon weight:length ratio (Figure 5.3). The increased weight of DSS+CsA treated colons compared to healthy colons might have been due to residual inflammation. Importantly, CsA reduced MLN weights to those of healthy mice (Figure 5.4), and the immunoPET images showed fewer enlarged MLN in DSS+CsA-treated mice compared to DSS-only mice (Figure 5.6), indicating that an effect of CsA treatment in colitic mice may be to reduce the total number of immune cells in MLN. The percent of CD4+ T cells was still decreased in DSS+CsA-treated lymph nodes (Figure 5.5b), which is expected due to the inhibitory effect of CsA on T cells.

Although CsA did not significantly decrease ^{89}Zr -maIDFO-GK1.5 cDb uptake in colons, ceca, or MLN compared to DSS-only treated mice (Figure 5.8), there was a trend of decreased uptake, and the *in vivo* PET images show less uptake in those organs in CsA-treated mice (Figure 5.6). The *ex vivo* PET images of colons, ceca, and MLN demonstrate the variability in treatment success: half the mice appeared to have benefited from CsA treatment, while the other half did not (Figure 5.7). This study was limited by the small number of animals treated with CsA; a bigger sample size might address the issue of variability.

The increased presence of CD4+ T cells in the colons of DSS+CsA-treated mice was not unexpected. Previous works have shown that CD4+ T cells begin to infiltrate into the gut in later stages of colitis, and contribute to chronic colitis, although their role is not yet clear. Since CsA was delivered on d 1-9, during the acute stage of colitis, there may have been few CD4+ T cells present for the CsA to act upon. Whether CsA can affect

CD4+ T cells in the DSS model could be tested by administering CsA during later stages and imaging later.

Despite the continued presence of CD4+ T cells in CsA-treated mice as determined by immunoPET and *ex vivo* biodistribution, CsA still had a therapeutic effect on DSS-treated mice. This suggests that the therapeutic mechanism of CsA in this particular mouse model may be to suppress or inhibit other immune cells. Imaging DSS- and DSS+CsA-treated mice with an antibody fragment specific for neutrophils or macrophages would indicate whether CsA prevents accumulation of these cells in the colon, cecum, and MLN of colitic mice.

While anti-CD4 immunoPET was unable to image the effects of CsA treatment in this colitis model, other works published recently have shown the value of molecular imaging (both nuclear and optical) in predicting treatment success in IBD. For example, the anti- TNF α adalimumab antibody is commonly used to treat Crohn's disease, but only about 50% of patients respond to treatment. To address this problem, Atreya et al. topically applied fluorescently-labeled adalimumab inflamed regions of the bowel during a colonoscopy, and quantified fluorescence with confocal laser endomicroscopy. TNF α expression correlated with the response rate to subsequent therapeutic adalimumab, thereby enabling stratification of patients into responders and nonresponders (Atreya et al., 2014). In addition, a clinical study using ^{99m}Tc -labeled CXCL8 for SPECT imaging of neutrophils, CD8+ T cells, and macrophages in human inflammatory bowel disease found that the probe had good sensitivity for detecting active disease, but that its specificity was lower compared to traditional endoscopy (Aarntzen et al., 2016); however, the authors suggested that the probe could still be useful for making decisions regarding immune-

modulating drugs. Therefore, anti-CD4 immunoPET still holds promise for imaging response to treatment, especially in preclinical models which are T cell-dependent, and in human IBD, which is characterized by aberrant T cell responses.

6 Conclusions

In this dissertation, I characterized the dose-dependent functional effects of the anti-mouse CD4 antibody fragment, GK1.5 cDb, on CD4⁺ T cells *in vitro* and *in vivo*. I investigated the effect of protein dose on immunoPET image contrast and biodistribution. Finally, I used GK1.5 cDb to detect CD4⁺ T cells in the colons and mesenteric lymph nodes of mice with inflammatory bowel disease, demonstrating the potential for this probe and others to track specific cell subsets involved in inflammation.

When designing an antibody fragment probe for molecular imaging, protein dose is a key factor for consideration. Testing multiple doses of GK1.5 cDb gave insight into how both imaging and biological effects can be influenced by the dose of protein given. In *in vivo* studies, 2 μg was sufficient for immunoPET imaging of target lymphoid organs and also resulted in less inhibition of proliferation and CD4 expression compared to the 40 μg dose. Importantly, the 2 μg dose was also sufficient to image CD4⁺ T cells outside of the antigen sink in colitic mice. Future studies might investigate the possibility of imaging with even less than 2 μg , as less protein appears to result in reduced functional effects on the cells of interest. However, there is likely a lower limit of dose, as enough probe must be administered to image outside of the antigen sink. Dose may need to be optimized for different applications as well: for example, monitoring early CD4⁺ T cell reconstitution in a patient with HIV may require an extremely low dose to image outside of the antigen sink, whereas disorders with normal or excess CD4⁺ T cells will need a higher dose.

Molecular imaging has the potential to improve investigation of large and complex organs such as the intestines, since it can survey the entire organ simultaneously, potentially reducing the need for invasive procedures such as endoscopy and biopsy. Increased regional uptake was seen in the colons and MLN of colitic mice imaged with GK1.5 cDb, demonstrating the utility of immunoPET in detecting localized inflammation. However, quantification of GK1.5 cDb uptake in the intestines of mice proved to be a challenge. Oral and intrarectal administration of CT contrast agent delineated the small and large intestine and allowed an ROI to be drawn, but the proximity of the kidneys resulted in PET signal spillover into the ROI. The increase of uptake in the colon of DSS mice was minor in scale compared to the intensity of the kidney, so this increase was likely masked by the kidney signal, resulting in a statistically insignificant change. Using a larger probe, such as a minibody, that clears through the liver might improve quantification of gut ROIs, but the liver is also proximal to the intestines, so it is unlikely that this would completely address the issue. A non-residualizing radiolabel would not be appropriate to image CD4 when using a bivalent probe, as changes in CD4 expression after administration of GK1.5 cDb suggest that CD4 may be dimerizing and internalizing as a result of GK1.5 cDb crosslinking. In addition to the challenge of drawing an ROI, multiple variables factor into how many CD4+ T cells can be detected with immunoPET, including antigen density, tissue volume, scanner resolution, and tissue accessibility. One consideration is whether quantification of uptake from the entire intestine is necessary and informative: in humans with IBD localized to the colon, such as ulcerative colitis, imaging may be sufficient to identify foci of inflammation in the colon alone, which could then be investigated further or quantified on a local basis.

ImmunoPET was unable to detect changes in colitic CD4+ T cells in the colons of mice treated with cyclosporin A (CsA). This may be due to evidence showing that CD4+ T cells infiltrate later in the DSS model (closer to d 12, per Hall et al., 2011), and CsA treatment during d 1-9 was too early to have a strong effect on CD4+ T cells. It is also possible that CsA treatment had a limited effect on the number of CD4+ T cells, and instead reduced inflammation by suppressing other immune cells such as neutrophils. Anti-CD4 IHC, although not performed here, could show whether the number of CD4+ T cells in the colon of CsA-treated colitic mice was changed compared to mice not treated with CsA. The inter-mouse variability in uptake along colons, as seen in the *ex vivo* scan, parallels the variability in disease severity observed between mice. Inter-mouse variability may have been due to changes in the amount of DSS water mice consumed (Sann et al., 2013); weighing the water bottles showed that four mice consistently drank ~10mL DSS water/day, but individual water consumption could not be determined.

Direct translational application of GK1.5 cDb to humans is limited, as GK1.5 cDb does not cross-react with human CD4. However, it has demonstrated proof-of-concept results for the use of antibody fragments in tracking CD4+ cells after stem cell transplant (Tavaré et al., 2015) and in IBD. Another consideration is the many differences between mouse and human immune systems. For example, mouse blood contains 75-90% lymphocytes, whereas human blood has just 30-50% lymphocytes (Mestas and Hughes, 2004). While the blood is of less concern due to the rapid clearance of the probe and the low proportion of the body's total lymphocytes present in the blood (Trepel, 1974), differences in the percent and/or number of lymphocytes in body tissues of humans could negate the results of the dose-escalation study performed here. With a new probe for

human CD4, however, the effects of protein dose would need to be explored anew, so this is not an insurmountable obstacle.

Interest and progress in antibody-targeted imaging is accelerating, supported by a push from the therapeutic antibody field (e.g. underlying work on target selection and validation, humanized and human antibodies, and production for clinical and commercial use) as well as a pull from medical fields, where there are still significant unmet needs in molecular imaging. In parallel, developments in imaging instrumentation and novel molecular probes are providing innovative new applications employing PET to provide highly specific information on biological processes *in vivo*, in both preclinical models and patients. With regard to clinical translation, radiolabeled antibody probes provide the most straightforward path, given the existing imaging infrastructure in nuclear medicine departments and established procedures for clinical production, radiolabeling, and regulatory review, as well as increased availability of long half-life PET radionuclides such as ^{89}Zr . Antibody-based biomarker imaging approaches are highly complementary to *in vitro* diagnostics, and should play an increasingly important role in providing essential information needed to effectively guide the development and implementation of molecularly targeted therapeutics as we move into the era of precision medicine.

In conclusion, anti-CD4 immunoPET is a promising tool for comprehensive investigation of CD4+ T cells. Preclinically, imaging may be used to add understanding about the localization and contribution of CD4+ T cells to various animal models. Clinically, anti-CD4 imaging could prove useful in detecting the immune response and imaging T cells in a variety of diseases.

References

- Aarntzen, E.H.J.G., Hermsen, R., Drenth, J.P.H., Boerman, O.C., Oyen, W.J.G., 2016. ^{99m}Tc-CXCL8 SPECT to monitor disease activity in inflammatory bowel disease. *J Nucl Med* 57, 398–403. doi:10.2967/jnumed.115.165795
- Agarwal, P., Bertozzi, C.R., 2015. Site-specific antibody–drug conjugates: the nexus of bioorthogonal chemistry, protein engineering, and drug development. *Bioconjug Chem* 26, 176–192. doi:10.1021/bc5004982
- Ahrens, E.T., Bulte, J.W.M., 2013. Tracking immune cells in vivo using magnetic resonance imaging. *Nat Rev Immunol* 13, 755–63. doi:10.1038/nri3531
- Atreya, R., Neumann, H., Neufert, C., Waldner, M.J., Billmeier, U., Zopf, Y., Willma, M., App, C., Münster, T., Kessler, H., Maas, S., Gebhardt, B., Heimke-Brinck, R., Reuter, E., Dörje, F., Rau, T.T., Uter, W., Wang, T.D., Kiesslich, R., Vieth, M., Hannappel, E., Neurath, M.F., 2014. In vivo imaging using fluorescent antibodies to tumor necrosis factor predicts therapeutic response in Crohn's disease. *Nat Med* 20, 313–8. doi:10.1038/nm.3462
- Axelsson, L.G., Landström, E., Goldschmidt, T.J., Grönberg, A., Bylund-Fellenius, A.C., 1996. Dextran sulfate sodium (DSS) induced experimental colitis in immunodeficient mice: effects in CD4+ -cell depleted, athymic and NK-cell depleted SCID mice. *Inflamm Res* 45, 181–91.
- Axup, J.Y., Bajjuri, K.M., Ritland, M., Hutchins, B.M., Kim, C.H., Kazane, S.A., Halder, R., Forsyth, J.S., Santidrian, A.F., Stafin, K., Lu, Y., Tran, H., Seller, A.J., Biroc, S.L., Szydlik, A., Pinkstaff, J.K., Tian, F., Sinha, S.C., Felding-Habermann, B., Smider, V. V, Schultz, P.G., 2012. Synthesis of site-specific antibody-drug conjugates using

- unnatural amino acids. *Proc Natl Acad Sci U S A* 109, 16101–6.
doi:10.1073/pnas.1211023109
- Bailey, S.R., Nelson, M.H., Himes, R. a, Li, Z., Mehrotra, S., Paulos, C.M., 2014. Th17 cells in cancer: the ultimate identity crisis. *Front Immunol* 5, 276.
doi:10.3389/fimmu.2014.00276
- Bamias, G., Pizarro, T.T., Cominelli, F., 2016. Pathway-based approaches to the treatment of inflammatory bowel disease. *Transl Res* 167, 104–115.
doi:10.1016/j.trsl.2015.09.002
- Bannas, P., Well, L., Lenz, A., Rissiek, B., Haag, F., Schmid, J., Hochgräfe, K., Trepel, M., Adam, G., Ittrich, H., Koch-Nolte, F., 2014. In vivo near-infrared fluorescence targeting of T cells: comparison of nanobodies and conventional monoclonal antibodies. *Contrast Media Mol Imaging* 9, 135–42. doi:10.1002/cmmi.1548
- Becker, W., Emmrich, F., Horneff, G., Burmester, G., Seller, F., Schwarz, A., Kalden, J., Wolf, F., 1990. Imaging rheumatoid arthritis specifically with technetium 99m CD4-specific (T-helper lymphocytes) antibodies. *Eur J Nucl Med* 17, 156–159.
- Ben-Horin, S., Kopylov, U., Chowers, Y., 2014. Optimizing anti-TNF treatments in inflammatory bowel disease. *Autoimmun Rev* 13, 24–30.
doi:10.1016/j.autrev.2013.06.002
- Benjamini, Y., Hochberg, Y., 1995. Controlling the false discovery rate: a practical and powerful approach to multiple testing. *J R Stat Soc B*. doi:10.2307/2346101
- Bennink, R.J., Peeters, M., Rutgeerts, P., Mortelmans, L., 2004. Evaluation of early treatment response and predicting the need for colectomy in active ulcerative colitis with ^{99m}Tc-HMPAO white blood cell scintigraphy. *J Nucl Med* 45, 1698–1704.

- Bettenworth, D., Reuter, S., Hermann, S., Weckesser, M., Kerstiens, L., Stratis, A., Nowacki, T.M., Ross, M., Lenze, F., Edemir, B., Maaser, C., Pap, T., Koschmieder, S., Heidemann, J., Schäfers, M., Lügering, A., 2013. Translational¹⁸F-FDG PET/CT imaging to monitor lesion activity in intestinal inflammation. *J Nucl Med* 54, 748–55. doi:10.2967/jnumed.112.112623
- Bhatti, M., Chapman, P., Peters, M., Haskard, D., Hodgson, H.J.F., 1998. Visualising E-selectin in the detection and evaluation of inflammatory bowel disease. *Gut* 43, 40–47. doi:10.1136/gut.43.1.40
- Bouchelouche, K., Choyke, P.L., Capala, J., 2010. Prostate specific membrane antigen—a target for imaging and therapy with radionuclides. *Discov Med* 9, 55–61.
- Brandtzaeg, P., Kiyono, H., Pabst, R., Russell, M.W., 2008. Terminology: nomenclature of mucosa-associated lymphoid tissue. *Mucosal Immunol* 1, 31–37. doi:10.1038/mi.2007.9
- Brewer, S., McPherson, M., Fujiwara, D., Turovskaya, O., Ziring, D., Chen, L., Takedatsu, H., Targan, S.R., Wei, B., Braun, J., 2008. Molecular imaging of murine intestinal inflammation with 2-deoxy-2-[¹⁸F]fluoro-D-glucose and positron emission tomography. *Gastroenterology* 135, 744–55. doi:10.1053/j.gastro.2008.06.040
- Broisat, A., Toczek, J., Dumas, L.S., Ahmadi, M., Bacot, S., Perret, P., Slimani, L., Barone-Rochette, G., Soubies, A., Devoogdt, N., Lahoutte, T., Fagret, D., Riou, L.M., Ghezzi, C., 2014. ^{99m}Tc-cAbVCAM1-5 imaging is a sensitive and reproducible tool for the detection of inflamed atherosclerotic lesions in mice. *J Nucl Med* 55, 1678–84. doi:10.2967/jnumed.114.143792
- Brown, R.K.J., Bohnen, N.I., Wong, K.K., Minoshima, S., Frey, K.A., 2014. Brain PET in

suspected dementia: patterns of altered FDG metabolism. *Radiographics* 34, 684–701. doi:10.1148/rg.343135065

Bruno, I., Martelossi, S., Geatti, O., Maggiore, G., Guastalla, P., Povolato, M., Ventura, A., 2002. Antigranulocyte monoclonal antibody immunoscintigraphy in inflammatory bowel disease in children and young adolescents. *Acta Paediatr* 91, 1050–1055.

Buck, D., Förschler, A., Lapa, C., Schuster, T., Vollmar, P., Korn, T., Nessler, S., Stadelmann, C., Drzezga, A., Buck, A.K., Wester, H.-J., Zimmer, C., Krause, B.-J., Hemmer, B., 2012. ¹⁸F-FDG PET detects inflammatory infiltrates in spinal cord experimental autoimmune encephalomyelitis lesions. *J Nucl Med* 53, 1269–76. doi:10.2967/jnumed.111.102608

Byrareddy, S.N., Arthos, J., Cicala, C., Villinger, F., Ortiz, K.T., Little, D., Sidell, N., Kane, M.A., Yu, J., Jones, J.W., Santangelo, P.J., Zurla, C., McKinnon, L.R., Arnold, K.B., Woody, C.E., Walter, L., Roos, C., Noll, A., Van Ryk, D., Jelcic, K., Cimbro, R., Gumber, S., Reid, M.D., Adsay, V., Amancha, P.K., Mayne, A.E., Parslow, T.G., Fauci, A.S., Ansari, A.A., 2016. Sustained virologic control in SIV+ macaques after antiretroviral and α 4 β 7 antibody therapy. *Science* 354, 197–202. doi:10.1126/science.aag1276

Cader, M.Z., Kaser, A., 2013. Recent advances in inflammatory bowel disease: mucosal immune cells in intestinal inflammation. *Gut* 62, 1653–64. doi:10.1136/gutjnl-2012-303955

Catafau, A.M., Bullich, S., 2015. Amyloid PET imaging: applications beyond Alzheimer's disease. *Clin Transl Imaging* 3, 39–55. doi:10.1007/s40336-014-0098-3

Chakravarty, R., Goel, S., Valdovinos, H.F., Hernandez, R., Hong, H., Nickles, R.J., Cai,

- W., 2014. Matching the decay half-life with the biological half-life: ImmunoPET imaging with ^{44}Sc -labeled Cetuximab Fab fragment. *Bioconjug Chem* 25, 2197–2204. doi:10.1021/bc500415x
- Chang, A.J., Sohn, R., Lu, Z.H., Arbeit, J.M., Lapi, S.E., 2013. Detection of rapalog-mediated therapeutic response in renal cancer xenografts using ^{64}Cu -bevacizumab immunoPET. *PLoS One* 8, e58949. doi:10.1371/journal.pone.0058949
- Chassaing, B., Aitken, J.D., Malleshappa, M., Vijay-Kumar, M., 2014. Dextran sulfate sodium (DSS)-induced colitis in mice. *Curr Protoc Immunol* 104, Unit 15.25. doi:10.1002/0471142735.im1525s104
- Cheng, D., Zou, W., Li, X., Xiu, Y., Tan, H., Shi, H., Yang, X., 2015. Preparation and evaluation of $^{99\text{m}}\text{Tc}$ -labeled anti-CD11b antibody targeting inflammatory microenvironment for colon cancer imaging. *Chem Biol Drug Des* 85, 696–701. doi:10.1111/cbdd.12459
- Csencsits, K., Burrell, B.E., Lu, G., Eichwald, E.J., Stahl, G.L., Bishop, D.K., 2008. The classical complement pathway in transplantation: Unanticipated protective effects of C1q and role in inductive antibody therapy. *Am J Transplant* 8, 1622–1630. doi:10.1111/j.1600-6143.2008.02295.x
- Danese, S., 2012. New therapies for inflammatory bowel disease: from the bench to the bedside. *Gut* 61, 918–32. doi:10.1136/gutjnl-2011-300904
- Dearling, J.L.J., Daka, A., Veiga, N., Peer, D., Packard, A.B., 2016. Colitis ImmunoPET: Defining Target Cell Populations and Optimizing Pharmacokinetics. *Inflamm Bowel Dis* 22, 529–538. doi:10.1097/MIB.0000000000000677
- Dearling, J.L.J., Park, E.J., Dunning, P., Baker, A., Fahey, F., Treves, S.T., Soriano, S.G.,

- Shimaoka, M., Packard, A.B., Peer, D., 2010. Detection of intestinal inflammation by MicroPET imaging using a ⁶⁴Cu-labeled anti-beta7 integrin antibody. *Inflamm Bowel Dis* 16, 1458–66. doi:10.1002/ibd.21231
- de Souza, H.S.P., Fiocchi, C., 2016. Immunopathogenesis of IBD: current state of the art. *Nat Rev Gastroenterol Hepatol* 13, 13–27. doi:10.1038/nrgastro.2015.186
- Deri, M.A.M., Ponnala, S., Zeglis, B.M.B., Pohl, G., Dannenberg, J.J., Lewis, J.S., Francesconi, L.C., 2014. Alternative chelator for ⁸⁹Zr radiopharmaceuticals: radiolabeling and evaluation of 3,4,3-(LI-1,2-HOPO). *J Med Chem* 57, 4849–4860. doi:dx.doi.org/10.1021/jm500389b
- Dewaraja, Y.K., Schipper, M.J., Shen, J., Smith, L.B., Murgic, J., Savas, H., Youssef, E., Regan, D., Wilderman, S.J., Roberson, P.L., Kaminski, M.S., Avram, A.M., 2014. Tumor-absorbed dose predicts progression-free survival following ¹³¹I-tositumomab radioimmunotherapy. *J Nucl Med* 55, 1047–1053. doi:10.2967/jnumed.113.136044
- Dialynas, D.P., Wilde, D.B., Marrack, P., Pierres, A., Wall, K.A., Havran, W., Otten, G., Loken, M.R., Pierres, M., Kappler, J., 1983. Characterization of the murine antigenic determinant, designated L3T4a, recognized by monoclonal antibody GK1.5: expression of L3T4a by functional T cell clones appears to correlate primarily with class II MHC antigen-reactivity. *Immunol Rev* 74, 29–56.
- Di Mascio, M., Paik, C.H., Carrasquillo, J.A., Maeng, J.-S., Jang, B.-S., Shin, I.S., Srinivasula, S., Byrum, R., Neria, A., Kopp, W., Catalfamo, M., Nishimura, Y., Reimann, K., Martin, M., Lane, H.C., 2009. Noninvasive in vivo imaging of CD4 cells in simian-human immunodeficiency virus (SHIV)-infected nonhuman primates. *Blood* 114, 328–37. doi:10.1182/blood-2008-12-192203

- Dianzani, U., Shaw, A., Al-Ramadi, B.K., Kubo, R.T., Janeway, C.A., 1992. Physical association of CD4 with the T cell receptor. *J Immunol* 148, 678–88.
- Dieleman, L.A., Palmen, M.J., Akol, H., Bloemena, E., Peña, A.S., Meuwissen, S.G., Van Rees, E.P., 1998. Chronic experimental colitis induced by dextran sulphate sodium (DSS) is characterized by Th1 and Th2 cytokines. *Clin Exp Immunol* 114, 385–91.
- Dieleman, L.A., Ridwan, B.U., Tennyson, G.S., Beagley, K.W., Bucy, R.P., Elson, C.O., 1994. Dextran sulfate sodium-induced colitis occurs in severe combined immunodeficient mice. *Gastroenterology* 107, 1643–1652.
- Dübel, S., Breitling, F., Fuchs, P., Zewe, M., Gotter, S., Welschhof, M., Moldenhauer, G., Little, M., 1994. Isolation of IgG antibody Fv-DNA from various mouse and rat hybridoma cell lines using the polymerase chain reaction with a simple set of primers. *J Immunol Methods* 175, 89–95. doi:10.1016/0022-1759(94)90334-4
- Evans, H., Nguyen, Q., Carroll, L.S., Kaliszczak, M., Twyman, F.J., Spivey, A.C., Aboagye, E.O., 2014. A bioorthogonal ⁶⁸Ga-labelling strategy for rapid in vivo imaging. *Chem Commun* 50, 9557–60. doi:10.1039/c4cc03903c
- Ewart, S.L., Gavett, S.H., Margolick, J., Wills-Karp, M., 1996. Cyclosporin A attenuates genetic airway hyperresponsiveness in mice but not through inhibition of CD4+ or CD8+ T Cells. *Am J Respir Cell Mol Biol* 14, 627–634.
- Feldkamp, L.A., Davis, L.C., Kress, J.W., 1984. Practical cone-beam algorithm. *J Opt Soc Am A* 1, 612. doi:10.1364/JOSAA.1.000612
- Fletcher, J.M., Lalor, S.J., Sweeney, C.M., Tubridy, N., Mills, K.H.G., 2010. T cells in multiple sclerosis and experimental autoimmune encephalomyelitis. *Clin Exp Immunol* 162, 1–11. doi:10.1111/j.1365-2249.2010.04143.x

- Fleuren, E.D.G., Versleijen-Jonkers, Y.M.H., Heskamp, S., van Herpen, C.M.L., Oyen, W.J.G., van der Graaf, W.T.A., Boerman, O.C., 2014. Theranostic applications of antibodies in oncology. *Mol Oncol* 8, 799–812. doi:10.1016/j.molonc.2014.03.010
- Freise, A.C., Wu, A.M., 2015. In vivo imaging with antibodies and engineered fragments. *Mol Immunol* 67, 142–52. doi:10.1016/j.molimm.2015.04.001
- Freise, A.C., Zettlitz, K.A., Salazar, F.B., Lu, X., Tavaré, R., Wu, A.M. In press. ImmunoPET imaging of murine CD4⁺ T cells using anti-CD4 cys-diabody: Effects of protein dose on T cell function and imaging. *Mol Imaging Biol*.
- Gálvez, J., 2014. Role of Th17 cells in the pathogenesis of human IBD. *ISRN Inflamm* 2014, 1–14. doi:10.1155/2014/928461
- Geremia, A., Biancheri, P., Allan, P., Corazza, G.R., Di Sabatino, A., 2014. Innate and adaptive immunity in inflammatory bowel disease. *Autoimmun Rev* 13, 3–10. doi:10.1016/j.autrev.2013.06.004
- Germain, R.N., Robey, E.A., Cahalan, M.D., 2012. A decade of imaging cellular motility and interaction dynamics in the immune system. *Science* 336, 1676–81. doi:10.1126/science.1221063
- Ghobrial, R.R.M., Boublik, M., Winn, H.J., Auchincloss Jr, H., 1989. In vivo use of monoclonal antibodies against murine T cell antigens 506, 486–506.
- Goverman, J., 2009. Autoimmune T cell responses in the central nervous system. *Nat Rev Immunol* 9, 393–407. doi:10.1038/nri2550
- Greve, D.N., Salat, D.H., Bowen, S.L., Izquierdo-Garcia, D., Schultz, A.P., Catana, C., Becker, J.A., Svarer, C., Knudsen, G.M., Sperling, R.A., Johnson, K.A., 2016. Different partial volume correction methods lead to different conclusions: An ¹⁸F-

FDG-PET study of aging. *Neuroimage* 132, 334–343.
doi:10.1016/j.neuroimage.2016.02.042

Gridley, D.S., Rizvi, A., Luo-Owen, X., Makinde, A.Y., Pecaut, M.J., 2009. Low Dose, Low Dose Rate Photon Radiation Modifies Leukocyte Distribution and Gene Expression in CD4+ T Cells. *J Radiat Res* 50, 139–150. doi:10.1269/jrr.08095

Griessinger, C.M., Kehlbach, R., Bukala, D., Wiehr, S., Bantleon, R., Cay, F., Schmid, A., Braumuller, H., Fehrenbacher, B., Schaller, M., Eichner, M., Sutcliffe, J.L., Ehrlichmann, W., Eibl, O., Reischl, G., Cherry, S.R., Rocken, M., Pichler, B.J., Kneilling, M., 2014. In vivo tracking of Th1 cells by PET reveals quantitative and temporal distribution and specific homing in lymphatic tissue. *J Nucl Med* 55, 301–307. doi:10.2967/jnumed.113.126318

Griessinger, C.M., Maurer, A., Kesenheimer, C., Kehlbach, R., Reischl, G., Ehrlichmann, W., Bukala, D., Harant, M., Cay, F., Brück, J., Nordin, R., Kohlhofer, U., Rammensee, H.-G., Quintanilla-Martinez, L., Schaller, M., Röcken, M., Pichler, B.J., Kneilling, M., 2015. ⁶⁴Cu antibody-targeting of the T-cell receptor and subsequent internalization enables in vivo tracking of lymphocytes by PET. *Proc Natl Acad Sci U S A* 112, 1161–1166. doi:10.1073/pnas.1418391112

Guérard, F., Lee, Y.-S., Brechbiel, M.W., 2014. Rational design, synthesis, and evaluation of tetrahydroxamic acid chelators for stable complexation of zirconium(IV). *Chem Eur J* 20, 5584–91. doi:10.1002/chem.201304115

Guérard, F., Lee, Y.-S., Tripier, R., Szajek, L.P., Deschamps, J.R., Brechbiel, M.W., 2013. Investigation of Zr(IV) and ⁸⁹Zr(IV) complexation with hydroxamates: progress towards designing a better chelator than desferrioxamine B for immuno-PET

- imaging. *Chem Commun* 49, 1002–1004. doi:10.1039/c2cc37549d
- Gutstein, N.L., Wofsy, D., 1986. Administration of F(ab')₂ fragments of monoclonal L3T4 inhibits humoral immunity in mice without depleting L3T4+ cells. *J Immunol* 137, 3414–3419.
- Hall, L.J., Faivre, E., Quinlan, A., Shanahan, F., Nally, K., Melgar, S., 2011. Induction and activation of adaptive immune populations during acute and chronic phases of a murine model of experimental colitis. *Dig Dis Sci* 56, 79–89. doi:10.1007/s10620-010-1240-3
- Haque, S., Saizawa, K., Rojo, J., Janeway, C.A., 1987. The influence of valence on the functional activities of monoclonal anti-L3T4 antibodies: discrimination of signaling from other effects. *J Immunol* 139, 3207–3212.
- Hendrickson, B.A., Gokhale, R., Cho, J.H., 2002. Clinical aspects and pathophysiology of inflammatory bowel disease. *Clin Microbiol Rev* 15, 79–94. doi:10.1128/CMR.15.1.79
- Higashikawa, K., Yagi, K., Watanabe, K., Kamino, S., Ueda, M., Hiromura, M., Enomoto, S., 2014. ⁶⁴Cu-DOTA-anti-CTLA-4 mAb enabled PET visualization of CTLA-4 on the T-cell infiltrating tumor tissues. *PLoS One* 9, e109866. doi:10.1371/journal.pone.0109866
- Hindryckx, P., Staelens, S., Devisscher, L., Deleye, S., De Vos, F., Delrue, L., Peeters, H., Laukens, D., De Vos, M., 2011. Longitudinal quantification of inflammation in the murine dextran sodium sulfate-induced colitis model using microPET/CT. *Inflamm Bowel Dis* 17, 2058–2064. doi:10.1002/ibd.21578
- Honarvar, H., Müller, C., Cohrs, S., Haller, S., Westerlund, K., Karlström, A.E., van der

- Meulen, N.P., Schibli, R., Tolmachev, V., 2017. Evaluation of the first ^{44}Sc -labeled Affibody molecule for imaging of HER2-expressing tumors. *Nucl Med Biol* 45, 15–21. doi:10.1016/j.nucmedbio.2016.10.004
- Honarvar, H., Strand, J., Perols, A., Orlova, A., Selvaraju, R.K., Karlström, A.E., Tolmachev, V., 2014. Position for site-specific attachment of a DOTA chelator to synthetic Affibody molecules has a different influence on the targeting properties of ^{68}Ga -compared to ^{111}In -labeled conjugates. *Mol Imaging* 13, 1–12. doi:10.2310/7290.2014.00034
- Houghton, J.L., Zeglis, B.M., Abdel-Atti, D., Sawada, R., Scholz, W.W., Lewis, J.S., 2016. Pretargeted Immuno-PET of pancreatic cancer: overcoming circulating antigen and internalized antibody to reduce radiation doses. *J Nucl Med* 57, 453–459. doi:10.2967/jnumed.115.163824
- James, M.L., Gambhir, S.S., 2012. A molecular imaging primer: modalities, imaging agents, and applications. *Physiol Rev* 92, 897–965. doi:10.1152/physrev.00049.2010
- Janeway Jr, C.A., Travers, P., Walport, M., Shlomchik, M.J., 2001. *Immunobiology: The Immune System in Health and Disease*, 5th ed. Garland Science, New York.
- Johnson, K.A., Fox, N.C., Sperling, R.A., Klunk, W.E., 2012. Brain imaging in Alzheimer disease. *Cold Spring Harb Perspect Med* 2, 1–23. doi:10.1101/cshperspect.a006213
- Johnson, L.L., Tekabe, Y., Kollaros, M., Eng, G., Bhatia, K., Li, C., Krueger, C.G., Shanmuganayagam, D., Schmidt, A.M., 2014. Imaging RAGE expression in atherosclerotic plaques in hyperlipidemic pigs. *EJNMMI Res* 4, 26. doi:10.1186/s13550-014-0026-6

- Kanwar, B., Gao, D.W., Hwang, A.B., Grenert, J.P., Williams, S.P., Franc, B., McCune, J.M., 2008. In vivo imaging of mucosal CD4+ T cells using single photon emission computed tomography in a murine model of colitis. *J Immunol Methods* 329, 21–30. doi:10.1016/j.jim.2007.09.008
- Kaser, A., Zeissig, S., Blumberg, R.S., 2010. Inflammatory bowel disease. *Annu Rev Immunol* 28, 573–621. doi:10.1146/annurev-immunol-030409-101225
- Keyaerts, M., Xavier, C., Heemskerk, J., Devoogdt, N., Everaert, H., Ackaert, C., Vanhoeij, M., Duhoux, F.P., Gevaert, T., Simon, P., Schallier, D., Fontaine, C., Vaneycken, I., Vanhove, C., De Greve, J., Lamote, J., Caveliers, V., Lahoutte, T., 2016. Phase I study of ⁶⁸Ga-HER2-Nanobody for PET/CT assessment of HER2 expression in breast carcinoma. *J Nucl Med* 57, 27–33. doi:10.2967/jnumed.115.162024
- Kim, C.H., Axup, J.Y., Dubrovskaya, A., Kazane, S.A., Hutchins, B.A., Wold, E.D., Smider, V. V, Schultz, P.G., 2012. Synthesis of bispecific antibodies using genetically encoded unnatural amino acids. *JACS* 134, 9918–21. doi:dx.doi.org/10.1021/ja303904e |
- Kim, C.H., Axup, J.Y., Schultz, P.G., 2013. Protein conjugation with genetically encoded unnatural amino acids. *Curr Opin Chem Biol* 17, 412–9. doi:10.1016/j.cbpa.2013.04.017
- Kim, J.M., Kang, H.W., Cha, M.Y., Yoo, D., Kim, N., Kim, I.-K., Ku, J., Kim, S., Ma, S.-H., Jung, H.C., Song, I.S., Kim, J.S., 2010. Novel guggulsterone derivative GG-52 inhibits NF-kappaB signaling in intestinal epithelial cells and attenuates acute murine colitis. *Lab Invest* 90, 1004–1015. doi:10.1038/labinvest.2010.54

- Kim, S.J., Kim, M.C., Um, J.Y., Hong, S.H., 2010. The beneficial effect of vanillic acid on ulcerative colitis. *Molecules* 15, 7208–7217. doi:10.3390/molecules15107208
- Kitajima, S., Takuma, S., Morimoto, M., 1999. Tissue distribution of dextran sulfate sodium (DSS) in the acute phase of murine DSS-induced colitis. *J Vet Med Sci* 61, 67–70.
- Knowles, S.M., Tavaré, R., Zettlitz, K.A., Rochefort, M.M., Salazar, F.B., Jiang, Z.K., Reiter, R.E., Wu, A.M., 2014. Applications of immunoPET: using ¹²⁴I-anti-PSCA A11 minibody for imaging disease progression and response to therapy in mouse xenograft models of prostate cancer. *Clin Cancer Res* 20, 6367–6378. doi:10.1158/1078-0432.CCR-14-1452
- Knowles, S.M., Wu, A.M., 2012. Advances in immuno-positron emission tomography: antibodies for molecular imaging in oncology. *J Clin Oncol* 30, 3884–92. doi:10.1200/JCO.2012.42.4887
- Kojouharoff, G., Hans, W., Obermeier, F., Männel, D.N., Andus, T., Schölmerich, J., Gross, V., Falk, W., 1997. Neutralization of tumour necrosis factor (TNF) but not of IL-1 reduces inflammation in chronic dextran sulphate sodium-induced colitis in mice. *Clin Exp Immunol* 107, 353–8. doi:10.1111/j.1365-2249.1997.291-ce1184.x
- Kolb, H.C., Finn, M.G., Sharpless, K.B., 2001. Click chemistry: diverse chemical function from a few good reactions. *Angew Chemie* 40, 2004–2021.
- Krüwel, T., Nevoltris, D., Bode, J., Dullin, C., Baty, D., Chames, P., Alves, F., 2016. In vivo detection of small tumour lesions by multi-pinhole SPECT applying a ^{99m}Tc-labelled nanobody targeting the Epidermal Growth Factor Receptor. *Sci Rep* 6, 21834. doi:10.1038/srep21834

- Li, K., Tavaré, R., Zettlitz, K.A., Mumenthaler, S.M., Mallick, P., Zhou, Y., Marks, J.D., Wu, A.M., 2014. Anti-MET ImmunoPET for non-small cell lung cancer using novel fully human antibody fragments. *Mol Cancer Ther* 13, 2607–17. doi:10.1158/1535-7163.MCT-14-0363
- Li, Y., Zhang, W., Wu, H., Liu, G., 2014. Advanced tracers in PET imaging of cardiovascular disease. *Biomed Res Int* 2014, 1–13. doi:10.1155/2014/504532
- Lim, Y.T., Cho, M.Y., Noh, Y.-W., Chung, J.W., Chung, B.H., 2009. Near-infrared emitting fluorescent nanocrystals-labeled natural killer cells as a platform technology for the optical imaging of immunotherapeutic cells-based cancer therapy. *Nanotechnology* 20, 475102. doi:10.1088/0957-4484/20/47/475102
- Liu, G., Hu, Y., Xiao, J., Li, X., Li, Y., Tan, H., Zhao, Y., Cheng, D., Shi, H., 2016. ^{99m}Tc-labelled anti-CD11b SPECT/CT imaging allows detection of plaque destabilization tightly linked to inflammation. *Sci Rep* 6, 1–12. doi:10.1038/srep20900
- Liu, S., Li, D., Guo, J., Canale, N., Li, X., Liu, R., Krasnoperov, V., Gill, P.S., Conti, P.S., Shan, H., Li, Z., 2014. Design, synthesis and validation of Axl-targeted monoclonal antibody probe for microPET imaging in human lung cancer xenograft. *Mol Pharm* 11, 3974–9. doi:10.1021/mp500307t
- Losa Garcia, L.E., Mateos Rodriguez, F., Jimenez Lopez, A., Garcia Salgado, M.J., Martin de Cabo, M., Perez Losada, J., Perez Arellano, J.L., 1998. Effect of cyclosporin A on inflammatory cytokine production by human alveolar macrophages. *Respir Med* 92, 722–728.
- Lütje, S., Franssen, G.M., Sharkey, R.M., Laverman, P., Rossi, E.A., Goldenberg, D.M., Oyen, W.J.G., Boerman, O.C., McBride, W.J., 2014a. Anti-CEA antibody fragments

- labeled with [^{18}F]AIF for PET imaging of CEA-expressing tumors. *Bioconjug Chem* 25, 335–41. doi:10.1021/bc4004926
- Lütje, S., van Rij, C.M., Franssen, G.M., Fracasso, G., Helfrich, W., Eek, A., Oyen, W.J., Colombatti, M., Boerman, O.C., 2014b. Targeting human prostate cancer with ^{111}In -labeled D2B IgG, $\text{F}(\text{ab}')^2$ and Fab fragments in nude mice with PSMA-expressing xenografts. *Contrast Media Mol Imaging* 10, 28–36. doi:10.1002/cmml.1596
- Ma, T., Sun, X., Cui, L., Gao, L., Wu, Y., Liu, H., Zhu, Z., Wang, F., Liu, Z., 2014. Molecular imaging reveals trastuzumab-induced epidermal growth factor receptor downregulation in vivo. *J Nucl Med* 55, 1002–1007. doi:10.2967/jnumed.114.137000
- Mandl, J.N., Liou, R., Klauschen, F., Vrisekoop, N., Monteiro, J.P., Yates, A.J., Huang, A.Y., Germain, R.N., 2012. Quantification of lymph node transit times reveals differences in antigen surveillance strategies of naïve CD4^+ and CD8^+ T cells. *Proc Natl Acad Sci U S A* 109, 1–7. doi:10.1073/pnas.1211717109
- Mansi, L., Kitson, S., Cuccurullo, V., Ciarmiello, A., 2014. Basic premises to molecular imaging and radionuclide therapy – part 1. *J Diagnostic Imaging Ther* 1, 137–156. doi:10.17229/jdit.2014-1125-010
- Markus, M.A., Dullin, C., Mitkovski, M., Prieschl-Grassauer, E., Epstein, M.M., Alves, F., 2014. Non-invasive optical imaging of eosinophilia during the course of an experimental allergic airways disease model and in response to therapy. *PLoS One* 9, 1–11. doi:10.1371/journal.pone.0090017
- Marquez, B. V., Lapi, S., 2016. Pretargeted immunoPET: Overcoming limitations of space and time. *J Nucl Med* 57, 332–334. doi:10.2967/jnumed.115.168096
- Massa, S., Xavier, C., De Vos, J., Caveliers, V., Lahoutte, T., Muyldermans, S., Devoogdt,

- N., 2014. Site-specific labeling of cysteine-tagged camelid single-domain antibody-fragments for use in molecular imaging. *Bioconjug Chem* 25, 979–88. doi:10.1021/bc500111t
- Matsuda, S., Koyasu, S., 2000. Mechanisms of action of cyclosporine. *Immunopharmacology* 47, 119–125. doi:10.1016/S0162-3109(00)00192-2
- Maynard, J., Georgiou, G., 2000. Antibody engineering. *Annu Rev Biomed Eng* 2, 339–76. doi:10.1146/annurev.bioeng.2.1.339
- McBride, H.J., 2010. Nuclear imaging of autoimmunity: focus on IBD and RA. *Autoimmunity* 43, 539–49. doi:10.3109/08916931003674766
- McBride, W.J., D'Souza, C.A., Sharkey, R.M., Goldenberg, D.M., 2012. The radiolabeling of proteins by the [¹⁸F]AIF method. *Appl Radiat Isot* 70, 200–4. doi:10.1016/j.apradiso.2011.08.013
- McCracken, M.N., Tavaré, R., Witte, O.N., Wu, A.M., 2016. Advances in PET detection of the antitumor T cell response, in: Alt, F.W. (Ed.), *Advances in Immunology*. Academic Press, Cambridge, MA, pp. 187–231. doi:10.1016/bs.ai.2016.02.004
- Melgar, S., Karlsson, A., Michaëlsson, E., 2005. Acute colitis induced by dextran sulfate sodium progresses to chronicity in C57BL/6 but not in BALB/c mice: correlation between symptoms and inflammation. *Am J Physiol Gastrointest Liver Physiol* 288, G1328–G1338. doi:10.1152/ajpgi.00467.2004
- Melgar, S., Karlsson, L., Rehnström, E., Karlsson, A., Utkovic, H., Jansson, L., Michaëlsson, E., 2008. Validation of murine dextran sulfate sodium-induced colitis using four therapeutic agents for human inflammatory bowel disease. *Int Immunopharmacol* 8, 836–44. doi:10.1016/j.intimp.2008.01.036

- Mestas, J., Hughes, C.C.W., 2004. Of mice and not men: differences between mouse and human immunology. *J Immunol* 172, 2731–8.
- Meyer, J.-P., Adumeau, P., Lewis, J.S., Zeglis, B.M., 2016. Click chemistry and radiochemistry: the first 10 years. *Bioconjug Chem* acs.bioconjchem.6b00561. doi:10.1021/acs.bioconjchem.6b00561
- Moolenbeek, C., Ruitenber, E.J., 1981. The “Swiss roll”: a simple technique for histological studies of the rodent intestine. *Lab Anim* 15, 57–9.
- Morgan, M.E., Zheng, B., Koelink, P.J., van de Kant, H.J.G., Haazen, L.C.J.M., van Roest, M., Garssen, J., Folkerts, G., Kraneveld, A.D., 2013. New perspective on dextran sodium sulfate colitis: antigen-specific T cell development during intestinal inflammation. *PLoS One* 8, 1–12. doi:10.1371/journal.pone.0069936
- Murthy, S.N.S., Cooper, H.S., Shim, H., Shah, R.S., Ibrahim, S.A., Sedergran, D.J., 1993. Treatment of dextran sulfate sodium-induced murine colitis by intracolonic cyclosporin. *Dig Dis Sci* 38, 1722–1734. doi:10.1007/BF01303184
- Nair-Gill, E.D., Shu, C.J., Radu, C.G., Witte, O.N., 2008. Non-invasive imaging of adaptive immunity using positron emission tomography. *Immunol Rev* 221, 214–28. doi:10.1111/j.1600-065X.2008.00585.x
- Natarajan, A., Gowrishankar, G., Nielsen, C.H., Wang, S., Iagaru, A., Goris, M.L., Gambhir, S.S., 2012. Positron emission tomography of ⁶⁴Cu-DOTA-rituximab in a transgenic mouse model expressing human CD20 for clinical translation to image NHL. *Mol Imaging Biol* 14, 608–16. doi:10.1007/s11307-011-0537-8
- Nimmagadda, S., Pullambhatla, M., Lisok, A., Hu, C., Maitra, A., Pomper, M.G., 2014. Imaging Axl expression in pancreatic and prostate cancer xenografts. *Biochem*

- Biophys Res Commun 443, 635–40. doi:10.1016/j.bbrc.2013.12.014
- Nishiyama, Y., Kataoka, T., Yamato, K., Taguchi, T., Yamaoka, K., 2012. Suppression of dextran sulfate sodium-induced colitis in mice by radon inhalation. *Mediators Inflamm* 2012, 1–11. doi:10.1155/2012/239617
- Norii, M., Yamamura, M., Iwahashi, M., Ueno, A., Yamana, J., Makino, H., 2006. Selective recruitment of CXCR3+ and CCR5+ CD4+ T cells into synovial tissue in patients with rheumatoid arthritis. *Acta Med Okayama* 60, 149–157.
- Ogasawara, A., Tinianow, J.N., Vanderbilt, A.N., Gill, H.S., Yee, S., Flores, J.E., Williams, S.P., Ashkenazi, A., Marik, J., 2013. ImmunoPET imaging of phosphatidylserine in pro-apoptotic therapy treated tumor models. *Nucl Med Biol* 40, 15–22. doi:10.1016/j.nucmedbio.2012.09.001
- Okoye, A.A., Picker, L.J., 2013. CD4+ T-cell depletion in HIV infection: mechanisms of immunological failure. *Immunol Rev* 254, 54–64. doi:10.1111/imr.12066
- Olafsen, T., Cheung, C.W., Yazaki, P.J., Li, L., Sundaresan, G., Gambhir, S.S., Sherman, M.A., Williams, L.E., Shively, J.E., Raubitschek, A.A., Wula, A.M., 2004. Covalent disulfide-linked anti-CEA diabody allows site-specific conjugation and radiolabeling for tumor targeting applications. *Protein Eng Des Sel* 17, 21–27. doi:10.1093/protein/gzh009
- Olafsen, T., Wu, A.M., 2010. Antibody vectors for imaging. *Semin Nucl Med* 40, 167–81. doi:10.1053/j.semnuclmed.2009.12.005
- Palmer, M.T., Weaver, C.T., 2010. Autoimmunity: increasing suspects in the CD4+ T cell lineup. *Nat Immunol* 11, 36–40. doi:10.1038/ni.1802
- Pandit-Taskar, N., O'Donoghue, J.A., Ruan, S., Lyashchenko, S., Carrasquillo, J.A.,

- Heller, G., Martinez, D.F., Cheal, S.M., Lewis, J.S., Fleisher, M., Keppler, J.S., Reiter, R.E., Wu, A.M., Weber, W.A., Scher, H.I., Larson, S.M., Morris, M.J., 2016. First-in-human imaging with ^{89}Zr -Df-IAB2M anti-PSMA minibody in patients with metastatic prostate cancer: pharmacokinetics, biodistribution, dosimetry, and lesion uptake. *J Nucl Med*. doi:10.2967/jnumed.116.176206
- Pandit-Taskar, N., Veach, D.R., Fox, J.J., Scher, H.I., Morris, M.J., Larson, S.M., 2016. Evaluation of castration-resistant prostate cancer with androgen receptor-axis imaging. *J Nucl Med* 57, 73S–78S. doi:10.2967/jnumed.115.170134
- Patra, M., Zarschler, K., Pietzsch, H.-J., Stephan, H., Gasser, G., 2016. New insights into the pretargeting approach to image and treat tumours. *Chem Soc Rev* 45, 6415–6431. doi:10.1039/C5CS00784D
- Phelps, M.E., 2000. Positron emission tomography provides molecular imaging of biological processes. *Proc Natl Acad Sci U S A* 97, 9226–9233. doi:10.1073/pnas.97.16.9226
- Poli, G.L., Bianchi, C., Virota, G., Bettini, A., Moretti, R., Trachsel, E., Elia, G., Giovannoni, L., Neri, D., Bruno, A., 2013. Radretumab radioimmunotherapy in patients with brain metastasis: a ^{124}I -L19SIP dosimetric PET study. *Cancer Immunol Res* 1, 134–43. doi:10.1158/2326-6066.CIR-13-0007
- Price, E.W., Zeglis, B.M., Lewis, J.S., Adam, M.J., Orvig, C., 2014. H6phospa-trastuzumab: bifunctional methylenephosphonate-based chelator with ^{89}Zr , ^{111}In and ^{177}Lu . *Dalt Trans* 43, 119–31. doi:10.1039/c3dt51940f
- Quah, B.J.C., Warren, H.S., Parish, C.R., 2007. Monitoring lymphocyte proliferation in vitro and in vivo with the intracellular fluorescent dye carboxyfluorescein diacetate

- succinimidyl ester. *Nat Protoc* 2, 2049–56. doi:10.1038/nprot.2007.296
- Rashidian, M., Keliher, E.J., Dougan, M., Juras, P.K., Cavallari, M., Wojtkiewicz, G.R., Jacobsen, J.T., Edens, J.G., Tas, J.M.J., Victora, G., Weissleder, R., Ploegh, H., 2015. Use of ¹⁸F-2-fluorodeoxyglucose to label antibody fragments for immunopositron emission tomography of pancreatic cancer. *ACS Cent Sci* 1, 142–47. doi:10.1021/acscentsci.5b00121
- Redman, J.M., Hill, E.M., AlDeghaither, D., Weiner, L.M., 2015. Mechanisms of action of therapeutic antibodies for cancer. *Mol Immunol* 67, 28–45. doi:10.1016/j.molimm.2015.04.002
- Rocheftort, M.M., Girgis, M.D., Ankeny, J.S., Tomlinson, J.S., 2014. Metabolic exploitation of the sialic acid biosynthetic pathway to generate site-specifically labeled antibodies. *Glycobiology* 24, 62–9. doi:10.1093/glycob/cwt090
- Rödel, F., Frey, B., Gaipf, U., Keilholz, L., Fournier, C., Manda, K., Schöllnberger, H., Hildebrandt, G., Rödel, C., 2012. Modulation of inflammatory immune reactions by low-dose ionizing radiation: molecular mechanisms and clinical application. *Curr Med Chem* 19, 1741–50. doi:CMC-EPUB-20120312-005 [pii]
- Rossin, R., Robillard, M.S., 2014. Pretargeted imaging using bioorthogonal chemistry in mice. *Curr Opin Chem Biol* 21, 161–9. doi:10.1016/j.cbpa.2014.07.023
- Rubin, R.H., Baltimore, D., Chen, B.K., Wilkinson, R.A., Fischman, A.J., 1996. In vivo tissue distribution of CD4 lymphocytes in mice determined by radioimmunosciintigraphy with an ¹¹¹In-labeled anti-CD4 monoclonal antibody. *Proc Natl Acad Sci U S A* 93, 7460–3.
- Ruigrok, V.J.B., Levisson, M., Eppink, M.H.M., Smidt, H., van der Oost, J., 2011.

- Alternative affinity tools: more attractive than antibodies? *Biochem J* 436, 1–13.
doi:10.1042/BJ20101860
- Sann, H., Erichsen, J. Von, Hessmann, M., Pahl, A., Hoffmeyer, A., 2013. Efficacy of drugs used in the treatment of IBD and combinations thereof in acute DSS-induced colitis in mice. *Life Sci* 92, 708–718. doi:10.1016/j.lfs.2013.01.028
- Sato, N., Wu, H., Asiedu, K.O., Szajek, L.P., Griffiths, G.L., Choyke, P.L., 2015. 89Zr-oxine complex PET cell imaging in monitoring cell-based therapies. *Radiology* 275, 490–500. doi:10.1148/radiol.15142849
- Schöll, M., Lockhart, S.N., Schonhaut, D.R., O’Neil, J.P., Janabi, M., Ossenkoppele, R., Baker, S.L., Vogel, J.W., Faria, J., Schwimmer, H.D., Rabinovici, G.D., Jagust, W.J., 2016. PET imaging of tau deposition in the aging human brain. *Neuron* 89, 971–982. doi:10.1016/j.neuron.2016.01.028
- Schoonooghe, S., Laoui, D., Van Ginderachter, J.A., Devoogdt, N., Lahoutte, T., De Baetselier, P., Raes, G., 2012. Novel applications of nanobodies for in vivo bio-imaging of inflamed tissues in inflammatory diseases and cancer. *Immunobiology* 217, 1266–72. doi:10.1016/j.imbio.2012.07.009
- Schuster, D.M., Nanni, C., Fanti, S., 2016. Evaluation of prostate cancer with radiolabeled amino acid analogs. *J Nucl Med* 57, 61S–66S. doi:10.2967/jnumed.115.170209
- Scott, A.M., Wolchok, J.D., Old, L.J., 2012. Antibody therapy of cancer. *Nat Rev Cancer* 12, 278–87. doi:10.1038/nrc3236
- Sha, T., Igaki, K., Yamasaki, M., Watanabe, T., Tsuchimori, N., 2013. Establishment and validation of a new semi-chronic dextran sulfate sodium-induced model of colitis in mice. *Int Immunopharmacol* 15, 23–29. doi:10.1016/j.intimp.2012.10.022

- Shankar, B., Premachandran, S., Bharambe, S.D., Sundaresan, P., Sainis, K.B., 1999. Modification of immune response by low dose ionizing radiation: role of apoptosis. *Immunol Lett* 68, 237–45.
- Shintani, N., Nakajima, T., Okamoto, T., Kondo, T., Nakamura, N., Mayumi, T., 1998. Involvement of CD4+ T cells in the development of dextran sulfate sodium-induced experimental colitis and suppressive effect of IgG on their action. *Gen Pharmacol* 31, 477–81.
- Silverman, D.H.S., 2004. Brain ¹⁸F-FDG PET in the diagnosis of neurodegenerative dementias: comparison with perfusion SPECT and with clinical evaluations lacking nuclear imaging. *J Nucl Med* 45, 594–607.
- Smaglo, B.G., Aldeghaither, D., Weiner, L.M., 2014. The development of immunoconjugates for targeted cancer therapy. *Nat Rev Clin Oncol* 11, 637–648. doi:10.1038/nrclinonc.2014.159
- Sörensen, J., Velikyan, I., Sandberg, D., Wennborg, A., Feldwisch, J., Tolmachev, V., Orlova, A., Sandström, M., Lubberink, M., Olofsson, H., Carlsson, J., Lindman, H., 2016. Measuring HER2-receptor expression in metastatic breast cancer using [⁶⁸Ga]ABY-025 Affibody PET/CT. *Theranostics* 6, 262–271. doi:10.7150/thno.13502
- Spisani, S., Fabbri, E., Muccinelli, M., Cariani, A., Barbin, L., Trotta, F., Dovigo, L., 2001. Inhibition of neutrophil responses by cyclosporin A. An insight into molecular mechanisms. *Rheumatology* 40, 794–800.
- Steinhoff, K., Pierer, M., Siegert, J., Pigla, U., Laub, R., Hesse, S., Seidel, W., Sorger, D., Seese, A., Kuenstler, J.U., Pietzsch, H.J., Lincke, T., Rullmann, M., Emmrich, F., Sabri, O., 2014. Visualizing inflammation activity in rheumatoid arthritis with Tc-99 m

anti-CD4-mAb fragment scintigraphy. *Nucl Med Biol* 41, 350–4.
doi:10.1016/j.nucmedbio.2013.12.018

Strand, J., Varasteh, Z., Eriksson, O., Abrahmsen, L., Orlova, A., Tolmachev, V., 2014. Gallium-68-labeled affibody molecule for PET imaging of PDGFR β expression in vivo. *Mol Pharm* 11, 3957–64. doi:10.1021/mp500284t

Suzuki, S., Toyabe, S., Moroda, T., Tada, T., Tsukahara, a, Iiai, T., Minagawa, M., Maruyama, S., Hatakeyama, K., Endoh, K., Abo, T., 1997. Circadian rhythm of leucocytes and lymphocytes subsets and its possible correlation with the function of the autonomic nervous system. *Clin Exp Immunol* 110, 500–508. doi:10.1046/j.1365-2249.1997.4411460.x

Swiercz, R., Chiguru, S., Tahmasbi, A., Ramezani, S.M., Hao, G., Challa, D.K., Lewis, M.A., Kulkarni, P. V, Sun, X., Ober, R.J., Mason, R.P., Ward, E.S., 2014. Use of Fc-engineered antibodies as clearing agents to increase contrast during PET. *J Nucl Med* 55, 1204–1207. doi:10.2967/jnumed.113.136481

Taschereau, R., Vu, N.T., Chatziioannou, A.F., 2014. Calibration and data standardization of a prototype bench-top preclinical CT, in: 2014 IEEE Nuclear Science Symposium and Medical Imaging Conference (NSS/MIC). IEEE, pp. 1–2. doi:10.1109/NSSMIC.2014.7430845

Tavaré, R., Escuin-Ordinas, H., Mok, S., McCracken, M.N., Zettlitz, K.A., Salazar, F.B., Witte, O.N., Ribas, A., Wu, A.M., 2016. An effective immuno-PET imaging method to monitor CD8-dependent responses to immunotherapy. *Cancer Res* 76, 73–82. doi:10.1158/0008-5472.CAN-15-1707

Tavaré, R., McCracken, M.N., Zettlitz, K.A., Knowles, S.M., Salazar, F.B., Olafsen, T.,

- Witte, O.N., Wu, A.M., 2014a. Engineered antibody fragments for immuno-PET imaging of endogenous CD8+ T cells in vivo. *Proc Natl Acad Sci U S A* 111, 1108–13. doi:10.1073/pnas.1316922111
- Tavaré, R., McCracken, M.N., Zettlitz, K.A., Salazar, F.B., Witte, O.N., Wu, A.M., 2015. ImmunoPET of murine T cell reconstitution post-adoptive stem cell transplant using anti-CD4 and anti-CD8 cys-diabodies. *J Nucl Med* 56, 1258–1264. doi:10.2967/jnumed.114.153338
- Tavaré, R., Wu, W.H., Zettlitz, K.A., Salazar, F.B., McCabe, K.E., Marks, J.D., Wu, A.M., 2014b. Enhanced immunoPET of ALCAM-positive colorectal carcinoma using site-specific ⁶⁴Cu-DOTA conjugation. *Protein Eng Des Sel* 27, 317–24. doi:10.1093/protein/gzu030
- Tillmanns, J., Schneider, M., Fraccarollo, D., Schmitto, J.-D., Länger, F., Richter, D., Bauersachs, J., Samnick, S., 2015. PET imaging of cardiac wound healing using a novel [⁶⁸Ga]-labeled NGR probe in rat myocardial infarction. *Mol Imaging Biol* 17, 76–86. doi:10.1007/s11307-014-0751-2
- Treglia, G., Quartuccio, N., Sadeghi, R., Farchione, A., Caldarella, C., Bertagna, F., Fania, P., Cistaro, A., 2013. Diagnostic performance of fluorine-18-fluorodeoxyglucose positron emission tomography in patients with chronic inflammatory bowel disease: A systematic review and a meta-analysis. *J Crohn's Colitis* 7, 345–354. doi:10.1016/j.crohns.2012.08.005
- Trepel, F., 1974. Number and distribution of lymphocytes in man. A critical analysis. *Klin Wochenschr* 52, 511–515. doi:10.1007/BF01468720
- Ulaner, G.A., Hyman, D., Ross, D., Corben, A., Chandarlapaty, S., Goldfarb, S.,

- McArthur, H., Erinjeri, J., Solomon, S., Kolb, H., Lyashchenko, S., Lewis, J., Carrasquillo, J., 2016. Detection of HER2-positive metastases in patients with HER2-negative primary breast cancer using the ^{89}Zr -DFO-trastuzumab PET/CT. *J Nucl Med* 132676, 1–25. doi:10.2967/jnumed.115.172031
- van de Watering, F.C.J., Rijpkema, M., Perk, L., Brinkmann, U., Oyen, W.J.G., Boerman, O.C., 2014. Zirconium-89 labeled antibodies: a new tool for molecular imaging in cancer patients. *Biomed Res Int* 2014, 1–13. doi:10.1155/2014/203601
- van Rij, C.M., Lütje, S., Frielink, C., Sharkey, R.M., Goldenberg, D.M., Franssen, G.M., McBride, W.J., Rossi, E.A., Oyen, W.J.G., Boerman, O.C., 2013. Pretargeted immuno-PET and radioimmunotherapy of prostate cancer with an anti-TROP-2 x anti-HSG bispecific antibody. *Eur J Nucl Med Mol Imaging* 40, 1377–83. doi:10.1007/s00259-013-2434-7
- Verhelle, A., Van Overbeke, W., Peleman, C., De Smet, R., Zwaenepoel, O., Lahoutte, T., Van Dorpe, J., Devoogdt, N., Gettemans, J., 2016. Non-invasive imaging of amyloid deposits in a mouse model of AGel using $^{99\text{m}}\text{Tc}$ -modified nanobodies and SPECT/CT. *Mol Imaging Biol* 18, 887–897. doi:10.1007/s11307-016-0960-y
- Vignali, D.A., Vignali, K.M., 1999. Profound enhancement of T cell activation mediated by the interaction between the TCR and the D3 domain of CD4. *J Immunol* 162, 1431–1439.
- Viola-Villegas, N.T., Sevak, K.K., Carlin, S.D., Doran, M.G., Evans, H.W., Bartlett, D.W., Wu, A.M., Lewis, J.S., 2014. Noninvasive imaging of PSMA in prostate tumors with ^{89}Zr -Labeled huJ591 engineered antibody fragments: the faster alternatives. *Mol Pharm* 11, 3965–73. doi:10.1021/mp500164r

- Wahl, R.L., 2005. Tositumomab and ¹³¹I therapy in non-Hodgkin's lymphoma. *J Nucl Med* 46, 128–140.
- Waldron, A.-M., Fissers, J., Van Eetveldt, A., Van Broeck, B., Mercken, M., Pemberton, D.J., Van Der Veken, P., Augustyns, K., Joossens, J., Stroobants, S., Dedeurwaerdere, S., Wyffels, L., Staelens, S., 2016. In vivo amyloid-β imaging in the APPPS1–21 transgenic mouse model with a ⁸⁹Zr-labeled monoclonal antibody. *Front Aging Neurosci* 8, 1–12. doi:10.3389/fnagi.2016.00067
- Wang, J.H., Meijers, R., Xiong, Y., Liu, J.H., Sakihama, T., Zhang, R., Joachimiak, A., Reinherz, E.L., 2001. Crystal structure of the human CD4 N-terminal two-domain fragment complexed to a class II MHC molecule. *Proc Natl Acad Sci U S A* 98, 10799–804. doi:10.1073/pnas.191124098
- Ward, E.S., Devanaboyina, S.C., Ober, R.J., 2015. Targeting FcRn for the modulation of antibody dynamics. *Mol Immunol* 67, 131–141. doi:10.1016/j.molimm.2015.02.007
- Weissleder, R., Nahrendorf, M., Pittet, M.J., 2014. Imaging macrophages with nanoparticles. *Nat Mater* 13, 125–38. doi:10.1038/nmat3780
- Westermann, J., Pabst, R., 1992. Distribution of lymphocyte subsets and natural killer cells in the human body. *Clin Investig* 70, 539–544. doi:10.1007/BF00184787
- Wilde, D.B., Marrack, P., Kappler, J., Dialynas, D.P., Fitch, F.W., 1983. Evidence implicating L3T4 in class II antigen reactivity; monoclonal antibody GK1.5 (anti-L3T4a) blocks class II MHC antigen-specific proliferation, release of lymphokines, and binding by cloned murine helper T lymphocyte lines. *J Immunol* 131, 78–83.
- Wirtz, S., Neurath, M.F., 2007. Mouse models of inflammatory bowel disease. *Adv Drug Deliv Rev* 59, 1073–1083. doi:10.1016/j.addr.2007.07.003

- Wu, A.M., 2014. Engineered antibodies for molecular imaging of cancer. *Methods* 65, 139–47. doi:10.1016/j.ymeth.2013.09.015
- Wu, Y., Zhu, H., Zhang, B., Liu, F., Chen, J., Wang, Y., Wang, Y., Zhang, Z., Wu, L., Si, L., Xu, H., Yao, T., Xiao, S., Xia, Q., Zhang, L., Yang, Z., Zhou, D., 2016. Synthesis of site-specific radiolabeled antibodies for radioimmunotherapy via genetic code expansion. *Bioconjug Chem* 27, 2460–2468. doi:10.1021/acs.bioconjchem.6b00412
- Wu, Z., Li, L., Liu, S., Yakushijin, F., Yakushijin, K., Horne, D., Conti, P.S., Li, Z., Kandeel, F., Shively, J.E., 2014. Facile preparation of a thiol-reactive ^{18}F -labeling agent and synthesis of ^{18}F -DEG-VS-NT for PET imaging of a neurotensin receptor-positive tumor. *J Nucl Med* 55, 1178–1184. doi:10.2967/jnumed.114.137489
- Xavier, C., Vaneycken, I., D’huyvetter, M., Heemskerk, J., Keyaerts, M., Vincke, C., Devoogdt, N., Muyltermans, S., Lahoutte, T., Caveliers, V., 2013. Synthesis, preclinical validation, dosimetry, and toxicity of ^{68}Ga -NOTA-anti-HER2 Nanobodies for iPET imaging of HER2 receptor expression in cancer. *J Nucl Med* 54, 776–84. doi:10.2967/jnumed.112.111021
- Yamamoto, A., Itoh, T., Nasu, R., Nishida, R., 2013. Effect of sodium alginate on dextran sulfate sodium- and 2,4,6-trinitrobenzene sulfonic acid-induced experimental colitis in mice. *Pharmacology* 92, 108–116. doi:10.1159/000353192
- Yao, Y., Han, W., Liang, J., Ji, J., Wang, J., Cantor, H., Lu, L., 2013. Glatiramer acetate ameliorates inflammatory bowel disease in mice through the induction of Qa-1-restricted CD8⁺ regulatory cells. *Eur J Immunol* 43, 125–136. doi:10.1002/eji.201242758
- Zanetti, M., 2015. Tapping CD4 T cells for cancer immunotherapy: the choice of

- personalized genomics. *J Immunol* 194, 2049–2056. doi:10.4049/jimmunol.1402669
- Zeglis, B.M., Sevak, K.K., Reiner, T., Mohindra, P., Carlin, S.D., Zanzonico, P., Weissleder, R., Lewis, J.S., 2013. A pretargeted PET imaging strategy based on bioorthogonal Diels-Alder click chemistry. *J Nucl Med* 54, 1389–96. doi:10.2967/jnumed.112.115840
- Zhu, A., Lee, D., Shim, H., 2011. Metabolic positron emission tomography imaging in cancer detection and therapy response. *Semin Oncol* 38, 55–69. doi:10.1053/j.seminoncol.2010.11.012
- Zhu, J., Paul, W.E., 2008. CD4 T cells: fates, functions, and faults. *Blood* 112, 1557–69. doi:10.1182/blood-2008-05-078154
- Zielinski, R., Hassan, M., Lyakhov, I., Needle, D., Chernomordik, V., Garcia-Glaessner, A., Ardeshirpour, Y., Capala, J., Gandjbakhche, A., 2012. Affibody-DyLight conjugates for in vivo assessment of HER2 expression by near-infrared optical imaging. *PLoS One* 7, e41016. doi:10.1371/journal.pone.0041016
- Zola, H., Stuart, B., Nicholson, I., Voss, E., 2007. *Leukocyte and stromal cell molecules: the CD markers*. John Wiley & Sons, Hoboken.